UNIVERSITY OF CALIFORNIA SAN DIEGO

Measuring Seafloor Displacement using Repeated Sidescan Sonar Surveys

A dissertation submitted in partial satisfaction of the
requirements for the degree
Doctor of Philosophy

in

Earth Sciences

by

John B. DeSanto

Committee in charge:

David T. Sandwell, Chair
Duncan C. Agnew
Donna Blackman
C. David Chadwell
Jeff Gee
Pui-Shum Shing

2018

The dissertation of John B. DeSanto is approved, and it is acceptable in quality and form for publication on microfilm and electronically:

_____

_____

_____

_____

_____

_____

Chair

University of California San Diego

2018

DEDICATION

To the IGPP tea masters, and the wonderful office culture that allowed them to rise to prominence.

EPIGRAPH

"...in L.A. as the forecast heats up. More hot and sunny weather on the way!"

"That was good weather, Suzie. Officials say they're not concerned about a series of small tremors along a length of 101. Cleanup crews are on the scene and traffic should be back to normal within the hour."

"...Breaking news, huh, Tom?"

"Well, it's not my... fault, Suzie. Uh oh."

—"L.A. Falls", from the album *Arizona Bay*, by Bill Hicks

TABLE OF CONTENTS

LIST OF FIGURES

LIST OF TABLES

ACKNOWLEDGEMENTS

As much as I would like to claim to have accomplished all of the work presented in this thesis solely on my own, the simple truth of the matter is that I have been aided by many people during my time as a graduate student.

The first person I would like to thank is my advisor David Sandwell. Dave has always had his office open for me and has actively supported my research endeavors at every stage of my graduate career. In addition, I am convinced he has supported me from behind the scenes in various ways as well, although I probably cannot know the full extent of his influence on the environment I have thrived in. As someone who is easily approachable, brilliant yet humble, and remarkably clever, Dave is a man whom I view as being the model scientist.

This is to say nothing of the rest of my thesis committee. David Chadwell has actively collaborated in my work at many steps, and has been an invaluable resource. Donna Blackman, Duncan Agnew, Jeff Gee, and Pui-Shum Shing have also been helpful in offering valuable feedback integral to the quality of this thesis.

Organizing and conducting offshore research is an intensely collaborative affair, and I have interacted with many people associated with my limited time at sea that have made the work presented here possible or otherwise broadened my horizons as a marine geophysicist. These people include the folks at the Ship Scheduling Office and Shipboard Technical Services, without whom no seagoing research would occur, as well as the crews of the R/V Roger Revelle and R/V Sally Ride. More specifically, I would like to thank James Holmes for volunteering his time during the RR1605 cruise, Matt Cook for organizing the SR1704 cruise as chief scientist, Kerry Key and Rob Evans for allowing me to join their CSEM experiment offshore New Jersey, Masako Tominaga and Anne Trehu for organizing the 2017 Early Career Chief Scientist training cruise, Valeria Reyes-Ortega and Steve Constable and David Sandwell for organizing the fall

2017 CSEM deployment across the Mendocino Fracture Zone, and David Chadwell and David Schmidt for organizing the summer 2018 GPS-Acoustic recovery and deployment offshore Cascadia.

Aside from the above, I have benefitted immensely simply by being a part of IGPP. Emmanuel "Soli" Garcia and Eric Lindsey were important mentor figures among the older students, and I certainly would like to be more like them. Various other students were also often available to discuss ideas with or answer inquiries that would otherwise have led to major headaches, in particular other members and close associates of the Sandwell lab including but not limited to Xiaohua "Eric" Xu, Ekaterina Tymofyeyeva, and Dan Bassett, and members of my IGPP cohort, including Matt Cook, Jessie Saunders, Dara Goldberg, and Adrian Doran. I hope I have been able to contribute to making the environment of IGPP as welcoming and beneficial for other students as it has been for myself, but it is not my place to judge whether or not I have been successful.

The final person whom I feel compelled to acknowledge is my father, Samuel DeSanto, who taught me how to read, English grammar, and basic arithmetic when I was still in elementary school. Although it is safe to say that arguably little of this remains incredibly relevant to my current studies, his early tutoring was undoubtedly critical in setting me on the path to becoming the intellectual I currently am. I have been privileged to have met and been taught by many brilliant and preeminent scientists during my short career, but one of the people whom has had the greatest impact on me is a humble elementary school teacher, a proverbial dwarf among giants. I can't help but feel there is some beautiful irony there.

Chapter 2, in full, is an unpublished compilation of notes on multibeam theory compiled by John B. DeSanto and David T. Sandwell. The dissertation author is the primary investigator and author of this paper.

Chapter 3, in full, is a reprint of the material as it appears in the Journal of Geophysical Research Solid Earth: DeSanto, J. B., D. T. Sandwell, C. D. Chadwell, "Seafloor Geodesy from Repeated Sidescan Sonar Surveys", *J. Geophys. Res. Solid Earth*, 121, pp.4800-4813, 2016. The dissertation author is the primary investigator and author of this paper.

Chapter 4, in full, is currently being prepared for publication as DeSanto, J. B., Sandwell, D. T., "Seafloor Geodesy from Repeated Sidescan Sonar Surveys: Optimal Survey and Processing Parameters". The dissertation author was the primary investigator and author of the paper.

Chapter 5, in full, is a reprint of the material as it will appear in the Journal of Navigation: DeSanto, J. B., C. D. Chadwell, D. T. Sandwell, "Kinematic Post-processing of Ship Navigation Data Using Precise Point Positioning", *Journal of Navigation*, accepted. The dissertation author was the primary investigator and author of the paper.

VITA

2008-2013	Bachelor of Science in Geophysics & Bachelor of Science in Physics, University of Texas, Austin, U.S.A.
2013-2018	Graduate Student Researcher, Scripps Institution of Oceanography, University of California, San Diego, U.S.A.
2018	Doctor of Philosophy in Earth Sciences, Scripps Institution of Oceanography, University of California, San Diego, U.S.A.

PUBLICATIONS

DeSanto, J. B., Sandwell, D. T., "Seafloor Geodesy from Repeated Sidescan Sonar Surveys: Optimal Survey and Processing Parameters", in prep.

Cook, M., **J. B. DeSanto**, "Validation of seafloor benchmark stability using structure-from-motion and seafloor pressure data", in prep.

DeSanto, J. B., C. D. Chadwell, D. T. Sandwell, "Kinematic Post-processing of Ship Navigation Data Using Precise Point Positioning", *Journal of Navigation*, 2018.

DeSanto, J. B., D. T. Sandwell, C. D. Chadwell, "Seafloor Geodesy from Repeated Sidescan Sonar Surveys", *J. Geophys. Res. Solid Earth*, 121, pp.4800-4813, 2016.

ABSTRACT OF THE DISSERTATION

Measuring Seafloor Displacement using Repeated Sidescan Sonar Surveys

by

John B. DeSanto

Doctor of Philosophy in Earth Sciences

University of California San Diego, 2018

David T. Sandwell, Chair

The purpose of this thesis is to propose and develop a novel tool for measuring seafloor displacement using repeated sidescan sonar surveys, a data set that is collected alongside multibeam bathymetry. Chapter 1 presents the motivation for this study and introduces the work done in subsequent chapters. Chapter 2 is a brief overview of the design and underlying physics of the multibeam sonar, and presents a discussion on the uncertainties introduced by errors in the sound velocity profile. Chapter 3 presents the processing method for measuring seafloor displacement from sidescan sonar in detail, and tests this method by measuring synthetic displacements introduced into legacy multibeam data. Chapter 4 presents data collected in calibration surveys during the RR1605 and

SR1704 cruises meant to test this method. We find displacements measurements with RMS uncertainties less than 0.5 m under optimal survey designs involving speeds less than 6 knots, kinematic post-processed ship navigation, and frequent measurements of the sound velocity profile. Chapter 5 demonstrates the improvement in ship positioning obtained when performing kinematic post-processing on the raw ship navigation data rather than relying on the real-time navigation solution.

Chapter 1

Introduction

1.1 Justification for Seafloor Geodesy

Geodesy is the study of the shape of the Earth, and is a field critical to natural hazard monitoring of geologic phenomena such as earthquakes and volcanoes because space geodetic techniques such as Global Positioning System (GPS) and Interferometric Synthetic Aperture Radar (InSAR) give us a means of measuring surface deformation associated with these hazards. GPS measurements give us a means of directly measuring plate motion and serve as boundary conditions for plate models such as the one reported in Bird et al [2003]. These models are used to predict the global distribution of earthquakes as well as the style of faulting in a particular region. On a local scale, GPS may be used to measure differential motion across faults as is done in Platt and Becker [2010], giving us information about where strain between plates is being accommodated. After an earthquake, GPS and InSAR may be used to measure the coseismic and postseismic surface deformation associated with the earthquake, which we may use to probe the geometry and frictional properties of faults at depth. Volcanoes may be probed in a similar fashion; InSAR provides measurements of surface deformation due to the buildup

of magma in the subsurface. These measurements are important boundary conditions in models estimating the size of subsurface magma chambers.

However, a significant fraction of earthquakes and volcanic activity occur offshore, due to the simple fact that many of the tectonic plate boundaries occur in these regions. The largest recorded earthquakes are all megathrust earthquakes that occurred in offshore subduction zones; these include the 1960 Chile earthquake, the 1964 Alaska Earthquake, the 2004 Sumatra earthquake, and the 2011 Tohoku-Oki earthquake. Studying this class of earthquakes is particularly important as not only do they pose a risk due to ground shaking, but also associate with destructive tsunamis such as those that followed the Sumatra and Tohoku-Oki eathquakes. Accurate offshore measurements are required to model the source of these tsunamis as shown in Melgar and Bock [2013], but we cannot rely upon GPS and InSAR to collect these measurements as in the terrestrial case because the microwave radiation critical to the function of these methods cannot penetrate seawater deeper than a few millimeters. Instead, we must adapt a parallel set of tools to collect geodetic measurements in a marine environment; we refer to this specialized field as the field of seafloor geodesy.

1.2 Seafloor Geodetic Techniques

An in-depth discussion of the current state of seafloor geodetic techniques is presented in the Burgmann and Chadwell [2014] review paper. A significant challenge in collecting seafloor geodetic data stems from the fact that seafloor geodetic monuments are remote, often being located far offshore and by definition underwater. As a result, instruments and infrastructure (such as cabled arrays) designed for seafloor deployment are more expensive than their terrestrial counterparts because they need to be designed and built to operate under high pressure. In addition, simply traveling to a monument is

more expensive because of the costs associated with operating a research vessel. Seafloor geodetic techniques can be divided into three primary categories of instruments, GPS-Acoustic, ocean bottom pressure sensor and tiltmeters, and sonar (Figure 1.1, each of which represents a slightly different approach to surmounting the technological barriers inherently present in collecting in seafloor geodetic data.

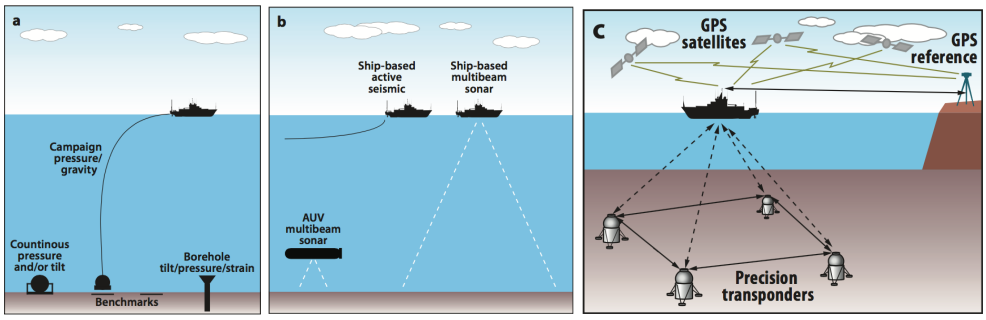

Figure 1.1: **Schematic diagram of seafloor geodetic techniques, including ocean bottom pressure (a), multibeam sonar (b), and GPS-Acoustic (c). Figure taken from** [Bürgmann and Chadwell 2014].

GPS-Acoustic was first proposed by Spiess [1985], and takes advantage of acoustic waves to measure the distance between a set of transponders on the seafloor and a waypoint (traditionally a research vessel) on the sea surface analogous to how a GPS receiver measures the distance between an antenna and satellite. However, unlike GPS, which uses multiple satellites to triangulate the position of the antenna, GPS-Acoustic instead ranges the distance between multiple transponders and a single sea surface waypoint. These transponders are deployed in a concentric circle on the seafloor, a geometry that allows the center of the array to appear stable when the ranges are averaged despite the constant real and apparent vertical and horizontal motion of the waypoint due to swell and internal waves. The location of the sea surface waypoint is measured in a stable reference frame using GPS; this may be used to locate the center of the GPS-Acoustic array which is measured relative to the waypoint. GPS-Acoustic measurements may yield

displacement measurements accurate to approximately a centimeter in the horizontal components and a few centimeters in the vertical component, and have since been used to measure the relative plate motion between the Juan de Fuca and North American Plates [Spiess et al. 1998] as well as the coupling between the Nazca and South American Plates offshore Peru [Gagnon, Chadwell, and Norabuena 2005]. Perhaps most excitingly, GPS-Acoustic measurements captured not only the cosiesmic [Sato et al. 2011] and postseismic [Watanabe et al. 2014] seafloor deformation from the 2011 Tohoku-Oki earthquake offshore Japan, but also a glimpse of the interseismic deformation preceding the earthquake [Sato et al. 2013].

Ocean bottom pressure sensors have been adapted to operate in a high pressure environment such as is present on the seafloor. They are capable of measuring vertical displacement with centimeter accuracy but have no sensitivity to motion in the horizontal components. A longstanding problem with ocean bottom pressure sensors is random instrument drift that may bias measurements made long after initial deployment, but recent engineering developments have led to improved instruments such as the self-calibrating seafloor pressure recorder [Sasagawa and Zumberge 2013]. Ocean bottom pressure recorders have been used to monitor vertical displacements at Axial Seamount, an active underwater volcano located on the Juan de Fuca Ridge, measuring inflation and deflation of the magma chamber prior to the 2012 eruption [Nooner and Chadwick 2009; Chadwick et al. 2012] and 2015 eruption [Sasagawa, Cook, and Zumberge 2016; Nooner and Chadwick 2016], the latter study incorporating measurements from the Cascadia Cabled Array. Pressure sensors have also been used to measure signals resulting from a slow slip event in the Hikurangi subduction margin [Wallace et al. 2016]. In addition, pressure sensors have been deployed in the DONET cabled array offshore Japan for the purposes of real-time tsunami monitoring [Baba, Takahashi, and Kaneda 2014].

The final class of instruments useful for seafloor geodetic application is multibeam

sonar. Multibeam sonar is a tool that is mounted on the hull of a research vessel or AUV that is used to measure seafloor bathymetry using the reflections of acoustic pulses. Multibeam bathymetry has a horizontal resolution generally on the order of 100-150 m for seafloor deeper than 2000 m, making it the highest resolution information on seafloor topography available to us. The geodetic application of these data is conceptually straightforward; taking the difference between two bathymetry surveys before and after can give us information such as the extent of extrusions during a volcanic erution. This has been done to map the extent of eruptions at Axial Seamount both by Fox [1992] using a hull-mounted multibeam sonar and Caress et al [2012] using an AUV-mounted multibeam sonar, as well as the uplift along the Nazca-South America subduction zone due to the 2010 M_ω 8.8 Maule earthquake [Maksymowicz et al. 2017]. Horizontal deformation may be measured by performing a cross-correlation between surveys, as was done to measure deformation across the Japan Trench during the 2011 Tohoku-Oki earthquake by Fujiwara et al [2011; 2017]. Multibeam sonar-derived displacements are unique among seafloor geodetic measurements in that they cover a broad area rather than a point as in the case for GPS-Acoustic and ocean bottom pressure measurements. However, this comes at the cost of accuracy; the displacements measured by the Fujiwara studies have uncertainties on the order of 10 m rather than the centimeter accuracy obtainable using other methods. For this reason, multibeam sonar is a tool that may be further developed for seafloor geodetic application.

1.3 Thesis Summary

The goal of this thesis is to describe and test an improved method for measuring seafloor displacements with multibeam sonar, utilizing the sidescan backscatter amplitude data collected simultaneously with multibeam bathymetry rather than the bathymetry

itself. As will be discussed in Chapter 2, sidescan data have a few advantages over bathymetry, the primary advantage being that the resolution of sidescan data is independent of seafloor depth, at least in the range dimension. Whereas the resolution of bathymetry may be 100-150 m or more dependent on the seafloor depth, the slant range resolution of sidescan data collected with a 12 kHz sonar is on the order of 11.25 m, meaning that when we compare reference and repeated sidescan tracks for displacement analysis, we might expect to be able to measure displacements on the meter scale rather than the decameter scale. In addition, the sidescan data are less susceptible to roll biases than multibeam bathymetry. Thus, we expect these data to be more straightforward to process and yield a more precise measurement. This thesis will explore the viability of sidescan data for seafloor geodetic application in the following chapters:

Chapter 2 is a brief overview of the multibeam sonar, discussing the design of the instrument as well as the physics governing the resolution of bathymetry and sidescan. This chapter also includes a brief discussion of how uncertainties in the sound velocity profile of the ocean affect the multibeam and sidescan measurements. Because multibeam sonars employ acoustic waves, any variation in the sound velocity profile will result in a distorted measurement, so it is imperative that we develop a satisfactory way to address sound velocity variations if we hope to obtain precise and accurate seafloor displacement measurements.

Chapter 3 is a description of the data processing employed to measure displacement using repeated sidescan sonar surveys. The method described entails performing digital image correlation on repeated sidescan sonar surveys and solving for the track displacement that yields the maximum correlation. This processing is tested using legacy data available from previous cruises conducted offshore Cascadia and offshore Southern California. These cruises contain repeated multibeam sidescan surveys collected within a few days of one another. Because of the short time frame between repeated tracks we

expect no measurable seafloor displacement; these surveys are suitable for calibrating the data processing. Because we only have single pairs of repeat tracks, we probe the precision of the measurements by introducing a synthetic displacement into one of the repeat tracks but not the other; we verify the efficacy of our technique by attempting to measure this synthetic displacement. We demonstrate that meter-level precision is obtainable in the range dimension but not the along-track dimension.

Chapter 4 is a presentation of data collected during the 2016 RR1605 research cruise, which was specifically designed as a calibration survey for assessing the displacement accuracy obtainable using the method proposed in Chapter 3. This is done by measuring the displacement between four sets of five repeating sidescan sonar surveys collected within a 40-hour period. These repeated surveys were collected with varying ship speed and track separation, allowing us to infer the optimal survey design for collecting sidescan sonar data for geodetic application. This chapter also includes an assessment of the uncertainty expected from variations in the sound velocity profile during this cruise, derived from expendable bathythermograph (XBT) measurements collected during the cruise.

Chapter 5 analyzes the ship navigation data collected during the RR1605 cruise. Bathymetry and sidescan measurements are made relative to the research vessel; if we do not precisely know the location of the research vessel we cannot infer the location of a point on the seafloor. However, the remote nature of seafloor geodetic surveys means that we may not always be close enough to a land GPS station to obtain a differential GPS solution. Thus, we employ Precise Point Positioning (PPP) to obtain a post-processed kinematic GPS solution of the ship navigation. We assess the accuracy of the PPP method by calculating the location of a continuous land station (AB21) on the Aleutian islands using three independent processing methods: GIPSY-OASIS, PANDA, and CSRS. We then compare the PPP solutions of the RR1605 cruise to assess the noise added by the

moving platform. This is done for both the ship navigation and a campaign-style GPS receiver deployed on the deck during the cruise. We compare these solutions to the real-time ship navigation solution to quantify the improvement in location accuracy obtained by the kinematic post-processing.

References

Baba, Toshitaka, Takahashi, Narumi, and Kaneda, Yoshiyuki (2014). "Near-field tsunami amplification factors in the Kii Peninsula, Japan for Dense Oceanfloor Network for Earthquakes and Tsunamis (DONET)". In: *Marine Geophysical Research* 35.3, pp. 319–325. DOI: 10.1007/s11001-013-9189-1. URL: https://doi.org/10.1007/s11001-013-9189-1.

Bird, Peter (2003). "An updated digital model of plate boundaries". In: *Geochemistry, Geophysics, Geosystems* 4.3. DOI: 10.1029/2001GC000252.

Bürgmann, Roland and Chadwell, David (2014). "Seafloor Geodesy". In: *Annual Review of Earth and Planetary Sciences* 42.1, pp. 509–534. DOI: 10.1146/annurev-earth-060313-054953.

Caress, D W, Clague, D A, Paduan, J B, Martin, J F, and Dreyer, B M (2012). "Repeat bathymetric surveys at 1-metre resolution of lava flows erupted at Axial Seamount in April 2011". In: *Nat. Geosci.* 5, p. 483.

Chadwick, William W., Nooner, Scott L., Butterfield, David A., and Lilley, Marvin D. (2012). "Seafloor deformation and forecasts of the April 2011 eruption at Axial Seamount". In: *Nature Geosci* 5 (7), pp. 474–477. DOI: http://dx.doi.org/10.1038/ngeo1464.

Fox, Christopher G., Chadwick, William W., and Embley, Robert W. (1992). "Detection of changes in ridge-crest morphology using repeated multibeam sonar surveys". In: *Journal of Geophysical Research: Solid Earth* 97.B7, pp. 11149–11162. ISSN: 2156-2202. DOI: 10.1029/92JB00601. URL: http://dx.doi.org/10.1029/92JB00601.

Fujiwara, T, Kodaira, S, No, T, Kaiho, Y, Takahashi, N, and Kaneda, Y (2011). "The 2011 Tohoku-oki earthquake: displacement reaching the trench axis". In: *Science* 334, p. 1240.

Fujiwara, Toshiya, Christian, Santos Ferreira, Katharina, Bachmann Anna, Michael, Strasser, Gerold, Wefer, Tianhaozhe, Sun, Toshiya, Kanamatsu, and Shuichi, Kodaira (2017). "Seafloor Displacement After the 2011 Tohoku-oki Earthquake in the Northern Japan Trench Examined by Repeated Bathymetric Surveys". In: *Geophysical Research Letters* 44.23, pp. 11,833–11,839. DOI: 10.1002/2017GL075839.

Gagnon, Katie, Chadwell, C. David, and Norabuena, Edmundo (Mar. 2005). "Measuring the onset of locking in the Peru-Chile trench with GPS and acoustic measurements". In: *Nature* 434.7030, pp. 205–208. URL: http://dx.doi.org/10.1038/nature03412.

Maksymowicz, A., Chadwell, C. D., Ruiz, J., Trhu, A. M., Contreras-Reyes, E., Weinrebe, W., Daz-Naveas, J., Gibson, J. C., Lonsdale, P., and Tryon, M. D. (2017). "Coseismic seafloor deformation in the trench region during the Mw8.8 Maule megathrust earthquake". In: *Scientific reports* 7. DOI: doi:10.1038/srep45918.

Melgar, Diego and Bock, Yehuda (2013). "Near-field tsunami models with rapid earthquake source inversions from land- and ocean-based observations: The potential for forecast and warning". In: *Journal of Geophysical Research: Solid Earth* 118.11, pp. 5939–5955. DOI: 10.1002/2013JB010506.

Nooner, Scott L. and Chadwick, William W. (2009). "Volcanic inflation measured in the caldera of Axial Seamount: Implications for magma supply and future eruptions". In: *Geochemistry, Geophysics, Geosystems* 10.2, n/a–n/a. ISSN: 1525-2027. DOI: 10.1029/2008GC002315. URL: http://dx.doi.org/10.1029/2008GC002315.

— (2016). "Inflation-predictable behavior and co-eruption deformation at Axial Seamount". In: *Science* 354.6318, pp. 1399–1403. DOI: 10.1126/science.aah4666.

Platt, John P. and Becker, Thorsten W. (2010). "Where is the real transform boundary in California?" In: *Geochemistry, Geophysics, Geosystems* 11.6. DOI: 10.1029/2010GC003060. URL: https://agupubs.onlinelibrary.wiley.com/doi/abs/10.1029/2010GC003060.

Sasagawa, G., Cook, M. J., and Zumberge, M. A. (2016). "Drift-corrected seafloor pressure observations of vertical deformation at Axial Seamount 20132014". In: *Earth and Space Science* 3.9, pp. 381–385. DOI: 10.1002/2016EA000190.

Sasagawa, G. and Zumberge, M. A. (2013). "A Self-Calibrating Pressure Recorder for Detecting Seafloor Height Change". In: *IEEE Journal of Oceanic Engineering* 38.3, pp. 447–454. ISSN: 0364-9059. DOI: 10.1109/JOE.2012.2233312.

Sato, Mariko, Ishikawa, Tadashi, Ujihara, Naoto, Yoshida, Shigeru, Fujita, Masayuki, Mochizuki, Masashi, and Asada, Akira (2011). "Displacement Above the Hypocenter of the 2011 Tohoku-Oki Earthquake". In: *Science* 332.6036, p. 1395. DOI: 10.1126/science.1207401.

Sato, Mariko, Fujita, Masayuki, Matsumoto, Yoshihiro, Ishikawa, Tadashi, Saito, Hiroaki, Mochizuki, Masashi, and Asada, Akira (2013). "Interplate coupling off northeastern Japan before the 2011 Tohoku-oki earthquake, inferred from seafloor geodetic data". In: *Journal of Geophysical Research: Solid Earth* 118.7, pp. 3860–3869. DOI: 10.1002/jgrb.50275. URL: https://agupubs.onlinelibrary.wiley.com/doi/abs/10.1002/jgrb.50275.

Spiess, F N (1985). "Suboceanic geodetic measurements". In: *IEEE Trans. Geosci. Remote Sens.* GE-23, p. 502.

Spiess, F. N., Chadwell, C. D., Hildebrand, J. A., Young, L. E., G. H. Purcell, Jr., and Dragert, H. (1998). "Precise GPS/Acoustic positioning of seafloor reference points for tectonic studies". In: *Phys. of the Earth and Plan. Int.* 108, pp. 101–112.

Wallace, Laura M., Webb, Spahr C., Ito, Yoshihiro, Mochizuki, Kimihiro, Hino, Ryota, Henrys, Stuart, Schwartz, Susan Y., and Sheehan, Anne F. (2016). "Slow slip near the trench at the Hikurangi subduction zone, New Zealand". In: *Science* 352.6286, pp. 701–704. ISSN: 0036-8075. DOI: 10.1126/science.aaf2349. eprint: http://science.sciencemag.org/content/352/6286/701.pdf. URL: http://science.sciencemag.org/content/352/6286/701.

Watanabe, Shunichi, Sato, Mariko, Fujita, Masayuki, Ishikawa, Tadashi, Yokota, Yusuke, Ujihara, Naoto, and Asada, Akira (2014). "Evidence of viscoelastic deformation following the 2011 Tohoku-Oki earthquake revealed from seafloor geodetic observation". In: *Geophysical Research Letters* 41.16, pp. 5789–5796. ISSN: 1944-8007. DOI: 10.1002/2014GL061134.

Chapter 2

Physical Principles of Multibeam Sonar for Mapping of the Seafloor

2.1 Introduction

A multibeam sonar mounted on the hull of a large research vessel provides an important tool for mapping the seafloor in the deep ocean at moderate spatial resolution and accuracy (Figure 2.1). This chapter provides a very brief introduction into the physical principles of a particular multibeam echo sounder that is able to map in the deepest ocean at approximately 100 m spatial resolution. The overall geometry is shown in Figure 2.1. The ship cruises along the surface of the ocean at a speed typically less than 12 knots (i.e. 6 m/s). It emits a sonar signal from hull-mounted transducers. These acoustic waves reflect from the seafloor and return to the ship mapping out a swath of seafloor 3-4 times the ocean depth. Some basic references for the method and technology are Farr [1980], de Moustier, [1988], and Kongsberg, [2011].

The sonar elements are mounted in a gondola or pod (Figure 2.2) that is fastened to the deepest part of the hull of the ship where it will remain submerged even in rough

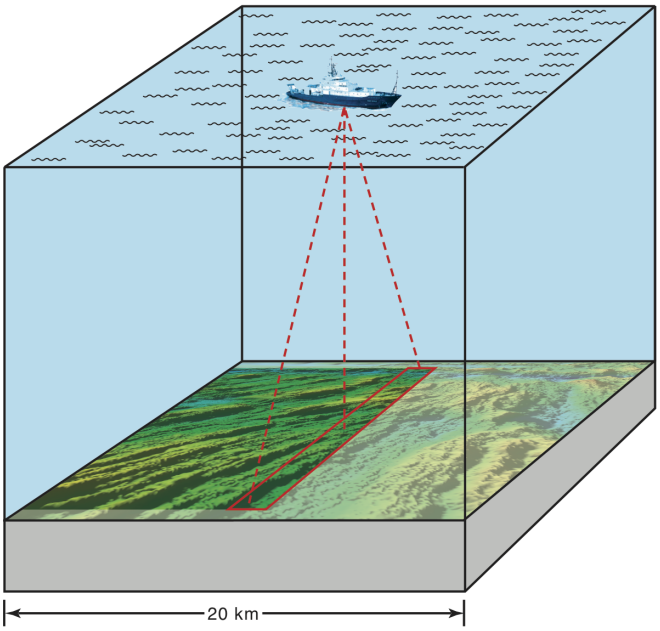

Figure 2.1: **Schematic diagram of a multibeam echo sounder mapping a swath of seafloor.**

seas. The sonar consists of two arrays. Sound pulses are generated by a 7 m long array of transducers that are oriented parallel to the keel of the ship (Figure 2.2, EM122 TX). The return echoes are recorded in a 7 m long array of hydrophones oriented perpendicular to the keel of the ship (Figure 2.2, EM122RX). In this chapter we will try to answer some basic questions such as: Why are the transmit and receive arrays so long? Why are they arranged in a T structure? Since the gondola is fixed to the hull of the ship, what happens when the ship undergoes yaw, pitch, and roll motions? The first part of the chapter will be related to some basic physical principles of sonar propagation in seawater and beam forming. These physical properties guide the overall design and limitations of the multibeam approach for seafloor mapping. What is missing from this chapter is a description of the marvelous and sophisticated engineering that has gone into the

development and refinement of these systems.

Figure 2.2: **Gondola containing a 7 m long array of transducers (EM122 TX) that are oriented parallel to the keel of the ship and a 7 m long array of hydrophones (EM122 RX) perpendicular to the keel. This system is a Kongsberg EM122 multibeam sonar being mounted on the hull of the RV Langseth. (Photo credit, John Greene, [*Seeing with Sound*]).**

Much of the physics of multibeam sonar is similar to radar interferometry mapping of topography by satellites. The major difference is that satellites provide a very stable platform where the position and orientation vary smoothly with time, so the motion compensation corrections are simple and accurate. In contrast the ship is constantly undergoing extreme motions and rotations at periods that are shorter than the two-way travel time of the sonar echoes. The compensation for these motions is easy to understand from a physical perspective (this chapter) but enormously challenging from an engineering perspective.

2.2 Mapping Geometry

The objective is to measure ocean depth in a swath perpendicular to the track of the ship one cross-track profile for each ping of the sonar. The geometry is illustrated in Figure 2.3 where the ship is on the ocean surface and moving into the page. Consider a sound pulse that is emitted from the hull at a look angle of θ from the vertical. The pulse travels at the speed of sound c along the ray path labeled ρ. It reflects from the seafloor and returns to the ship. The range is estimated from the two-way travel time Δt as $\rho = \Delta t/c$. The estimated depth at that location is $H(\theta) = \rho/\cos\theta$. Therefore in addition to the range measurement, the look angle of the return pulse must be accurately estimated. We will discuss the principles and limitations of forming a narrow sonar beam in the next section.

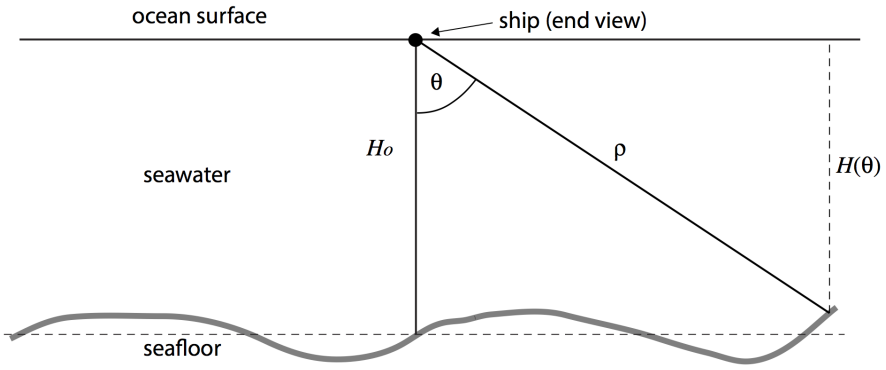

Figure 2.3: **Schematic diagram of a ray of sound energy, emitted at a look angle of θ, from a ship moving into the page. H_0 is the depth directly beneath the ship at zero look angle. The off-nadir depth is $H(\theta) = \rho/\cos\theta$.**

The maximum look angle of this mapping is limited by three effects. (1) First the outgoing pulse will not send all of its energy in the look direction and some fraction will be emitted in the vertical direction through a side lobe of the sonar beam (discussed below). The backscattered energy is highest at a vertical look angle so significant energy

can come from this nadir reflection but more importantly there will be significant energy in the first multiple of the pulse. The 2-way travel time of the first multiple at nadir is equal to the 2-way travel time of a single reflected pulse at a 60° look angle assuming equal ocean depth at these two locations. Therefore at look angles of 60° and higher the double bounce will arrive at or before the off-nadir reflected pulse and the sonar will have difficulty to uniquely identify the travel time of the main reflection. This limits the swath to about 3.5 times the ocean depth although larger widths are possible with sector illumination techniques discussed below. (2) The second limitation is related to a non-uniform sound velocity in the upper ocean. This will cause the ray path to bend mostly outward (away from the look angle); at extreme look angles approaching 90°, the outgoing ray may never reach the ocean floor. (3) The third limitation is related to the attenuation of the sonar pulse as it passes through the ocean. If the attenuation is very strong then the sonar will not be able to detect energy from the return pulse. The selection of an acceptable sonar frequency for deep ocean mapping is discussed next.

2.3 Selection of Sonar Frequency

A main objective of this system is to have the ability to map the seafloor at all ocean depths. A significant limitation of sonar is the attenuation of energy as the waves propagate through the ocean. High frequency waves are more strongly attenuated than lower frequency waves as shown in Figure 2.4. Commonly used sonar frequencies are provided in Table 2.1 along with the wavelength for a nominal sound speed of 1500 m/s. The table also provides the propagation distance where the waves are attenuated by 1/4 of their initial power [Ainslie and McColm 1998]. The median ocean depth is about 4 km as illustrated in the hypsometry of the ocean (Figure 2.5) [Becker and Sandwell 2007]. The maximum ocean depth in the Mariana trench is about 11 km but most of the seafloor

lies at depths less than 6 km. As discussed above the range to the outermost beam having a look angle of 60° is two times the nadir ocean depth. Therefore, a lower frequency sonar (12 kHz) is needed to obtain full swath coverage at the most common 4 km ocean depth and also have the ability to map at 8 km depth with a narrower swath. From this analysis we have constrained the wavelength of our sonar to be longer than about 0.12 m. Next we will see how this effects the ability to focus the sonar beam.

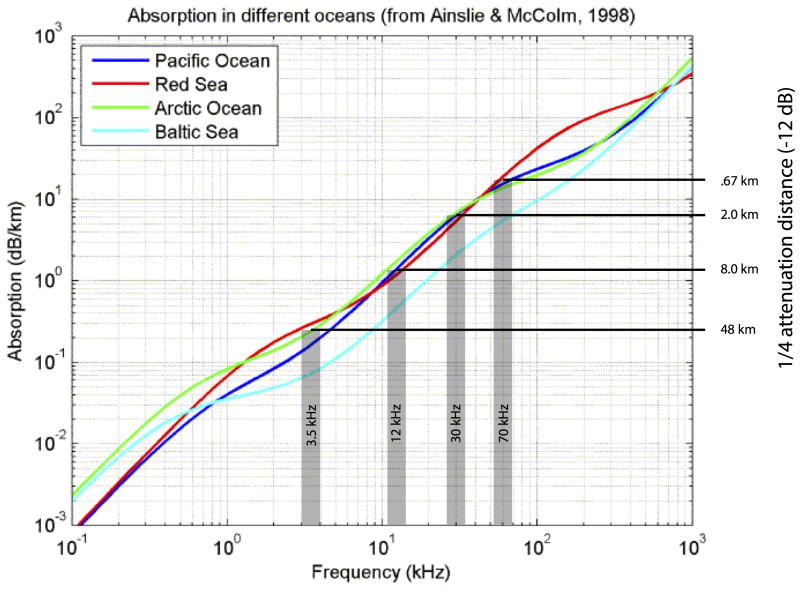

Figure 2.4: **Absorption of sonar power per km of propagation as a function of frequency for several bodies of seawater. The right axis shows the length where the sonar power is attenuated by 1/4. Lower frequency sonars (e.g., 3.5 kHz) can propagate long distances (about 48 km) and retain detectable power while high frequency sonars (e.g., 70 kHz) suffer significant loss over much shorter distances (about 0.67 km) (modified from Ainslie and McColm, [1998]).**

Table 2.1: **Characteristics of sonar in the ocean.**

f - frequency (kHz)	λ - wavelength (m)	α - $\frac{1}{4}$ attenuation distance (km)	wavelength analogy for radar
3.5	0.43	48	P
12	0.13	8	S
30	0.05	2	C
70	0.02	0.7	X

2.4 Fraunhoffer Diffraction

The beam width of a sonar pulse is governed by the principles of Fraunhoffer diffraction. Consider a coherent sonar pulse generated across an aperture of length L as shown in Figure 2.6. First we'll consider a 1-D aperture and then go on to a 2-D rectangular aperture to simulate a rectangular array of transducers or hydrophones as shown in Figure 2.2. The 2-D case provides the shape and dimension of the footprint of the sonar. These notes were developed from Rees [2001] and Bracewell [1978] for electromagnetic radiation but the principles are equivalent for sonar.

We simulate coherent radiation by numerous point sources of sound (transducers) distributed along the aperture between $-L/2$ and $L/2$. For simplicity we'll assume all the sources have the same amplitude, wavelength λ, and phase. Given these sources of radiation, we solve for the illumination pattern on the screen as a function of θ. We'll assume that the screen is far enough from the aperture so that rays AP and OP are parallel. Later we will determine how far away the screen needs to be in order for this approximation to hold. Under these conditions, the ray AP is slightly shorter than the ray OP by an amount $-y\sin\theta$. This corresponds to a phase shift of $\frac{-2\pi}{\lambda}y\sin\theta$. The amplitude of the illumination at point P is the integral over all of the sources along the aperture

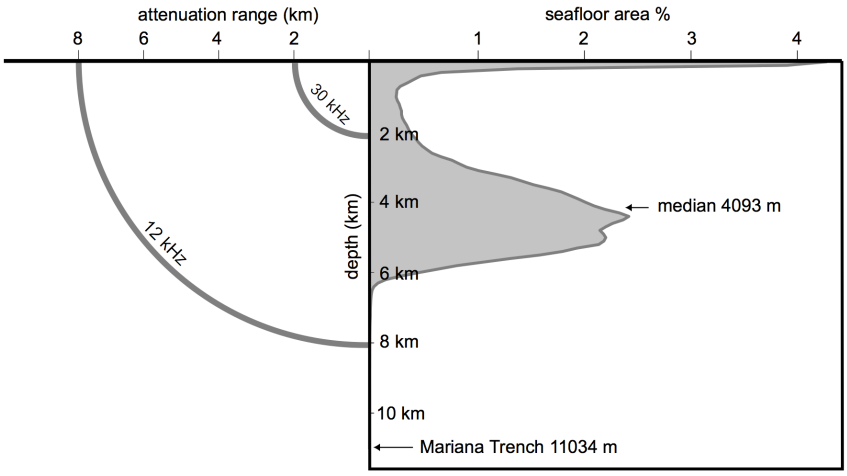

Figure 2.5: **(left) Attenuation range for sonar waves in the ocean at 30 kHz and 12 kHz. (right) Histogram of area of seafloor as a function of depth. The median ocean depth is about 4 km and most of the ocean is shallower than 8 km. Deep ocean mapping requires lower sonar frequencies (12 kHz).**

multiplied by their complex phase value

$$P(\theta) = \int_{-L/2}^{L/2} A(y) e^{-i2\pi y k \sin\theta} dy \tag{2.1}$$

where $k = 1/\lambda$. This is called the Fraunhoffer diffraction integral. The illumination across the aperture is uniform in both amplitude and phase so we set $A(y) = 1$. Later we will adjust the phase across the aperture to shift the peak in the energy away from $\theta = 0$. Now let $s = 2\pi k \sin\theta$ so the integral is easy to evaluate.

$$P(s) = \int_{-L/2}^{L/2} e^{-isy} dy = \frac{e^{-isL/2} - e^{isL/2}}{-is} = \frac{2}{s}\sin(sL/2) = L\mathrm{sinc}(sL/2) \tag{2.2}$$

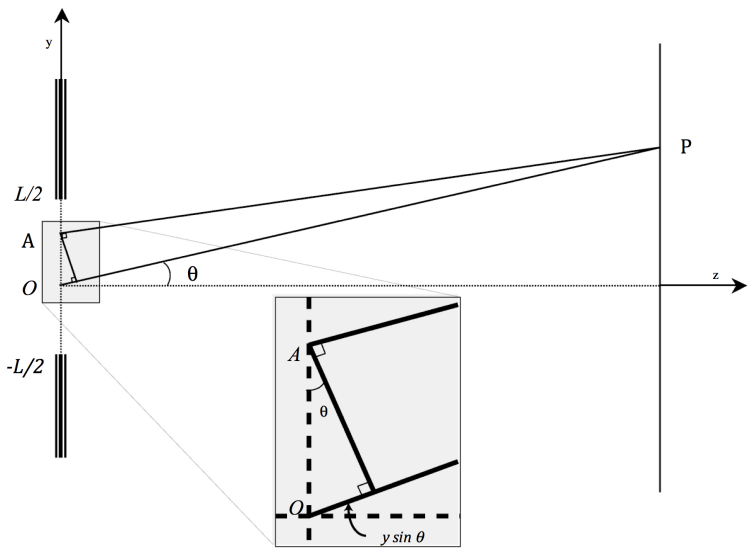

Figure 2.6: **Diagram for the projection of coherent sound waves on a screen (e.g. seafloor) that is far from the aperture of length L.**

Replacing s with $2\pi\sin\theta/\lambda$ we arrive at the final result.

$$P(\theta) = L\text{sinc}\left(\frac{L\pi\sin\theta}{\lambda}\right) \tag{2.3}$$

The illumination pattern on the screen is shown in Figure 2.7 (solid curve).

The first zero crossing, or angular resolution θ_r of the sinc function occurs when the argument is π so

$$\sin\theta_r = \lambda/L. \tag{2.4}$$

At this point it is instructive to calculate the angular resolution of the aperture of the EM122 system shown in Figure 2.2. The length of this aperture is 7 m and we use a 0.13 m wavelength sonar to reach full ocean depth. Given these values and equation (2.4) we find an angular resolution of 1°. If we constructed TX and RX arrays 10 times smaller with an aperture length of say 0.7 m then the angular resolution of the two arrays

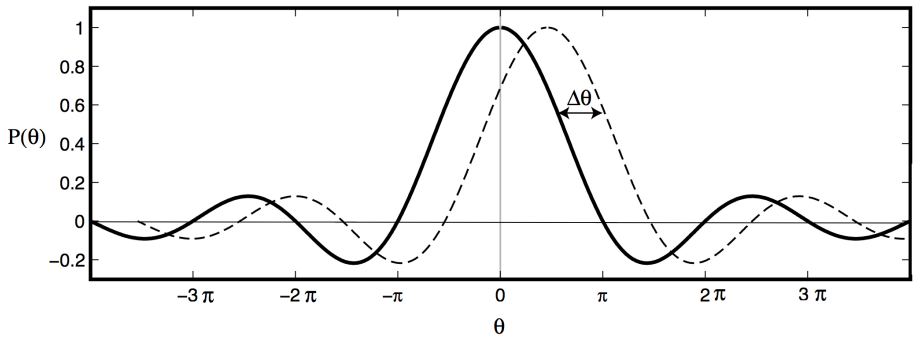

Figure 2.7: **Sinc function illumination pattern for the aperture shown in Figure 2.6. Solid curve is for uniform phase across the aperture. Dashed curve is for a linear phase ramp across the aperture to shift the location of the peak by $\Delta\theta$.** (Modified from [Sandwell et al. 2016].)

would be 10°. At an ocean depth of 4 km this would correspond to a spatial resolution of 700 m, which is inadequate for many mapping purposes. Figure 2.2 also shows the location of a 12 kHz transducer having a diameter of about 0.5 m. This type of transducer would produce a very broad beam that would roughly correspond to the single-beam echo sounders used on research vessels before the multibeam technology was available. So now we have answered the question of why the TX and RX arrays are so long. We need longer wavelength sonar to reach full ocean depth but to resolve features of about 1° the basic physics dictates that the array be approximately 7 meters long. We still have not explained the shorter width of the apertures and their T configuration.

The next modifications to the aperture are to change the amplitude and phase of the transducers (or hydrophones) across the array (i.e., $A(y)$). First, one could modify the amplitude of the illumination across the aperture. For example, a Gaussian aperture would produce a Gaussian illumination function on the screen. This would eliminate the side lobes associated with the sinc function but it would also broaden the projection pattern. Second we could vary the phase of the transponders across the aperture to shift the point of maximum illumination away from $\theta = 0$. We accomplish by linearly varying

the phase of the illumination across the aperture, given by

$$A(y) = e^{i2\pi y k \sin\theta_0}. \tag{2.5}$$

In this case the Fraunhoffer diffraction integral becomes

$$P(\theta) = \int_{-L/2}^{L/2} A(y) e^{-i2\pi y k \sin\theta} dy = \int_{-L/2}^{L/2} e^{-i2\pi y k(\sin\theta - \sin\theta_0)} dy. \tag{2.6}$$

Following the approach above, we integrate and find the result is

$$P(\theta) = L\text{sinc}\left[\frac{L\pi(\sin\theta - \sin\theta_0)}{\lambda}\right]. \tag{2.7}$$

The peak in the projection pattern is shifted by an amount $\Delta\theta = \sin^{-1}(\sin\theta - \sin\theta_0)$ as shown by the dashed line in Figure 2.7. This phased array approach is used to form the off-nadir beams across the swath of the multibeam as described below. Moreover it is used to compensate for the pitch of the ship on the outgoing pulse of the transmit array as well as the roll on the incoming wave fronts of the receive array. A diagram of how the look angle of the incoming sonar waves are electronically shifted away from nadir is shown in Figure 2.8.

Before moving on to the 2-D case, we should check the assumption used in developing the Fraunhoffer diffraction integral that the rays *AP* and *OP* are parallel. Suppose we examine the case when $\theta = 0$; the ray path *AP* is slightly longer than *OP* (Figure 2.9). This parallel-ray assumption breaks down when the phase of ray path *AP* is more than $\pi/2$ radians longer than *OP*, which corresponds to a distance of $\lambda/4$. Let's determine the conditions when this happens.

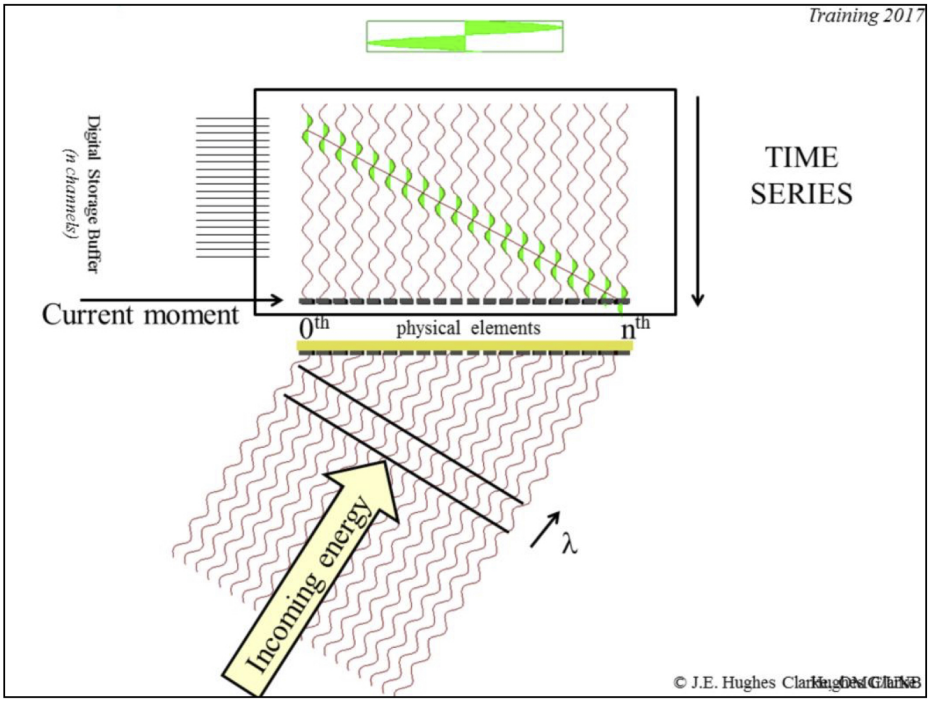

Figure 2.8: **Diagram showing coherent waves from an off-nadir reflection being recorded by an array of hydrophones across an aperture. To extract a time series of the energy arriving from that direction one sums the pulses with an appropriate time delay. (Taken from Clarke [2017])**

The condition that the path length difference is smaller than 1/4 wavelength is

$$\left[\frac{L^2}{4}+z^2\right]^{1/2}-z<\frac{\lambda}{4} \tag{2.8}$$

or can be rewritten as

$$\left[\left(\frac{L}{2z}\right)^2+1\right]^{1/2}-1<\frac{\lambda}{4z}. \tag{2.9}$$

Now assume $L << z$ so we can expand the term in brackets into a binomial series.

$$1+\frac{L^2}{8z^2}-1<\frac{\lambda}{4z} \tag{2.10}$$

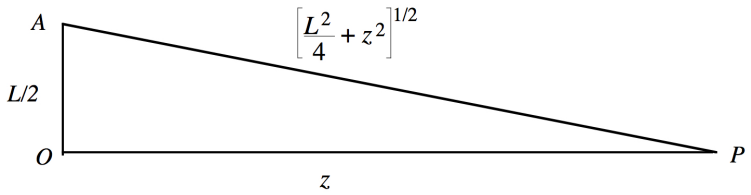

Figure 2.9: **Diagram showing the length of path AP with respect to OP due to an offset of $L/2$. (Taken from [Sandwell et al. 2016] and [Rees 2001].)**

and we find $z_f > \frac{L^2}{2\lambda}$ where z_f is the Fresnel distance. So when $z < z_f$ we are in the near field and we need to use a more rigorous diffraction theory. However when $z >> z_f$ we are safe to use the parallel-ray approximation and the Fraunhoffer diffraction integral is appropriate. As shown in Figure 2.2, our aperture has a length of 7 m and based on the need for 8 km propagation we have selected a wavelength of 0.13 m. For this case the Fresnel distance is 188 m. We will mainly be using this system to map areas greater than 200 m depth so the parallel ray approximation is valid.

2.5 2-D Aperture

A 2-D rectangular aperture is a good approximation for both the transmit and receive arrays shown in Figure 2.2. The transmit aperture is longer in the keel direction (length L) than in the perpendicular direction (width W) as shown in Figure 2.2. As in the 1-D case, one uses a 2-D Fraunhoffer diffraction integral to calculate the projection pattern of the antenna. The integral is

$$P(\theta_x,\theta_y) = \int_{-L/2}^{L/2}\int_{-W/2}^{W/2} A(x,y)\exp\left[i\frac{2\pi}{\lambda}(x\sin\theta_x + y\sin\theta_y)\right]dxdy \tag{2.11}$$

where λ is the wavelength of the radar. As in the 1-D case we will assume the aperture $A(x,y)$ has uniform amplitude and phase. In this case the projection pattern can be integrated analytically and is

$$P(\theta_x,\theta_y) = LW\,\mathrm{sinc}\left(\frac{\pi W \sin\theta_x}{\lambda}\right)\mathrm{sinc}\left(\frac{\pi L \sin\theta_y}{\lambda}\right). \tag{2.12}$$

The first zero crossing of this 2-D sinc function is illustrated in Figure 2.10 (right).

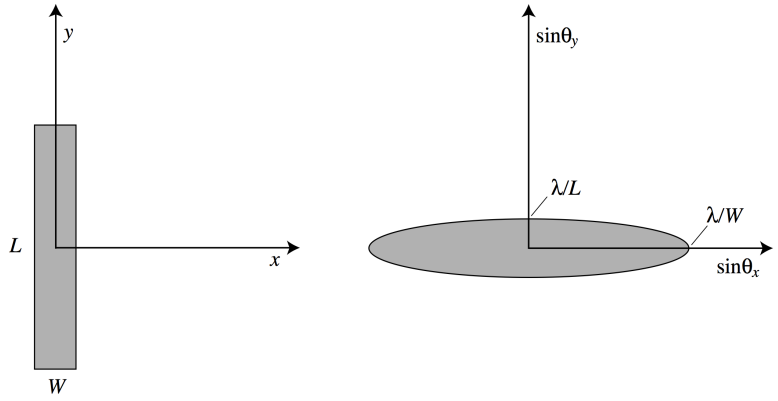

Figure 2.10: **Diagram showing the projection pattern (right) for a rectangular aperture (left). (Taken from [Sandwell et al. 2016] and [Rees 2001].)**

2.6 Mills Cross Configuration

High 2-D resolution of a patch of seafloor can be achieved by setting the transmit array with the long axis along the keel of the ship and the long axis of the receive array in the perpendicular direction; this is called a Mills cross configuration. The beam pattern on the seafloor is shown in Figure 2.11.

In the case of the Konsberg EM122, the transmit array has a length of 7.8 m and a width of 0.78 m resulting in a 0.92° resolution in the along-track direction and a

9.2° resolution across the track. As discussed above, the overall swath width can be 150°, which is significantly wider than the 9.2° cross track angle. Indeed the transmit array has 18 elements along the keel and 6 elements across the keel. The 6 cross-track elements are used to focus the outgoing beam in up to 9 sectors in the cross track direction. Each ping of the sonar actually consists of 9 pings with a slight time and frequency offset to ensonify the entire 150° swath, or whatever swath width was selected by the user. Some examples of the hydrophone records from the receive array (called stave data) for the 9 sectors are shown in the next section.

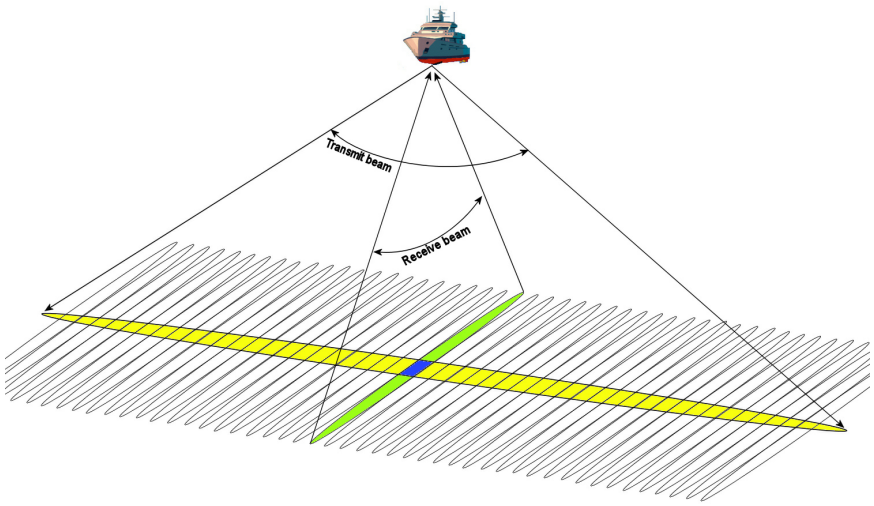

Figure 2.11: **Schematic diagram of the beam patterns of transmit (yellow) and receive (green) arrays on the seafloor. The intersection of the 0° incidence angle receive beam and the transmit beam is shown as a blue box (1°x1°). The other cross-track beams are resolved by synthesizing a non-nadir focus in the computer after the data are collected on all the hydrophones of the receive array.**

The receive array is 7.2 m in the across-keel directions and 0.42 m along the keel resulting in a cross-track resolution pattern of 0.99° and an along-track resolution of 17.3°. The receive array has 128 hydrophones (or staves) having the ability to record over a wide bandwidth centered at 12 kHz. All 128 staves record the entire time series of reflected waves over a time window beginning at the time the pulse was emitted and

ending at the two-way travel time of the most distant reflection at a look angle of up to 75°. After the data are recorded, they are first divided into the 9 sectors by frequency filtering and then focussed into cross-track beams by summing with the appropriate time delay. Both operations are performed with the Fast Fourier transform algorithm to speed the processing. An example of the original stave data is shown in Figure 2.12. This example comes from an EM120 with only 64 staves. The range sampling rate is 2 kHz so the first arrivals are at about 3 seconds corresponding to a depth of 2250 m. Note the nadir double bounce arrives at about 6 seconds. After beam forming (right) the horizontal axis corresponds to the sine of the look angle. The higher look angles have two-way travel times of up to 7 seconds corresponding to a distance of 5250 m. (Note that beam forming is simply the FFT of each row of raw stave data with the output shifted so the lowest wavenumber is in the center of the array and corresponds to the nadir beam.)

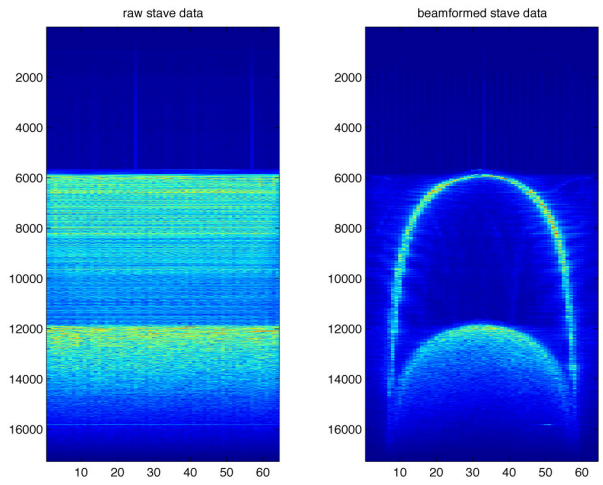

Figure 2.12: **(left) Reflected sonar amplitude versus time in milliseconds (increasing down) and stave number (across). This example comes from an EM120 with 64 staves. The range sampling rate is 2 kHz. (right) Beam formed stave data where the horizontal axis now corresponds to the sine of the look angle.**

As discussed above, 9 individual pings are emitted for each sonar echo and each of these pings has its own center look angle and center frequency as provided in Table 2.2.

Table 2.2: **Sectors and frequencies (Hz) for the Kongsberg EM122.**

Port				Center	Starboard			
1	3	5	7	9	8	6	4	2
11550	12150	12600	11850	12450	11400	12300	11700	11250

For ocean depths greater than 2000 m the bandwidth of each ping is 67 Hz corresponding to a pulse length of 15 ms and a range resolution of 11.25 m. For shallower depth, the bandwidth is increased to 200 Hz corresponding to a range resolution of 3.75 m.

After this pre-processing of the columns into unique look angles θ, a bottom detection algorithm is used to measure the two-way travel time and thus the range ρ for each beam. Then the cross-track depth profile h can be estimated from $h = \rho \cos\theta$ as shown in Figure 2.3:

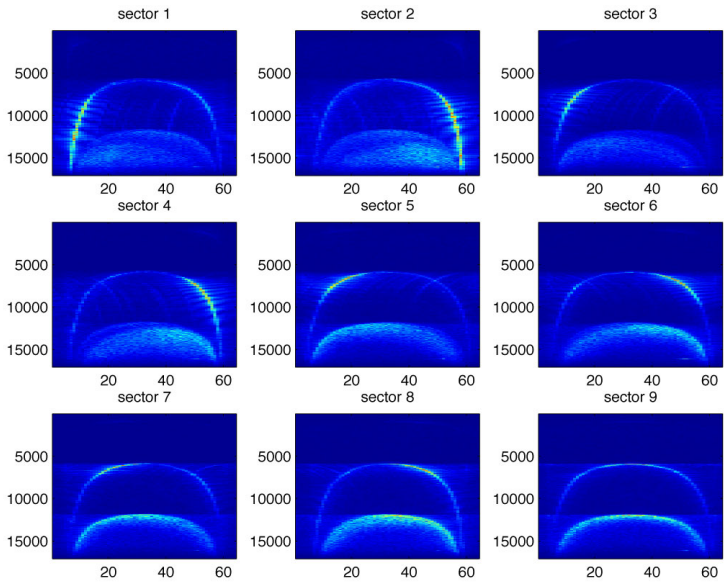

Figure 2.13: **Reflected sonar amplitude versus time in milliseconds (increasing down) and stave number (across), separated by beam sector according to frequency filtering. This example comes from an EM120 with 64 staves. The range sampling rate is 2 kHz.**

2.7 Roll, Pitch, and Yaw Compensation

As discussed in the introduction a major challenge of measuring depth from a ship is that the ocean waves cause the platform to be constantly rotating in all three directions. The geometry of the three important angles is shown in Figure 2.14. An example of a time series of pitch, roll, and heave is provided in Figure 2.15. In this case the roll angle was more than 10 degrees. If this was not corrected it would result in a depth error of more than 1 km on the outermost beam at 7 km from the nadir track line. Achieving better than 10 m of depth error on the outermost beam requires an accuracy of 0.08°. Therefore accurate bathymetry requires an accurate roll correction.

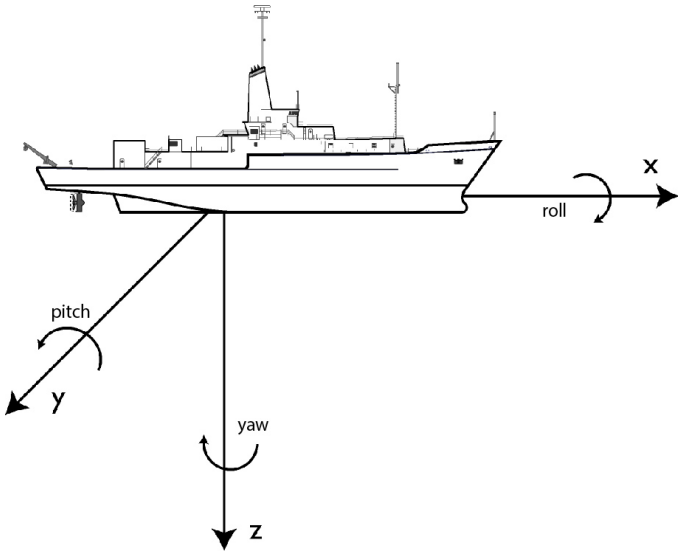

Figure 2.14: **Geometry of roll, pitch, and yaw angles for a ship.**

The sonar provides a real-time correction for pitch and roll angles using a vertical reference unit (VRU) that can record off vertical angles to about 0.01° accuracy. The transmit array ensonifies a narrow beam (about 1°) in the along-track direction. A pitch error of greater than about 0.5° will place the footprint in the wrong location ultimately blurring the seafloor map. The problem is corrected in real time. First the VRU records the pitch and roll angles at 10 Hz. Then the current pitch angle is sent to the sonar

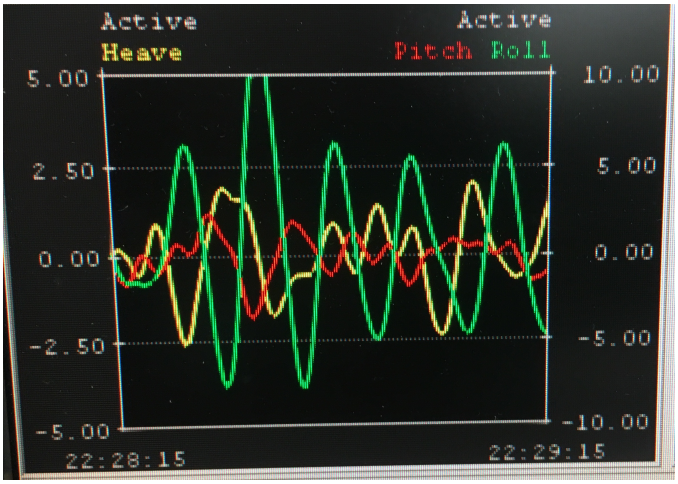

Figure 2.15: **Time series of pitch and roll for 1 minute. Right vertical axis is in degrees.**

where a pitch correction is applied to the transmit array to correct for this angle. The correction to the roll angle can be performed in real time although it can also be done in post processing. Again the roll angle from the VRU is used by the sonar to correct the incidence angle relative to the true vertical. Note that since the return pulse must be recorded for several seconds, the roll correction will be time dependent. This section provides only a conceptual description of these corrections. The engineering behind this rather complicated system is marvelous and sophisticated and beyond the scope of this document.

2.8 Effects of the Sound Speed Profile

Our analysis thus far has assumed a uniform speed of sound C_d in the water column, from which the beam steering is calculated. In the real world, the sound speed varies as a function of temperature and salinity, both of which change with depth. As a result, locations of depth soundings will be improperly estimated because they arrive at slightly different look angles compared to $\theta_d = \theta_{beam} + \theta_{roll}$ predicted by the beam

steering and roll compensation, which is calculated with C_d.

A strategy to address this is detailed in de Moustier [1988]. In principle, the depth H of a point on the seafloor may be calculated as $H(\theta) = \rho \cos\theta = \frac{C_d}{2} t \cos\theta$, where t is the travel time and ρ is the slant range. There are two ways in which this may be modified due to perturbations in the sound speed profile. In the simpler case, the sound speed C_d is accurate except for some sound speed perturbation at the sea surface that may be measured during transit. In this case, the slant range is not affected but the apparent look angle will be bent according to Snell's Law:

$$\frac{\sin\theta'}{C'} = \frac{\sin\theta_d}{C_d} \tag{2.13}$$

As a result, the apparent depth profile is distorted to

$$H'(\theta) = \frac{C_d}{2} t \cos\left(\mathrm{Sin}^{-1}\left[\frac{C'}{C_d}\sin\theta\right]\right). \tag{2.14}$$

We estimate the effect of this distortion in Figure 2.16, which shows the normalized water depth calculated when the surface sound velocity changes by $\pm 6.6\%$, the maximum theoretical change that could result from moving from polar to tropical latitudes [De Moustier 1988]. The difference between true and distorted look angles increases for greater angles, causing greater errors for outer beams.

In addition, there is a possibility that the default sound speed used throughout the profile is wrong, which will affect both the slant range and look angle. The strategy to address this is to compute the average speed of sound by integrating sound speed across the vertical water column:

$$C_{avg} = \frac{1}{H_0}\int_0^{H_0} C(z)dz \tag{2.15}$$

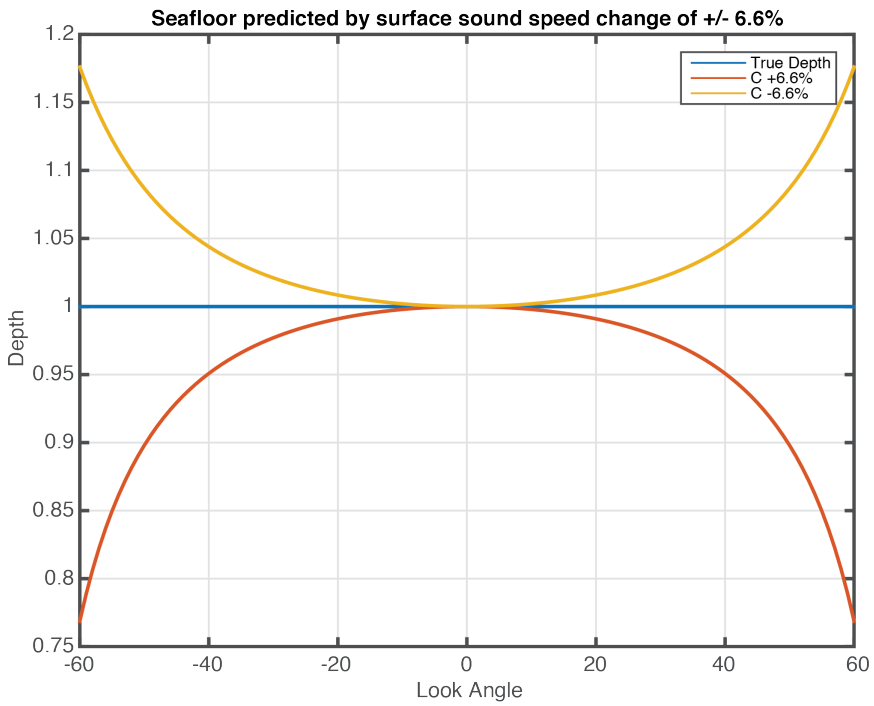

Figure 2.16: **Normalized depth change from a change in surface sound velocity.**

The change in water depth due only to the change in slant range in shown in Figure 2.17. Curiously, changing the range shifts the depth values up or down by a constant, due to the range and depth increasing linearly with sound speed.

After computing C_{avg}, the true look angle of a depth sounding may be estimated once again using Snell's Law:

$$\frac{\sin\theta_{true}}{C_{avg}} = \frac{\sin\theta'}{C'} \tag{2.16}$$

In this case, the new depth profile would be calculated by replacing C_d with C_{avg} and θ with θ_{true} in our initial expression for $H(\theta)$. Figure 2.18 synthesizes both the distortions to the look angle and range due to changing the average sound speed.

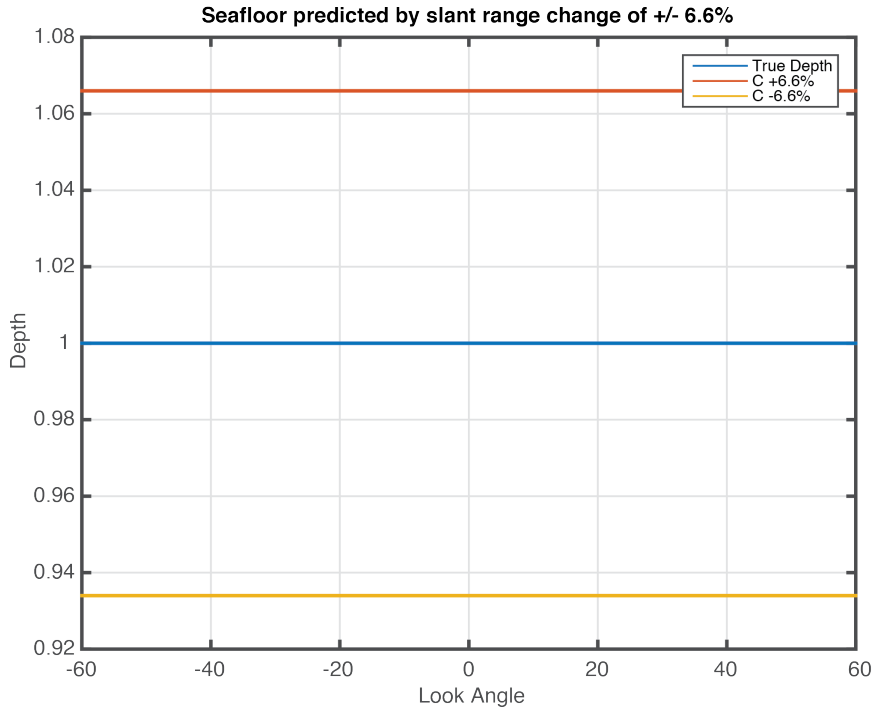

Figure 2.17: **Normalized change in water depth due to a range change of** $\pm 6.6\%$**.**

One final note is that de Moustier [1988] recommends using the harmonic mean:

$$C_h = \left[\frac{1}{H_0} \int_0^{H_0} \frac{dz}{C(z)} \right]^{-1}. \tag{2.17}$$

This yields preferable results to the standard mean because the travel time is linear with respect to slowness but not velocity.

Of course, this processing technique relies on the user obtaining an accurate sound speed profile. This may be done by deploying an XBT or CTD. However, maintaining an accurate sound speed profile during a cruise can prove difficult because of shallow depth internal waves that may alter the sound speed over timescales of tens of minutes to hours. We will discuss how to address these sound speed errors in a later section.

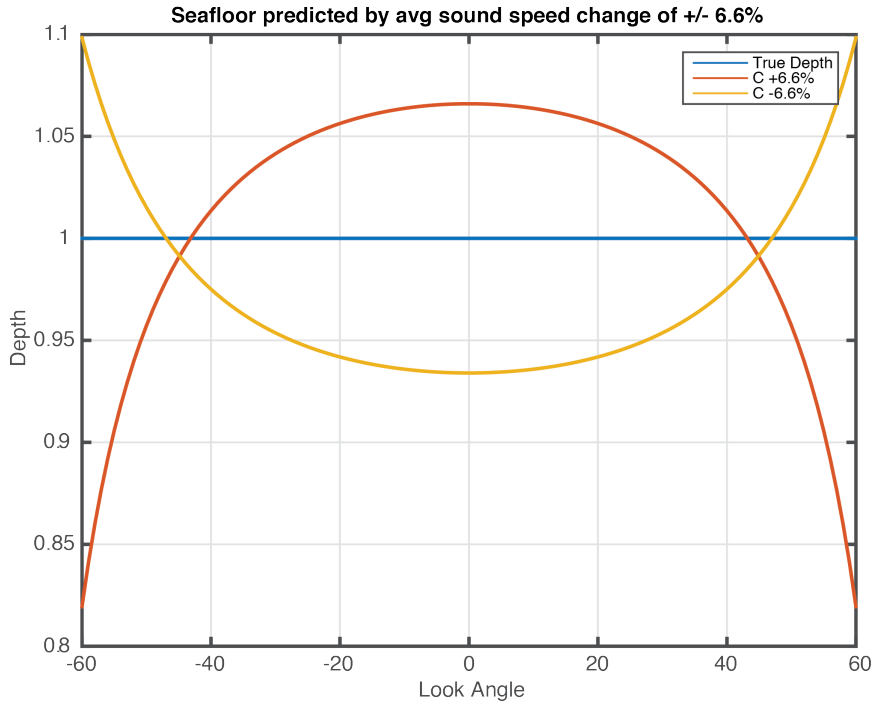

Figure 2.18: **Change in normalized water depth due to a $\pm 6.6\%$ change in average sound speed.**

2.9 Sidescan Sonar

Thus far we have considered depth measurements collected by the multibeam sonar, but the instrument is also capable of collecting information based upon the amplitude of the returned pulse. This information is referred to as backscatter or sidescan sonar, the latter name arising from sonars employed before the advent of multibeam systems. As before, the physics behind sidescan sonar are very similar to those behind satellite radar, so the following notes are partially adapted from the Rees [2001] treatment of electromagnetic radiation, as well as the SeaBeam Theory of Operation [2000] notes.

Start by considering a flat, uniform seafloor. A transmitter at the sea surface emits a pulse and measures the echoes from the seafloor, as was the case for multibeam. However, this time we are interested in the entire time series of amplitude vs time for the returning pulse. For a featureless seafloor, we expect the peak amplitude of the returned

pulse to occur at the first return; subsequent amplitudes will steadily decrease as governed by attenuation in the water column since they have travelled slightly longer distances. When the seafloor is non-uniform, the amplitude of the sonar echoes will deviate from uniform seafloor case depending on whether or not the energy is being reflected by a smoother or rougher patch of seafloor. Thus, we may use these echoes to characterize the roughness of the area ensonified by the ping.

There are a few shortcomings in our analysis thus far. First, we need some way of determining whether the echoes are returning from the port or starboard side of the ping. This is accomplished by considering the different pulse frequencies utilized to ensonify to different beam sectors (Figure 2.13, Table 2.2) to create two time series, one each for the echo amplitudes reflecting from the port and starboard sides of the vessel. (Incidentally, this is also how the name "sidescan" came into usage.)

We also need some way of locating the echoes in space, which we do by estimating the slant range to each point. A simple way to do this is by converting from the time difference between the outgoing and returning pulses, ie $\rho = \frac{Ct}{2}$ where ρ is the slant range, C is the speed of sound, and t is time. With an estimate of slant range, we may locate the points in space depending on the shape of the seafloor. For the case of a relatively flat seafloor, the minimum range ρ_0 occurs at vertical incidence and each range value corresponds to a unique look angle $\theta = \mathrm{Cos}^{-1}(\rho_0/\rho)$.

A slight complication arises when working with real data in that the sonar actually only records one look angle but many sidescan echoes per beam. As a result we must perform an interpolation to properly infer the look angle for every range echo. The rate at which the look angle changes between sidescan points depends on the slope of the seafloor. Thus, a simple method of interpolating is a linear interpolation between center beam points according to $\partial\theta/\partial\rho$.

2.10 Range Resolution

The sonar emits a short pulse that reflects off the seafloor and returns to the hydrophone array. The amplitude vs time of the return pulse is a recording of the reflectivity of the seafloor. If adjacent reflectors appear as two distinct peaks in the return waveform then they are resolved in range. The nominal slant range resolution is $\Delta\rho = C\tau/2$ where τ is the pulse length, and C is the speed of sound in seawater. The factor of 2 accounts for the two-way travel time of the pulse.

The ground range resolution (Figure 2.19) is geometrically related to the slant range resolution by the relation

$$R_r = \frac{\Delta\rho}{\sin\theta} = \frac{C\tau}{2\sin\theta}. \tag{2.18}$$

Note the ground range resolution is infinite for vertical look angle and improves as look angle is increased. Also note that the range resolution is independent of the depth of the seafloor H. The range resolution can be improved by increasing the bandwidth of the sonar. The Kongsberg EM122 multibeam employs pulse lengths of 2 ms for shallow water depths, 5 ms for intermediate water depths, and 15 ms for deep water depths. Slant and ground range resolutions for these pulse lengths are shown in Table 2.3.

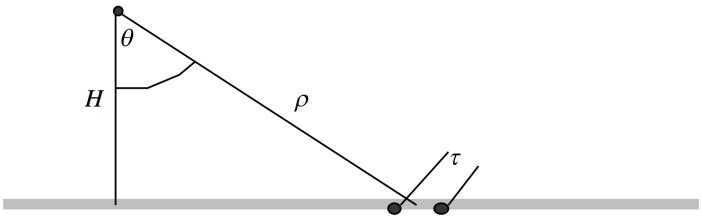

Figure 2.19: **Schematic diagram of the relation between slant range and its projection on the seafloor, called the ground range. (Taken from [Sandwell et al. 2016].)**

Table 2.3: **Range resolution of the Kongsberg EM122.**

Depth	τ (ms)	Slant Range (m)	Ground Range (m)		
			$\theta = 20°$	$\theta = 40°$	$\theta = 60°$
Shallow	2	1.5	4.39	2.33	1.73
Intermed.	5	3.75	10.96	5.83	4.33
Deep	15	11.25	32.89	17.50	12.99

2.11 Real Sound Velocity Profile Examples

In previous sections we have considered the normalized depth errors due to a change in surface sound speed or average sound speed across the entire water column, but we have not obtained a reasonable estimate for the magnitude of depth errors given realistic sound velocity profiles. In this section we shall estimate depth and range errors by analyzing sound velocity profiles collected during two cruises: the RR1605 cruise south of Palau and the RR1719 cruise west of Oregon, USA. These cruises were both conducted on the R/V Roger Revelle in regions with seafloor deeper than 4000 meters using the same multibeam sonar, a Kongsberg EM122. However, the sea surface temperature varies according to region and time of year. For instance, the surface sound velocity is approximately 30°C in the RR1605 survey area and approximately 18°C in the RR1719 survey area. We compare these sound velocity profiles to mean water column profiles computed from annual measurements of ocean temperature and salinity [Levitus 1982; Dushaw et al. 1993].

We compute the depth profiles that would result from using sound velocity profiles from these cruises, assuming a flat seafloor of 4000 m water depth when the water column consists of a constant 1500 m/s sound velocity profile (Figure 2.20). The largest depth differences at nadir are approximately 20 m, or 0.5% of the water depth, which is significant. We also obtain an estimate of the magnitude of sound velocity variations over short time scales by observing the difference between the XBT and mean

annual sound velocity profiles (Figure 2.21), which on the order of a meter.

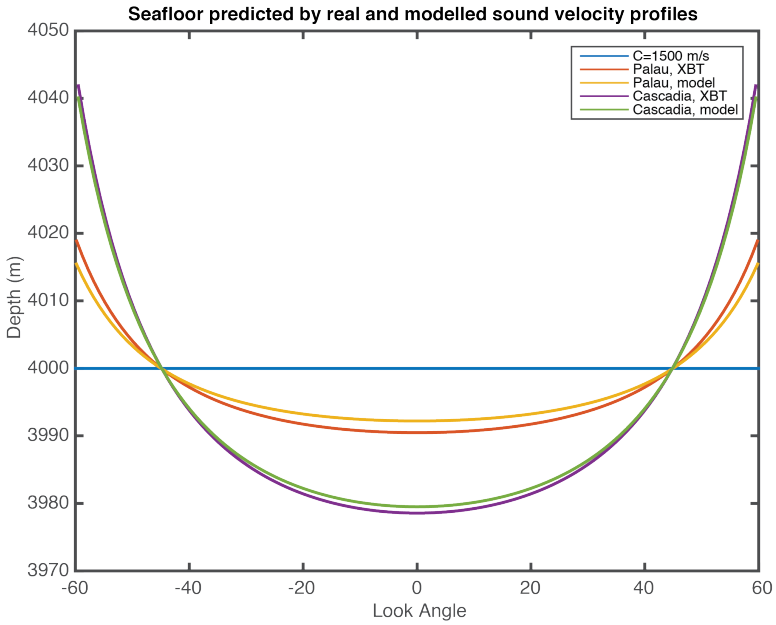

Figure 2.20: **Change in water depth (assuming flat seafloor of 4000 m depth) due to applying a real sound velocity profile rather than a constant 1500 m/s water velocity.**

We also estimate the difference in predicted range between the XBT and mean annual sound velocity profiles (Figure 2.22). Because the instantaneous sound velocity profile during a survey may vary from the annual mean due to seasonal trends or internal waves, this gives us a rough estimate of the range error in any particular survey. Perhaps surprisingly, the range error is linear with range, because the range is linear in travel time due to the average sound speed C_{avg} being essentially constant over the course of a single ping. Unfortunately, C_{avg} may change with depth, so we must stress that this linear relation only holds true for a single ping. The range error will in general not be linear with range at nadir because increasing the water depth will usually increase C_{avg} for large depths. However, this relationship should approach linearity as $\partial C_{avg}/\partial H$ approaches 0 for very deep water. Regardless, Figure 2.22 should give us a sufficient order of magnitude estimate for range error since there is a significant surface temperature

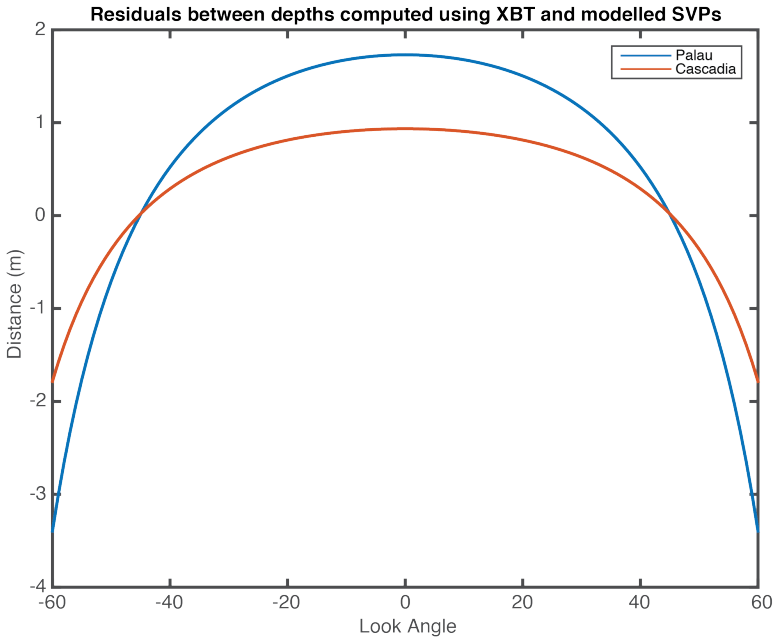

Figure 2.21: **Difference in water depth (assuming flat seafloor of 4000 m depth) due to applying a real or modelled sound velocity profile.**

difference between the two surveys plotted.

2.12 Sidescan Data Processing

There are special considerations that must be taken into account when processing sidescan data due to it having a finer resolution than multibeam bathymetry. Whereas a bathymetry data set may have one echo for depth and look angle per beam, raw sidescan data may contain from 2-3 amplitude echoes in vertical beams to 12-16 amplitude echoes in outer beams. As a result of this, some form of interpolation is required in order to properly assign range and look angle values to sidescan echoes.

The Kongsberg EM122 does not provide range and look angle information for every sidescan echo. Rather, it provides information about which pixels reside in which beams and which pixels are the center pixels of each beam. Using this information, we

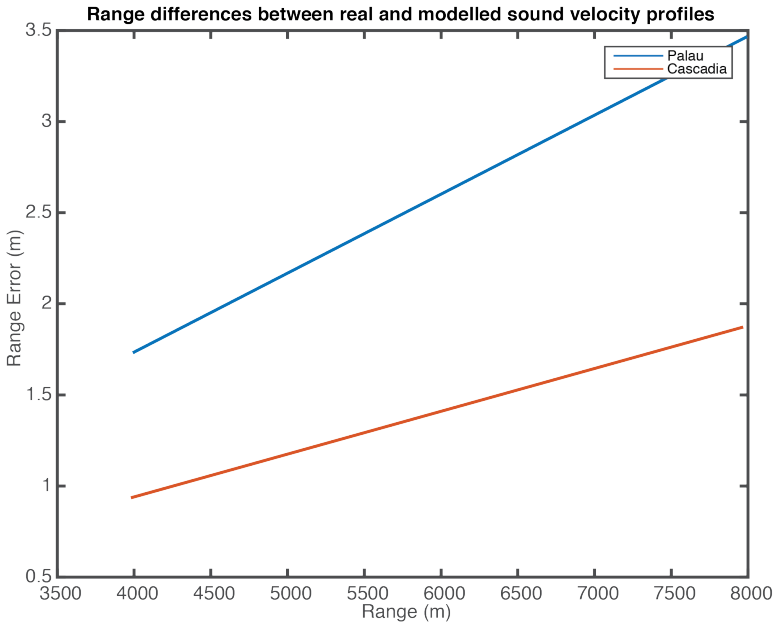

Figure 2.22: **Difference in range (assuming flat seafloor of 4000 m depth) due to applying a real or modeled sound velocity profile.**

assume the center sidescan pixels of each beam have the range and look angle values corresponding to the multibeam bathymetry and perform a linear interpolation to infer the range and look angles of off-center sidescan pixels.

2.13 Conclusions

Multibeam sonar is an instrument that measures the two-way travel time of an acoustic pulse from a research vessel to the seafloor to map the seafloor. There are a few frequencies of acoustic pulses that are used by multibeam sonars, but the primary frequencies are 12 kHz and 30 kHz. Higher frequency multibeams yield higher resolution bathymetry but attenuate faster in seawater. As a result, the 12 kHz sonar is ideal for mapping bathymetry deeper than 1000 m, and is tuned for mapping most regions of the open ocean, whereas higher frequency sonars are more appropriate for shallower waters.

The transmit and receiver arrays of the multibeam sonar have resolutions that are governed by Fraunhoffer diffraction, and have a fine resolution in one dimension each. The arrays are arranged perpendicular to one another in a Mills cross formation, allowing the transmit array a resolution of 1° in the along-track direction and the receiver array a resolution of 1° in the across-track direction. The nominal resolution of bathymetry collected by a 12 kHz multibeam sonar is 100-150 m dependent on depth, but this value may increase for very deep seafloor. In a single ping, the sonar emits up to nine pulses at different angles by introducing small time delays in the signals emitted by adjacent transducers; this process is known as beam steering. Likewise, the hydrophones may be filtered to distinguish the angle of incoming acoustic energy. However, beam steering requires independent measurements of the ship orientation to properly correct the angles used in beam steering for the roll, pitch, and yaw of the vessel.

In addition to bathymetry, multibeam sonars collect information on the amplitude of returning acoustic pulses and uses this information to measure the backscatter of the seafloor, known as sidescan. Unlike bathymetry, which has an across-track resolution dependent on the geometry of the array, sidescan has a range resolution dependent on the pulse length and look angle of a pulse. The resolution of sidescan is best for look angles from 15°-65°due to poor theoretical resolution at nadir and high noise at oblique angles due to longer ray paths.

Accurate measurements of the sound velocity profile are critical for collecting accurate bathymetry and sidescan data. Errors from the surface sound speed will cause incoming rays to appear to arrive from distorted look angles, leading to a warped bathymetry swath. Likewise, errors in sound speed along the ray path, modeled as an erroneous average sound speed, will cause a shift in the measured depth. The easiest way to ensure a reasonable sound velocity profile is to collect an XBT during data collection. We demonstrate that naively assuming a constant sound velocity of 1500 m/s can lead to

depth errors on the order of 20 m; proper measurements of sound speed such as collected by an XBT or CTD are required for collecting accurate bathymetry. Comparing XBT measurements to a mean annual model of sound velocity, we expect range errors on the order of a few meters for ranges between 4000-8000 m.

Acknowledgements

Chapter 2, in full, is an unpublished compilation of notes on multibeam theory compiled by John B. DeSanto and David T. Sandwell. The dissertation author is the primary investigator and author of this paper.

References

Ainslie, Michael A. and McColm, James G. (1998). "A simplified formula for viscous and chemical absorption in sea water". In: *The Journal of the Acoustical Society of America* 103.3, pp. 1671–1672. DOI: 10.1121/1.421258.

Becker, J. J. and Sandwell, D. T. (2007). *SRTM30 PLUS: Data fusion of SRTM land topography with measured and estimated seafloor topography (Version 3.0)*.

Bracewell, R. N. (1978). *The Fourier Transform and its Applications*. Second. McGraw-Hill Book Co.

Clarke, John E. Hughes (Jan. 10, 2017). *Multibeam Sonar Methods*. Presentation, Swath Sonar Training 2017 Workshop.

De Moustier, C (Jan. 1988). "State of the Art in Swath Bathymetry Survey Systems". In: *OED (ASME, Ocean Engineering Division)* 13.

Dushaw, Brian D., Worcester, Peter F., Cornuelle, Bruce D., and Howe, Bruce M. (1993). "On equations for the speed of sound in seawater". In: *The Journal of the Acoustical Society of America* 93.1, pp. 255–275. DOI: 10.1121/1.405660.

Farr, Harold K. (1980). "Multibeam bathymetric sonar: Sea beam and hydro chart". In: *Marine Geodesy* 4.2, pp. 77–93. DOI: 10.1080/15210608009379375.

Greene, John. *Seeing with Sound*. https://crestfest.wordpress.com/2016/01/24/seeing-with-sound/. Accessed: 2018-11-01.

Kongsberg (2011). "Kongsberg EM 122 Multibeam echo sounder Product Description". In:

Levitus, S. (1982). "Climatological Atlas of the World Ocean". In: *NOAA/ERL GFDL Professional Paper 13, Princeton, N.J., 173 pp. (NTIS PB83-184093)*.

Rees, W. G. (2001). *Physical Principles of Remote Sensing*. Cambridge, UK: Cambridge University Press.

Sandwell, David, Mellors, Rob, Tong, Xiaopeng, Xu, Xiaohua, Wei, Matt, and Wessel, Paul (June 1, 2016). *GMTSAR: An InSAR Processing System Based on Generic Mapping Tools*. https://topex.ucsd.edu/gmtsar/tar/GMTSAR_2ND_TEX.pdf.

SeaBeam (2000). *Multibeam Sonar Theory of Operation*. L-3 Communications SeaBeam Instruments. East Walpole, MA.

Chapter 3

Seafloor Geodesy from Repeated Sidescan Sonar Surveys

3.1 Introduction

3.1.1 Summary

There is a compelling need for accurate and economical tools to be used for seafloor geodetic applications [Davis et al. 2012; Wilcock et al. 2012]. The vast majority of plate margins, specifically the subduction zones associated with megathrust earthquake and tsunami hazards, are distributed in marine environments unobservable via traditional satellite-based techniques [Spiess 1985]. Understanding the earthquake cycle along spreading ridges, transform faults, and subduction zones will require at least two types of geodetic measurements - point measurements to establish plate motions and spatially dense coverage to investigate moment accumulation rate of locked patches at the plate margins.

On land, these tools are well developed. Point measurements from GPS net-

works provide mm-accuracy, vector displacement time series [Wdowinski, Sudman, and Bock 2001], and InSAR provides spatially dense snapshots of line-of-sight deformation [Bürgmann, Rosen, and Fielding 2000]. However, these techniques make use of electromagnetic radiation which cannot penetrate the deep ocean.

There are three main classes of seafloor geodetic measurements [Bürgmann and Chadwell 2014]. First, hybrid GPS-Acoustic (GPS-A) arrays measure the relative position between three or more seafloor transponders via acoustic ranging. The location of these transponders is monitored by a ship, buoy, or wave glider whose position is in turn monitored in a global reference frame using GPS. Second, pressure sensors can be deployed to the seafloor to directly measure vertical deformation. Finally, the seafloor can be imaged using a multibeam sonar array or an active source seismic array. These data have geodetic applications when comparing repeated surveys.

GPS-A was first proposed by Spiess [1985], and has since been employed to measure tectonic motions of the Juan de Fuca plate [Chadwell and Spiess 2008], interseismic strain accumulation due to subduction offshore coastal Peru [Gagnon, Chadwell, and Norabuena 2005], as well as the coseismic [Sato et al. 2011; Kido et al. 2011] and postseismic [Watanabe et al. 2014; Tomita et al. 2015] displacement due to the 2011 M_ω 9.0 Tohoku-Oki earthquake. Analogous to terrestrial GPS, these systems can capture centimeter-scale motions at specific points, but GPS-A is hampered by the considerable expense of deploying and monitoring transponders as well as the significant ship time required to make the measurement. In contrast, multibeam sonar data are significantly cheaper to acquire and provide a denser spatial coverage like InSAR, but are significantly less accurate. Repeated multibeam surveys have mostly been used to detect large changes ($>$10 m) in bathymetry due to volcanic events [Chadwick, Embley, and Fox 1991; Fox, Chadwick, and Embley 1992; Chadwick, Embley, and Shank 1998; Caress et al. 2012]. However, the Fujiwara et al. [2011] study showed that even the 10-m accuracy of the

multibeam sonar was sufficient to provide important constraints on the very large displacement ($\sim$ 50 m) of the seafloor associated with the Tohoku-Oki earthquake. These multibeam data were critical for understanding why the tsunami had such large amplitude.

We are investigating methods for improving the accuracy of the seafloor displacement measurement using digital image correlation [Pan et al. 2009], a technique used to measure horizontal offsets. Digital image correlation has been developed as a tool for measuring in-plane deformation with sub-pixel accuracy [Chen et al. 1993; Sjödahl and Benckert 1993]. These techniques are analogous to pixel tracking, which has been used in InSAR studies to measure ice velocities and along-track offsets for co-seismic motions [Joughin 2002].

The accuracy of a displacement measurement obtained from a correlation study is a sub-pixel quantity, but the horizontal resolution of standard multibeam bathymetry depends upon the height of the measurement platform above the seafloor. Thus, although Fujiwara et al. [2014] demonstrated meter accuracy displacement measurements from repeated multibeam surveys of shallow ($\sim$1000 m) water, this may not be easily extended to water deeper than 2000-3000 m, when the resolution of multibeam increases to 100-150 m. In contrast, sidescan data, while still having an along-track resolution comparable to bathymetry, have an across-track resolution R_r of

$$R_r = \frac{c\tau}{2\sin\theta} \tag{3.1}$$

where θ is the look angle, c is the speed of sound in seawater, and τ is the pulse length. (See Methods section.) Since this quantity depends upon the look angle rather than platform height, the across-track resolution of sidescan may remain on the order of the pulse length in water 4000-6000 m deep. Here we evaluate sidescan data from a 12 kHz system having a nominal range resolution of 13-64 m. Thus, we propose cross

correlating the sidescan data product of multibeam sonar systems, which should yield superior displacement measurements in at least one dimension.

There are three general sources of error that must be quantified in such an experiment: variations in the sound speed profile, uncertainty in the digital image correlation that depend on the cruise parameters of the multibeam surveys (including the ship speed and stability, the seafloor depth and roughness, and the distance between repeat tracks), and limitations of the navigational system used to locate the measurement platform. We evaluate the error associated with each source by analyzing data from two cruises, the 2003 survey CNTL15RR collected approximately 2500 m above the young, lightly sedimented seafloor on the flank of the Juan de Fuca Ridge, and the 2010 survey MV1011 collected approximately 4300 m above old, heavily sedimented seafloor 300 nautical miles offshore Southern California.

3.1.2 Sound Speed Errors

We address concerns of sound speed variations with the following thought experiment. Consider the area of seafloor ensonified by right- and left-looking pings from a multibeam sonar (Fig 3.1a). We assume the most likely source of sound speed variations is due to internal waves in the upper water column. Such waves have a period on the order of tens of minutes, far greater than the duration of a single ping. Thus, we posit that at any given moment of time the sound speed perturbation appears to be a horizontal layer, as shown in Fig 3.1b. This has the effect of introducing a time delay into the signal relative to the expected ping duration, similar to if the platform had moved vertically some distance ΔH.

Due to the even symmetry of this model, we expect the apparent horizontal motion of the port and starboard seafloor to cancel one another. This expectation is routinely

applied to address variations in sound speed velocity in high-precision GPS-Acoustic surveys [Spiess et al. 1998]. The primary difference between GPS-Acoustic studies and repeat cross-correlation studies is that apparent horizontal motions due to sound speed velocity variations are averaged out over the time domain in the former and the spatial domain in the latter.

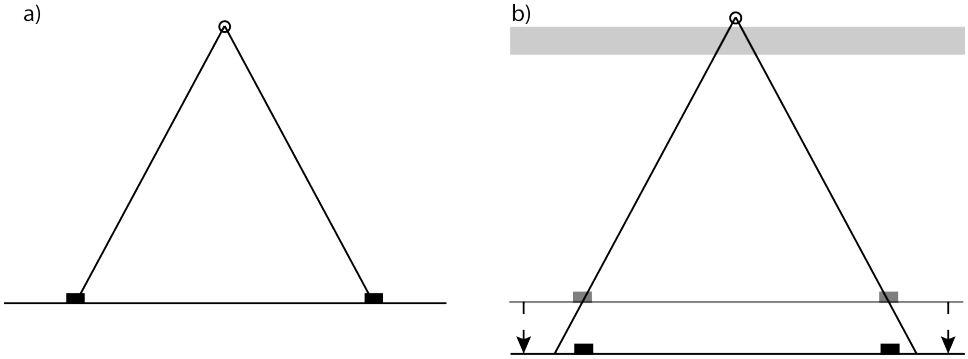

Figure 3.1: **Schematic cross-section of a single multibeam ping ensonifying an area of seafloor (a), and it's apparent change due to the injection of a horizontal layer of "slow" sound speed water near the sea surface (b).**

3.1.3 Image Correlation Errors

We assess the accuracy of the digital image correlation operation by applying it to sets of repeated sidescan sonar surveys, which have similar geometries in a single locale and consist of tracks collected in the same direction. We extract raw sidescan amplitudes from instrument-generated data files using the MB-System software package [Caress and Chayes 1996] and rotate them into a coordinate frame with axes aligned with the along-track (azimuth) and across-track (range) directions. We then create grid files of the surveys using the Generic Mapping Tools software [Smith and Wessel 1990]. We then calculate the normalized cross-correlation between the grids, estimating the offset as the location of peak correlation coefficient [Pan et al. 2009].

We analyze repeated multibeam tracks from the CNTL15RR and MV1011 cruises. These tracks are separated only by at most a few days of time; any deformation that may have occurred is thus negligible. We estimate the displacement accuracy by injecting an artificial horizontal offset in the repeat data and comparing the estimated offset with the injected offset. We repeat this process many times, analyzing the residuals between the injected and measured offsets to assess the accuracy and precision of this methodology.

In this way, we may begin to assess the relevance of various cruise parameters to this type of experiment. Of particular interest is the ship speed and stability during data collection, as well as how closely the tracks are repeated. These parameters should directly affect the distribution of soundings on the seafloor, as well as the coherence between repeat surveys. Also of interest are the seafloor characteristics; rougher seafloor should presumably lead to a higher correlation.

3.1.4 Navigation Errors

The multibeam sonar precisely measures the range to seafloor reflectors; such a relative measurement is only as accurate as our knowledge of the location of the instrument platform. Multibeam sonars generally rely on information from the ship navigation and motion reference unit to locate points on the seafloor. We evaluate the precision of the ship navigation by comparing it to independent location measurements collected during the CNTL15RR cruise, and apply the improved navigation to the associated sidescan data to assess its affect on the image correlation experiment.

3.2 Image Correlation Tests

3.2.1 CNTL15RR Cruise

A 2 day survey designed to assess the feasibility of creating synthetic aperture sonar (SAS) images from multibeam sonar data collected in regions with deep ($\sim$3000 m) seafloor (Fig 3.2) was conducted in 2003 as part of the CNTL15RR cruise aboard the R/V Roger Revelle. The survey consisted of 6 tracks, denoted EXP01 through EXP06, in two sites, across the Juan de Fuca Ridge axis and off the ridge flank. Data were collected at slow ship speeds using a Kongsberg EM120 multibeam system.

Of the 6 multibeam tracks collected, EXP01 and EXP03 were collected above the Juan de Fuca Ridge axis with the intent of forming a synthetic aperture above young, rough seafloor. These data were collected at a speed of 0.5-1.5 knots and a heading of 277 degrees and are a close repeat with a baseline of 1 m on average for 6 km of track length. We calculate an estimate of the signal and noise between these tracks by computing their sum and difference. The sum (Fig 3.3) shows a coherent mottled texture, and the difference shows a speckled pattern with little structure and relative amplitude about 25-50% of the coherent signal. The experiments had minor difficulties maintaining a constant heading due to persistent winds and currents from the north, but most correlation errors are likely due to the EM120 yaw stabilization being set to filtered heading during EXP01. As a result, the orientation of the pings in EXP01 was dependent upon the orientation of the ship at the time of transmission rather than upon a user-specified orientation. The yaw compensation of EXP03 was set to 273 degrees to most closely match the heading of EXP01 while accounting for systematic biases between the ship gyro system and the PHINS INU.

The EXP02 and EXP04 through EXP06 tracks were collected on the cleft flank of the Juan de Fuca Ridge near (44°42.75' N, -130°02.59' E). These surveys were designed

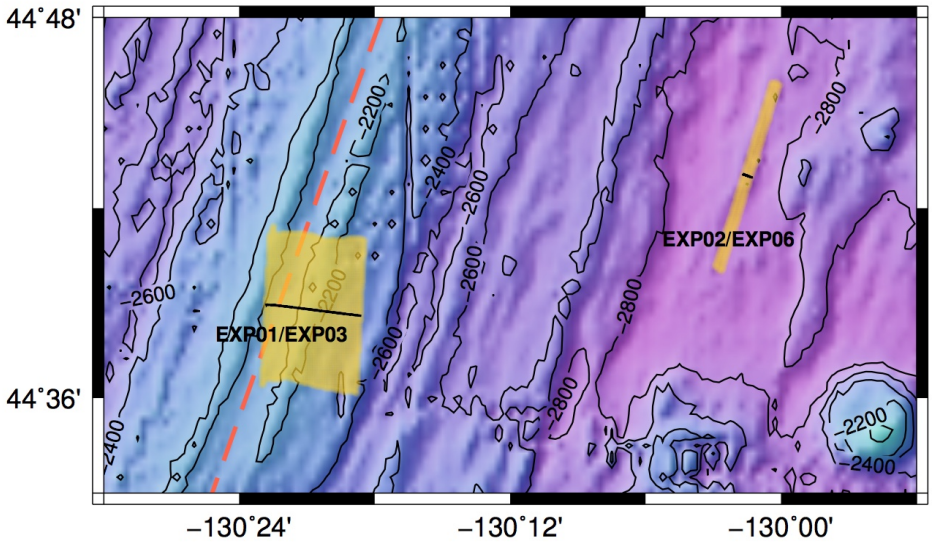

Figure 3.2: **Regional topography of the CNTL15RR cruise in meters. The red dashed line marks the location of the Juan de Fuca Ridge. Locations of repeated tracks are displayed in black, with ensonified areas in yellow.**

to compliment the ridge axis surveys by forming a synthetic aperture above relatively older, more sedimented seafloor. The EXP02 track was collected at a speed of 0.5-0.6 knots and a heading of 290 degrees controlled by the manual yaw stabilization. The remaining tracks were collected with the intent of repeating the EXP02 track, but were met by various difficulties. Inclement weather during EXP04 and EXP05 rendered the ship unable to maintain a steady track at such a slow ship speed; to compensate the ship speed was increased to 1.2-1.5 knots. To ensure the pulse frequency of the sonar remained below the pulse repetition frequency theoretically required for successfully forming a synthetic aperture the beam width was narrowed such that the maximum allowed range was 3800 meters. As a result, EXP04 and EXP05 have drastically reduced coverage, and the coverage preserved is exclusively of the near-vertical beams unsuitable for digital image correlation due to their poor range resolution. The EXP06 track is a high-quality repeat of EXP02 since it was collected with the same heading and ship speed with a small baseline offset averaging 3 m, but is only 1 km long due to time constraints during the

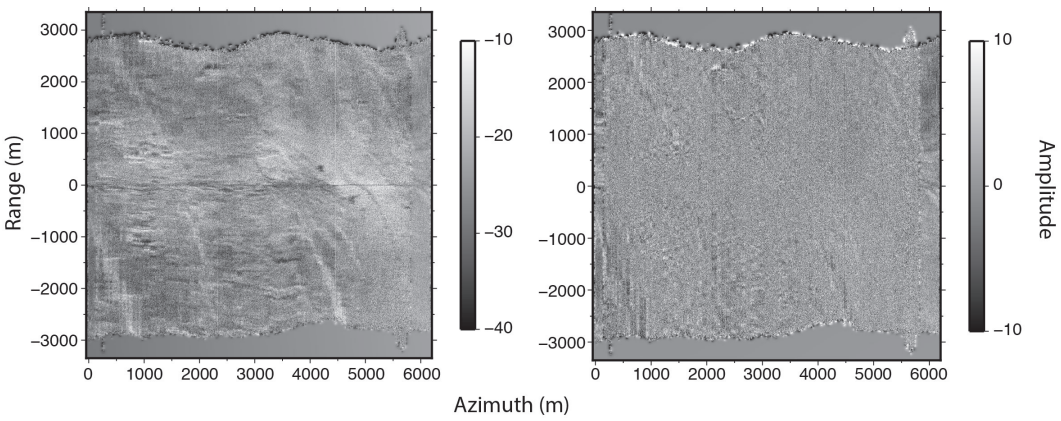

Figure 3.3: **Sum (left) and difference (right) of the EXP01 and EXP03 sidescan tracks. The data have been rotated into a coordinate frame of range and azimuth, both in m.**

survey. The horizontal lineations across the sidescan data (Fig 3.4) are sharp in the range direction, which aids in the cross-correlation. In addition the noise between surveys is small relative to the noise between EXP01 and EXP03.

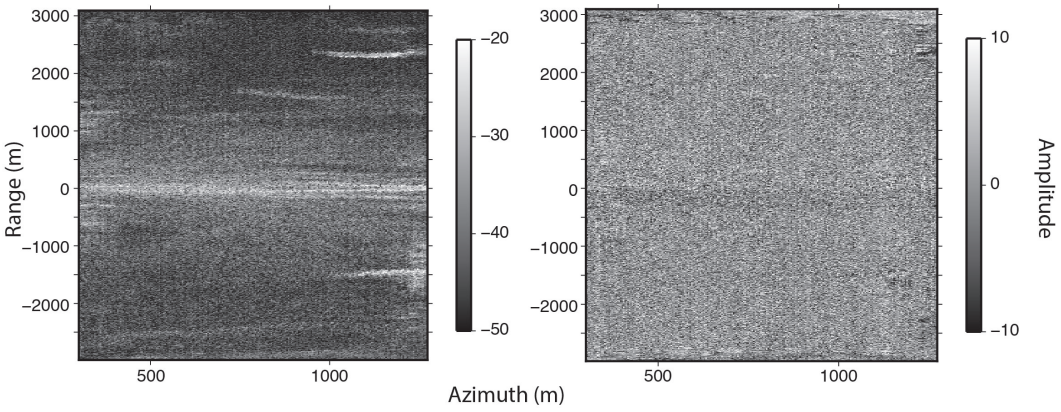

Figure 3.4: **Sum (left) and difference (right) of the EXP02 and EXP06 sidescan tracks. The data have been rotated into a coordinate frame of range and azimuth, both in m.**

3.2.2 MV1011 Cruise

The MV1011 cruise was conducted in 2010 offshore of Southern California in the vicinity of 124°W, 32.25°N using the Kongsberg EM122 multibeam array aboard the R/V Melville (Fig 3.5). The seafloor in this region is approximately 4300 m deep, being old and far from any spreading ridges. Presumably from its age, it is also heavily sedimented, although it displays a well-defined abyssal hill fabric oriented North-South. This is advantageous since the fabric manifests perpendicular to the range direction in the sidescan plots (Figs 3.6 and 3.7). The survey was collected at speed of 3.2-3.5 knots, and includes 5 sections of track that repeat in two regions offset by approximately 2 km. The tracks that repeat one another are approximately 20 km long and separated by 2 m on average in the across-track direction. Denoting the successive repeated tracks MV11A through MV11E, MV11B and MV11D repeat in the eastern section and the remainder in the western region. All of the tracks maintain a stable heading, although this heading is not necessarily in the direction of the track. Nevertheless, the stability of the heading means that we may easily correct for any resulting yaw biases. These tracks have a range sampling on the order of a meter, but an azimuth sampling between 30 and 40 meters due to the faster ship speed compared to the CNTL15RR survey.

Although the ensonified areas of the western and eastern tracks show significant overlap, we do not perform correlation between the two sets for two reasons. First, the track headings are out of phase by approximately 180°, which may introduce unwanted errors due to the relative difference in the phase center of the multibeam array. Second, the 2 km offset between regions would likely reduce correlation significantly due to reflectors on the seafloor being observed by significantly different look angles. The error contributions of both of these effects will need to be quantified in the future, but the MV1011 survey is not ideal for such a study since the contributions cannot be isolated.

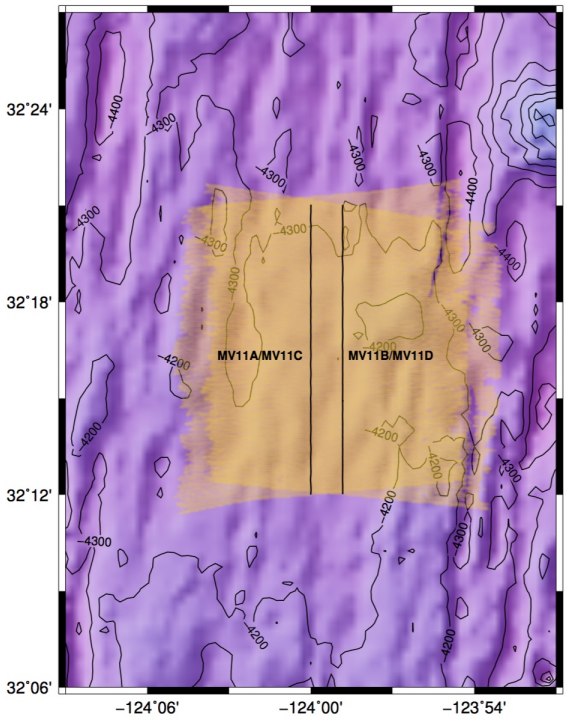

Figure 3.5: **Regional topography of the MV1011 cruise in meters. Locations of repeated tracks are displayed in black, with ensonified regions in yellow.**

3.2.3 Results

We perform cross-correlation of repeated raw sidescan tracks in the CNTL15RR and MV1011 surveys, injecting offsets in both the azimuth and range directions ranging from -10 $< x <$10 m with 1 m increments. After estimating the displacement, we difference the measured and injected offsets to obtain a set of residuals with which to assess the efficacy of this method (Fig 3.8 and Table 3.1). For the cross correlation, the CNTL15RR tracks were gridded at a resolution of 20 m in both the azimuth and range directions. The MV1011 tracks were gridded at 120 m in the azimuth direction, owing to the scarcer ping spacing, and 20 m in the range direction. The residuals are precise to the scale of decimeters to meters, but show systematic biases on the order of meters to tens of meters.

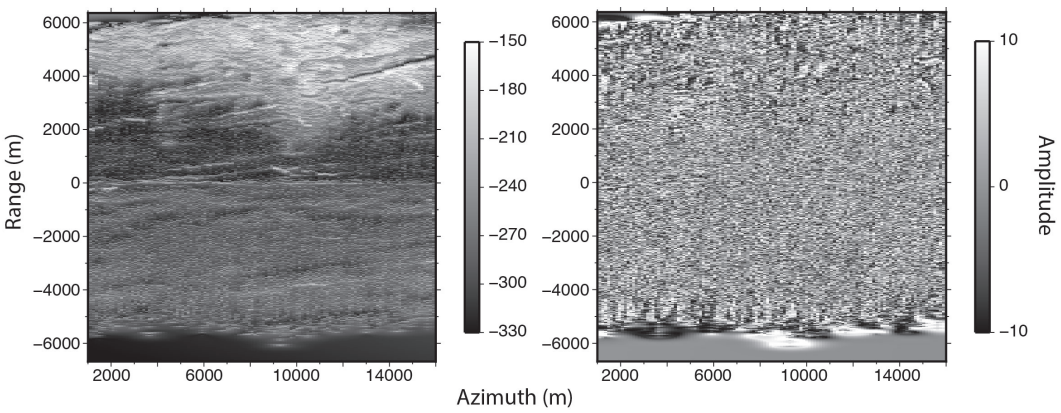

Figure 3.6: **Sum (left) and difference (right) of the MV11A and MV11C sidescan tracks. The data have been rotated into a coordinate frame of range and azimuth, both in m.**

Table 3.1: **Statistics of the residuals obtained by differencing the measured and predicted offsets obtained by performing cross correlation on the whole data sets. CNTL15RR tracks EXP01-EXP06 were gridded at 20 m in both the azimuth and range directions. MV1011 tracks MV1011A-MV1011D were gridded at 120 m in the azimuth direction and 20 m in the range direction.**

Experiments	Max Correlation	Azimuth Residual Mean (m)	Range Residual Mean (m)
EXP01/EXP03	0.58	2.55 ± 1.93	0.07 ± 0.75
EXP02/EXP06	0.80	1.01 ± 1.67	-3.14 ± 0.76
MV1011A/MV1011C	0.90	43.92 ± 3.21	-5.54 ± 0.57
MV1011B/MV1011D	0.90	-36.79 ± 0.73	3.09 ± 0.25

3.3 Navigation Tests

3.3.1 Navigation Data

The location of the vessel is measured using the shipboard navigation, which depends upon a single-frequency GPS receiver processed using the P-code protocol (PC). During the CNTL15RR cruise, three additional dual-frequency GPS receivers were deployed aboard the vessel to serve as a complimentary location feed. From these dual-frequency GPS locations, we infer the orientation of the ship independent of the

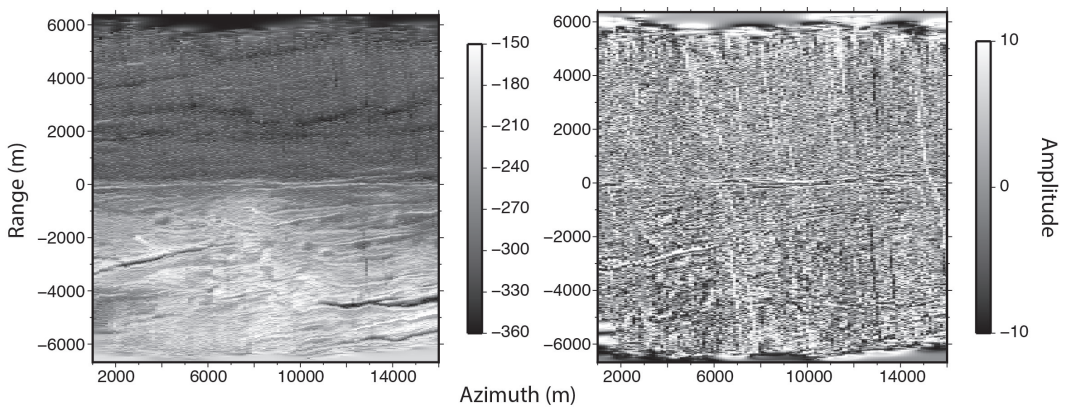

Figure 3.7: **Sum (left) and difference (right) of the MV11B and MV11D sidescan tracks. The data have been rotated into a coordinate frame of range and azimuth, both in m.**

onboard motion reference unit and define a body frame through which we may accurately track the location of any specific point during the experiment. In particular, we are interested in the location of the center of gravity of the vessel (CG) and the location of the transmitter array (TX). For the following analysis, we shall be analyzing the location of the vessel during a two-hour window of the EXP03 repeat survey.

3.3.2 Location Differences

The locations of TX (based on dual-frequency GPS) and PC (based on single-frequency GPS) during the EXP03 survey are plotted in Fig 3.9. We take the difference between these time series and CG to analyze changes in relative position within the body frame of the ship. TX and PC have standard deviations of approximately 15 cm and 2 m, respectively (Table 3.2). However, the single frequency ship navigation appears to drift with respect to the body frame defined by the dual-frequency receivers on the order of 1 m/hr, as demonstrated by the apparent shift in the location of PC (Fig 3.10). The actual precision of PC is over-estimated by the standard deviation due to this drift, and is likely closer to $\sim$ 50 cm.

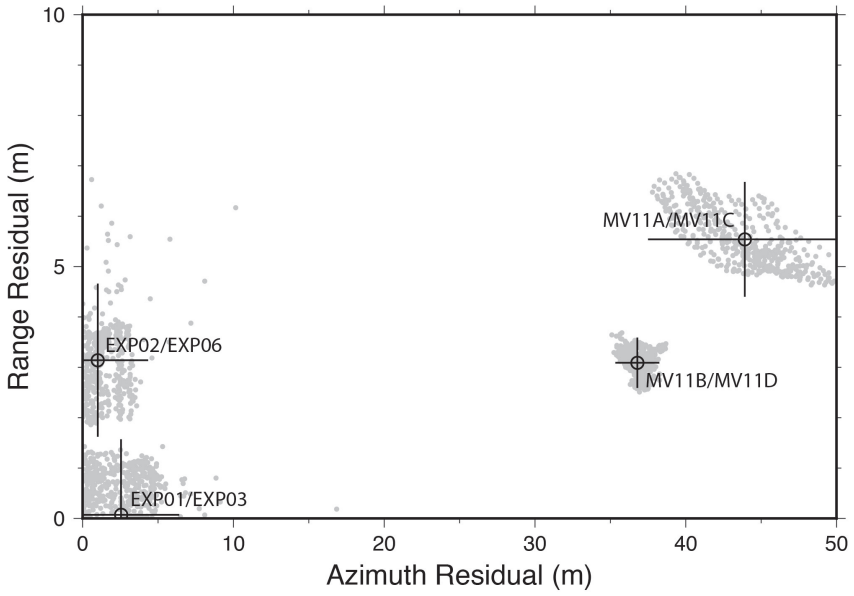

Figure 3.8: **Absolute values of residuals obtained from correlation experiments comparing injected and measured displacements. Mean error and 2σ values are plotted for each experiment.**

Table 3.2: **Position differences and absolute distances between reference points as measured by dual-frequency GPS units.**

Points	E-W Position (m)	N-S Position (m)
TX - CG	14.133 ± 0.067	-0.692 ± 0.132
PC - CG	14.783 ± 1.719	-1.341 ± 0.945

We repeat the digital image correlation procedure for EXP01 and EXP03 using the locations of CG as measured by the dual-frequency GPS units (Table 3.3). The residuals of the reprocessed results show a smaller mean and larger standard deviation in both the azimuth and range direction.

3.4 Discussion

We derive our estimate of the accuracy and precision of the displacement measurement between two surveys as the mean and standard deviation of the residuals (Table

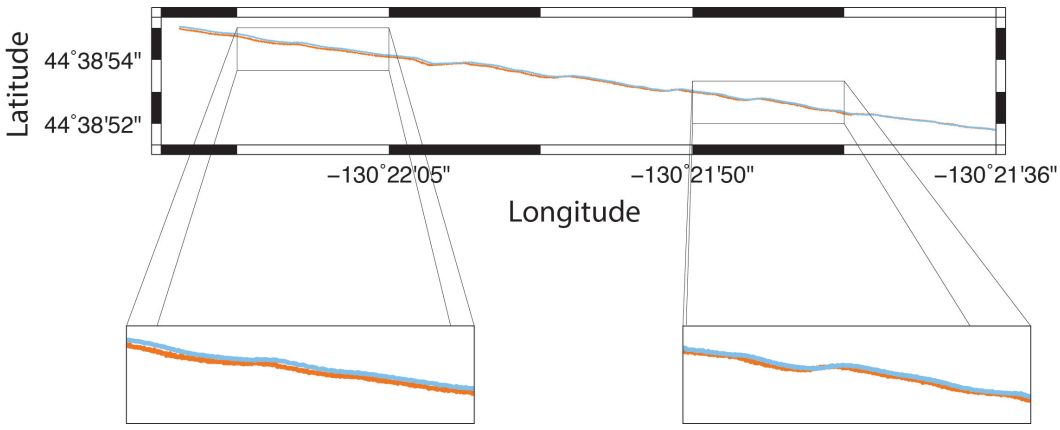

Figure 3.9: **EXP03 track as recorded by TX (blue) and PC (orange). Boxed sections are zoomed into to demonstrate instrument drift.**

Table 3.3: **Statistics of the residuals obtained by digital image correlation for EXP01/EXP03, varying navigation data used for processing. Tracks were gridded at 20 m.**

Navigation	Max Correlation	Azimuth Residual Mean (m)	Range Residual Mean (m)
PC	0.58	2.55 ± 1.93	0.07 ± 0.75
CG	0.55	0.48 ± 4.52	0.01 ± 1.66

3.1, Fig 3.8). The first-order estimate of the accuracy of this method comes from the mean of the residuals since any biases in the data will cause the mean to deviate from zero. We observe biases on the order of meters that increase by an order of magnitude in the along-track (azimuth) dimension at faster ship speeds. The large (>30 m) azimuthal biases of the MV1011 residuals may result from the lower ping density arising from these faster surveys. There is likely a shift in the ping locations along track between the two surveys, resulting in the surveys ensonifying slightly different portions of the seafloor within the same area. Increases in range bias due to ship speed are not directly observed, since the echo density depends upon the sampling rate in the range direction rather than the ship speed. However, we predict faster ship speed could cause decorrelation between tracks if the ping shift is greater than half the wavelength of the measured features; this

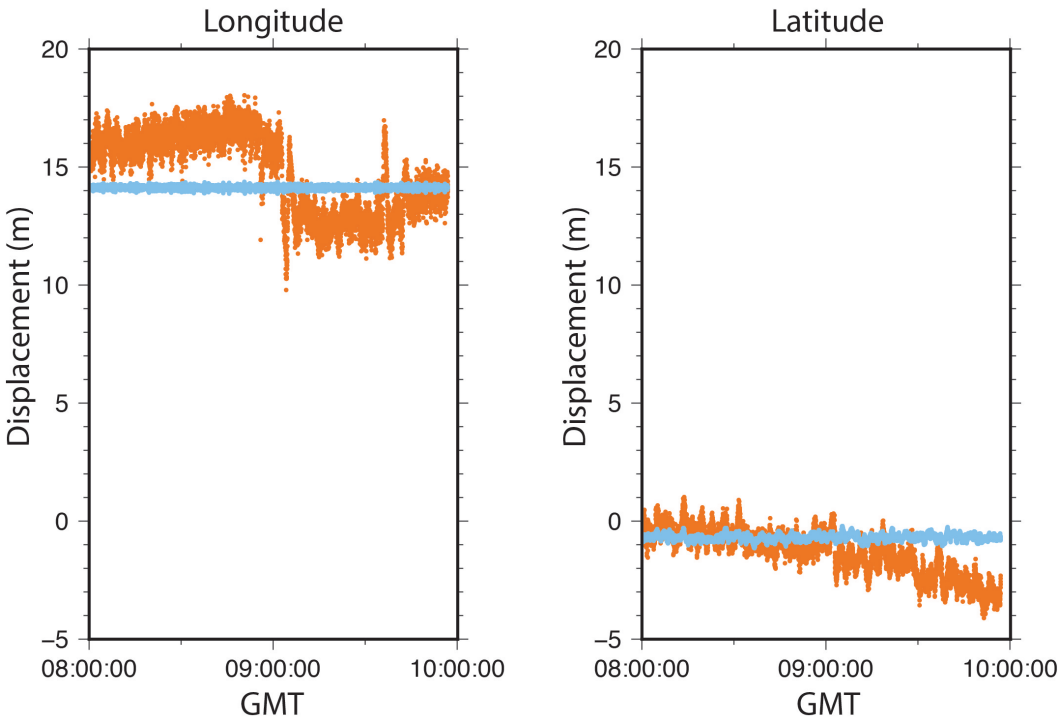

Figure 3.10: **Locations of TX (blue) and PC (orange) relative to CG. Longitude and latitude differences are converted to meters for ease of comparison with other error sources.**

would adversely affect both the azimuth and range accuracy.

Observed biases may be partially due to variations in the sound speed profile between surveys. Such variations have been previously observed [Spiess et al. 1998], but on the order of decimeters. In addition, we expect the apparent displacements from sound speed variations to mostly cancel due to symmetry. These errors are likely due to shortcomings of the ship navigation since updating the navigation with locations constrained using a trio of dual-frequency GPS receivers significantly reduced the biases observed in the EXP01/EXP03 tracks (Table 3.3). This is consistent with a drift we observed in the single-frequency ship navigation, which is on the order of meters per hour. This drift is likely due to changing electron content in the ionosphere, and probably contributes to a significant portion of the error observed in the correlation experiment. Although errors

introduced by these effects may not be crippling for most marine applications, they are large enough that a single-frequency GPS is insufficient for geodetic applications at sea.

The precision of these measurements may be estimated from the standard deviation of the residuals, and lies within the range of 0.5-2 m in the range dimension and 1-10 m for the azimuthal direction (Fig 3.8 and Table 3.1). This difference in precision is expected due to the inherently higher resolution of sidescan sonar in the range direction, especially at faster ship speeds. We interpret the improved range precision of the MV1011 tracks as due to the lineations parallel to the range dimension, which provide a distinct signal in the correlation. Geodetic measurements at this precision should be sufficient to measure displacement due to offshore earthquakes, but only once the biases due to ship speed and navigation constraints have been minimized. Even with minimal bias, signals such as plate motions would require long periods of time between measurements. Since measurements are more accurate in the range dimension, we recommend conducting at least two orthogonal surveys in an area of interest, one for each horizontal dimension.

The seafloor roughness does not seem to play a large role in the displacement precision since tracks over smooth seafloor such as EXP02/EXP06 produce displacement measurements roughly as precise as tracks over rougher seafloor. This phenomenon has been previously observed by Schreier et al. [2000], who posited that the long wavelength features contribute the largest component of the correlation. We verify this explicitly by computing the coherency spectrum for each pair of repeated tracks in the across-track (range) dimension (Fig 3.11). In each case the coherency is highest at low wavenumber (long wavelength) and falls to a noise floor at higher wavenumbers (short wavelengths). We attribute more gradual decline of the MV1011 spectra to a more even frequency distribution arising from the lineations parallel to the range dimension. The approximate wavelength at which 3 of the 4 coherency spectra fall below 0.2 is 100 meters, or 5 pixels since all of the grids considered in this study have a range cell size of 20 m. This

may seem unintuitive since the high contrast from the high-frequency signal of a rough seafloor should presumably create a higher correlation, but in practice these features are also more susceptible to random noise.

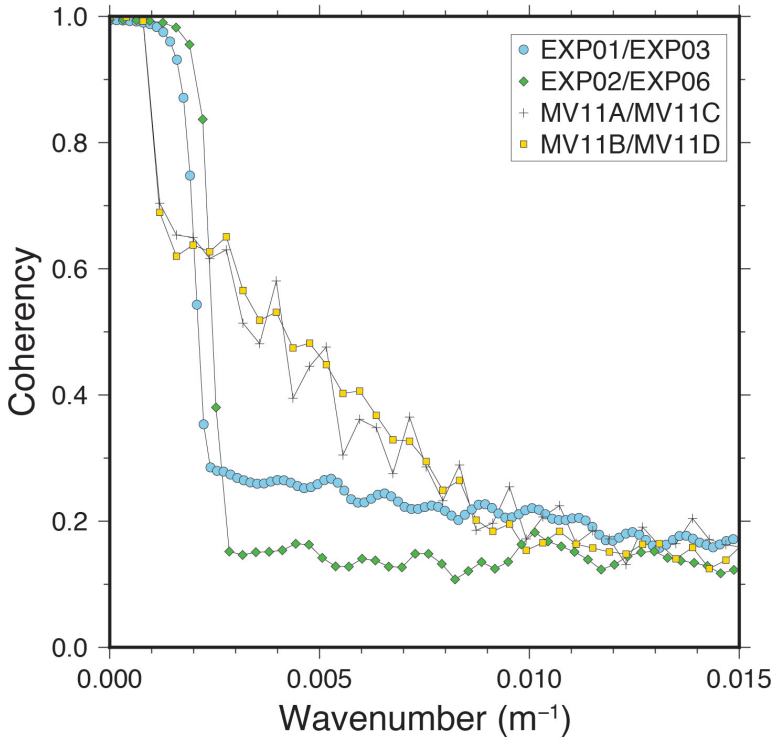

Figure 3.11: **Coherency spectra in the across-track (range) dimension, computed for each pair of repeated tracks.**

These measurements are limited by the quality of the seafloor model used to define the range parameter. For these studies a flat seafloor model has been sufficient, but in areas with sufficient relief it may be necessary to define a more rigorous range coordinate. In addition, these measurements must still be converted to a geographic coordinate frame; they are thus limited by the quality of the digital elevation model used in the conversion. Note however that multibeam is somewhat unique in that the bathymetry data product may serve this role. There is also some ambiguity in how the measurements from this study would map into the geographic coordinate frame since

they are derived from data on both the port and starboard of the vessel. However, this ambiguity could be resolved by correlating smaller data subsets, which would also allow us to more easily discard lower quality data such as those near veritcal incidence. We have yet to implement a code to perform this either of these operations.

Unfortunately, the cross-correlation is dependent upon the gridding parameters used to process the data. The grid cell size should be large enough to include multiple samples, which are then averaged to reduce noise. However, cells that are too large are less sensitive to the displacements we wish to measure. The cell size in the range dimension is primarily governed by the sampling rate of the instrument, while the azimuthal cell size is governed by the ping spacing, a function of the ship speed. While we expect the slower surveys to have better accuracy in the azimuthal direction due to denser pings, we do not observe this effect. This is likely due to the unstable heading of the ship at such slow speeds, which causes the pings to have variable density. It is thus just as important that a multibeam survey have a steady orientation as a slow speed for geodetic application.

3.5 Conclusions

We measure simulated seafloor displacement using repeated sidescan sonar surveys. From a platform height of 3-4 km and a ship speed of 0.5-3.5 knots, we are able to measure displacements accurate to tens of meters in the along-track (azimuth) direction and meters in the across-track (range) direction, an improvement over the previous Fujiwara et al. [2011] study of approximately one order of magnitude. These measurements are limited by the accuracy of the shipboard navigational system, which may be accurate to $\sim$10 cm if it utilizes a dual-frequency GPS. Single-frequency GPS units drift on the order of meters per hour and are thus not sufficiently accurate to be applied for geodetic

purposes.

The greater accuracy and precision of these measurements in the range dimension has direct implications for the orientation of the optimal survey layout. It is easier to measure the expected deformation in the across-track direction or some component thereof. Taking the example of surveying a subduction zone, we recommend collecting at least two tracks of data, which are oriented either parallel or at angles to the trench, rather than one track across the trench.

For this experimental setup to work, the survey must be collected at a stable heading and relatively slow speed. In addition, it is important to keep a careful record of the original survey so that it may be closely repeated at a later time. However, since this experimental setup makes exclusive use of equipment already available on most research vessels (except dual-frequency GPS), it presents an economical alternative to more traditional seafloor geodetic methods and may be implemented in conjunction with a wide variety of other seagoing research.

3.6 Appendix: Methods

3.6.1 Overview

We solve for the displacement between two multibeam surveys by computing the correlation between them. This method has been previously applied to measure vertical bathymetry changes due to submarine volcanic eruptions [Fox, Chadwick, and Embley 1992; Chadwick, Embley, and Fox 1991; Chadwick, Embley, and Shank 1998; Caress et al. 2012]. In addition, analogous correlation techniques have been used to measure horizontal displacements [Fox, Chadwick, and Embley 1992; Fujiwara et al. 2011]. However, all of these previous studies have only considered the bathymetry product from

the multibeam sonar; our innovation is applying these techniques to the sidescan data produced alongside the bathymetry.

3.6.2 Sidescan vs Multibeam Resolution

What makes sidescan attractive for use in these types of correlation studies is its resolution. The azimuth and range resolution (roughly corresponding to the along-track and acrosstrack resolution) of multibeam bathymetry are governed by Fraunhoffer diffusion, which simplifies to

$$R_f = \frac{\rho\lambda}{L} \tag{3.2}$$

where R_f is the resolution, ρ is the slant range, λ is the pulse wavelength, and L is the aperture length. This is sub-optimal because the parameter ρ is dependent upon the depth of the seafloor.

In the case of sidescan, only the azimuth resolution is governed by Fraunhoffer diffusion; the range resolution is

$$R_r = \frac{c\tau}{2\sin\theta} \tag{3.3}$$

where θ is the look angle, c is the speed of sound in seawater, and τ is the pulse length.

For reference, a Kongsberg EM120 multibeam sonar, which has a pulse length of 15 ms and an aperture length of 7 m, may have a bathymetry resolution of 100-150 m in both the along-track and across-track directions for seafloor of approximately 3000 meter depth. The range resolution of the corresponding sidescan would be an undefined quantity at vertical incidence, but improve to about 65 m for a look angle of 10°and 13 m at 60°. As a result, sidescan data offers superior resolution in at least one dimension.

3.6.3 Constructing Coordinate Axes

The EM120 has 9 cross-track sectors that are constrained by both the direction and carrier frequency of the outgoing pulse. The raw sidescan amplitudes do not have specific range values given by the instrument. Rather, there is information about the sector each pixel falls into and the range of each sector's center pixel. We wish to construct a simple range model, but the given center pixel associated with the minimum range may not correspond to the actual pixel with minimum range because there can be many pixels with irregular spacing in a given sector. We solve for the center pixel explicitly by fitting a linear trend to the sets of center pixel ranges of the port and starboard beams. The center pixel corresponds to the minimum where these two trends intersect. From the location of the center pixel, we may define a coordinate frame of relative ranges by incrementing the range of any adjacent pixels by a factor of $c/2\nu$, where c is assumed to be 1500 m/s, and ν is the sampling rate. Although this exercise does not yield absolute ranges, we may use it to easily construct ranges for a given seafloor model, which for the purposes of this paper will correspond to a flat seafloor of depth H.

We define the along-track, or azimuth, coordinate using locations recorded by the ship navigation system every ping. To create a consistent coordinate axis, we define an ideal repeat track line by performing a least squares fit on the locations recorded in both surveys. The critical information is then contained within the displacement vector between the ships location and an arbitrary reference point along the ideal repeat track. Decomposing this displacement vector into components parallel and perpendicular to the ideal repeat track yields the azimuth coordinate we desire and a location bias, which we refer to as the sway. Of course, the magnitude of the azimuth depends strongly on the location of the reference point; we prefer to choose a point sufficiently far from the ship surveys such that the sway is much smaller in magnitude than the azimuth in an effort to minimize distortions in the coordinate.

3.6.4 Coordinate Axis Corrections

Once we have defined the range and azimuth coordinates, we must align the tracks by correcting their coordinates based upon deviations in the ship position and orientation from the heading and location presumed by the ideal repeat track. In the following section, we shall define 2 such corrections based upon the sway (horizontal across-track motion) and yaw (heading). Presumably, there are analogous corrections for the surge, heave, roll, and pitch, but we shall not be taking these into account for the following reasons. The surge correction is somewhat trivial in that it is parallel to the azimuth coordinate. Corrections to the heave are analogous to variations in tidal height as well as sound speed in the upper water column. The roll (side-side rocking of the vessel), while critical for forming the multibeam bathymetry, is unnecessary for sidescan for similar reasons as the surge; our definition of the look angle is arbitrarily dependent upon whatever model we use to describe the seafloor. The pitch (fore-aft rocking) can vary on timescales shorter than the length of a ping, and is thus an ill-posed correction.

The sway correction accounts for strictly lateral deviations of the ship location from the ideal repeat track for a given azimuth. These deviations are easily measurable while creating the azimuth coordinate frame, and will always be present since perfectly repeating ship tracks are nominally very difficult, if not impossible, to obtain.

The need for the correction then arises since the range is taken at face value to be from the ideal ship track, but in this case would mis-locate the reflectors by the ship sway Δr. The magnitude of the correction $\Delta\rho_h$ may be calculated by making a parallel ray approximation, allowing us to write the relationship

$$\Delta\rho_h = \Delta r \sin\theta \tag{3.4}$$

$$\cos\theta = \frac{H}{\rho} \tag{3.5}$$

By this relationship, we see that the sway increases the range from the ideal repeat track line to reflectors on the same side as the offset, and decrease the range to reflectors on the opposite side. This may easily be verified qualitatively by inspection of Figure 3.12.

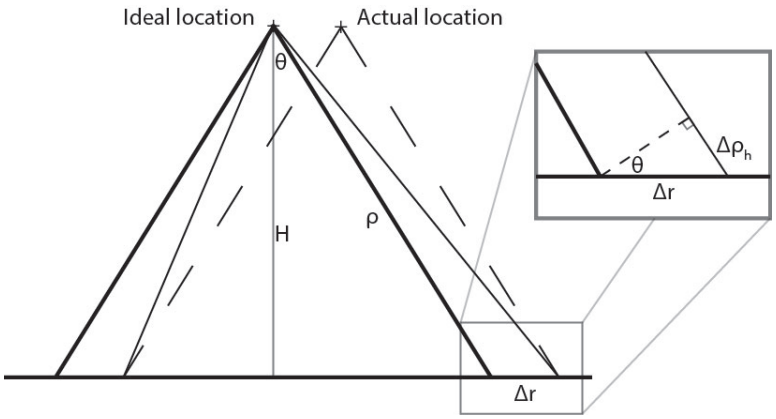

Figure 3.12: **Schematic diagram of the range correction required to account ship sway. The ideal uncorrected range measurement is shown by the thick lines, which are offset from the actual measurements shown by the dashed line by some distance Δr. For the correlation between the repeated tracks, we require the corrected ranges from the ideal ship location along the repeated track and the actual reflectors, shown by the thin solid lines. The ship track is into the page.**

We must also account for variations in the ship heading. Nominally, the range coordinate is orthogonal to the azimuth coordinate, which in turn is parallel to the ideal repeat ship track. However, the range is actually perpendicular to the instantaneous heading of the ship; deviations of this from the ideal track will rotate the range axis, causing the reflectors sensed by the array to be mis-located in both azimuth and range.

For a given reflector measured by a ship with yaw deviation α, we may form a right triangle with the measured range to the reflector as the hypotenuse and the azimuth correction and corrected range as the legs (Fig 3.13). We may then write the range correction as

$$\cos\alpha = \frac{(\rho + \Delta\rho_\alpha)\sin\theta}{\rho\sin\theta} \tag{3.6}$$

$$\Delta\rho_\alpha = \rho\left(\sqrt{\sin^2\theta\cos^2\alpha + \cos^2\theta} - 1\right) \tag{3.7}$$

Note that the range correction is by definition always negative. In addition, we are implicitly assuming that the look angle of the corrected range is approximately equivalent to the look angle of the actual range. This should be reasonable as long as α is sufficiently small. The corresponding azimuth correction is

$$\Delta a_\alpha = \rho\sin\alpha\sin\theta \tag{3.8}$$

The azimuth correction will be positive on one side of the ship and negative on the other side.

The errors due to horizontal baseline shifts display an odd symmetry that causes them to map directly as an apparent horizontal shift of the seafloor. Luckily, this baseline is easy to measure as it can be directly solved for alongside the azimuth coordinate. Another reason why the horizontal baseline contributes a larger error is due simply to the difficulty of exactly repeating ship tracks. This correction is bounded by Δr, which could easily be many tens or even hundreds of meters.

The corrections due to the orientation of the vessel are remarkably similar, showing similar magnitudes for the azimuth and range corrections. The range correction due

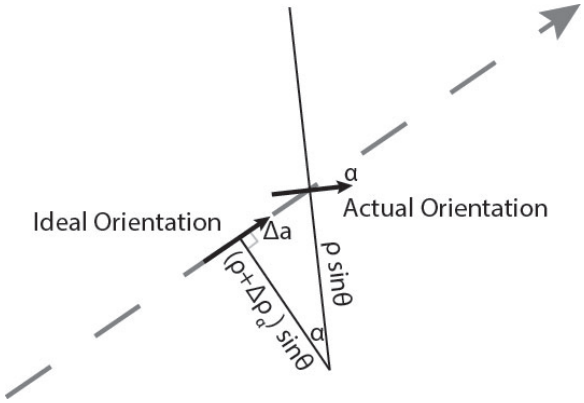

Figure 3.13: **Schematic diagrams of the range correction required due to errors in the ship heading. The perspective is a bird's eye view upon the ideal repeat ship track.**

to the orientations show an even symmetry, and may have a magnitude of a few meters to a few tens of meters, assuming a range on the order of 5000 m. The azimuth correction is much larger in magnitude, being on the order of a few tens to hundreds of meters, and rotating the coordinate frame.

However, it may not always be necessary to apply the correction for the ship's heading, as the sonar has a yaw stabilization system that, when operating, automatically aligns the ping with the average course of the ship, eliminating the need for this correction. In addition, it may be unreasonable to apply a correction due to the pitch, which varies on the order of seconds and goes through multiple cycles over the course of a single ping.

3.6.5 Data Correlation

Before performing cross-correlation on the two data sets, we must first transcribe them into coregistered grid files. We do so using algorithms from the Generic Mapping Tools (GMT) programming suite [Smith and Wessel 1990]. We first mitigate the effects of any outliers by performing a blockmedian, which returns the median amplitude of the pixels that fall within grid cells defined by the user. We may then create the grid using

the algorithm xyz2grd. During this process, the grids are coregistered as long as they have the same bounds and cell size; both are easy for the user to manipulate.

Alternatively, grids may be generated using the GMT algorithm surface, which uses a tension spline to fit the data. Using this method, we recommend a tension factor of 0.4 for gridding sidescan data, as opposed to the tension of 0.35 recommended by Smith and Wessel [1990] and used by Fujiwara et al. [2011]. We have also found our best results by using a convergence limit of 0.08 to prevent the spline from introducing high frequency noise into the grid.

We calculate the normalized cross-correlation criteria, as it has been shown to be the most stable correlation criterion [Pan et al. 2006]. We compute the cross-correlation for pixel offsets within a user-defined search radius of some initial guess of deformation [Pan et al. 2009]. We define the displacement between the two surveys as being the displacement that yields the maximum correlation [Sjödahl and Benckert 1993]; by fitting an appropriate function to the correlation peak we may obtain the displacement to sub-pixel accuracy. We have found an appropriate model to be that of a Gaussian peak, as long as we only consider points in the neighborhood of the maximum. Coincidentally, only having to compute the correlation in the neighborhood of the peak drastically reduces the required computation time. This method is easily able to discern sub-pixel offsets, but is subject to a few limitations, the most obvious being that the user must have an appropriate guess before running the algorithm. A more subtle limitation is that this algorithm is most sensitive to displacements near the initial guess. As the guess may be iteratively improved, this algorithm is least accurate for offsets exactly halfway between pixels.

3.7 Acknowledgments

This work was supported by the National Science Foundation, Marine Geology and Geophysics division, grant 1536386. Data are available through the National Centers for Environmental Information (NCEI) bathymetric data viewer, accessible at *https://maps.ngdc.noaa.gov/viewers/bathymetry/*.

Chapter 3, in full, is a reprint of the material as it appears in the Journal of Geophysical Research Solid Earth: DeSanto, J. B., D. T. Sandwell, C. D. Chadwell, "Seafloor Geodesy from Repeated Sidescan Sonar Surveys", *J. Geophys. Res. Solid Earth*, 121, pp.4800-4813, 2016. The dissertation author is the primary investigator and author of this paper.

References

Bürgmann, Roland and Chadwell, David (2014). "Seafloor Geodesy". In: *Annual Review of Earth and Planetary Sciences* 42.1, pp. 509–534. DOI: 10.1146/annurev-earth-060313-054953.

Bürgmann, Roland, Rosen, Paul A., and Fielding, Eric J. (2000). "Synthetic Aperture Radar Interferometry to Measure Earths Surface Topography and Its Deformation". In: *Annual Review of Earth and Planetary Sciences* 28.1, pp. 169–209. DOI: 10.1146/annurev.earth.28.1.169. eprint: http://dx.doi.org/10.1146/annurev.earth.28.1.169. URL: http://dx.doi.org/10.1146/annurev.earth.28.1.169.

Caress, D W, Clague, D A, Paduan, J B, Martin, J F, and Dreyer, B M (2012). "Repeat bathymetric surveys at 1-metre resolution of lava flows erupted at Axial Seamount in April 2011". In: *Nat. Geosci.* 5, p. 483.

Caress, David W. and Chayes, Dale N. (1996). "Improved processing of Hydrosweep DS multibeam data on the R/V Maurice Ewing". English. In: *Marine Geophysical Researches* 18.6, pp. 631–650. ISSN: 0025-3235. DOI: 10.1007/BF00313878. URL: http://dx.doi.org/10.1007/BF00313878.

Chadwell, C D and Spiess, F N (2008). "Plate motion at the ridge-transform boundary of the south Cleft segment of the Juan de Fuca Ridge from GPS-acoustic data". In: *J. Geophys. Res.* 113, B04415.

Chadwick, William W., Embley, Robert W., and Fox, Christopher G. (Apr. 1991). "Evidence for volcanic eruption on the southern Juan de Fuca ridge between 1981 and 1987". In: *Nature* 350.6317, pp. 416–418. URL: http://dx.doi.org/10.1038/350416a0.

Chadwick, William W., Embley, Robert W., and Shank, Timothy M. (1998). "The 1996 Gorda Ridge eruption: geologic mapping, sidescan sonar, and SeaBeam comparison results". In: *Deep Sea Research Part II: Topical Studies in Oceanography* 45.12, pp. 2547 –2569. ISSN: 0967-0645. DOI: http://dx.doi.org/10.1016/S0967-0645(98)00083-6. URL: http://www.sciencedirect.com/science/article/pii/S0967064598000836.

Chen, D. J., Chiang, F. P., Tan, Y. S., and Don, H. S. (1993). "Digital speckle-displacement measurement using a complex spectrum method". In: *Appl. Opt.* 32.11, pp. 1839–1849. DOI: 10.1364/AO.32.001839. URL: http://ao.osa.org/abstract.cfm?URI=ao-32-11-1839.

Davis, J. L., Fialko, Y., Holt, W. E., Miller, M. M., Owen, S. E., Pritchard, M. E., and (Eds.) (2012). *A Foundation for Innovation: Grand Challenges in Geodesy*. Report from the Long-Range Science Goals for Geodesy Community Workshop, UNAVCO, Boulder, Colorado, 79 pp.

Fox, Christopher G., Chadwick, William W., and Embley, Robert W. (1992). "Detection of changes in ridge-crest morphology using repeated multibeam sonar surveys". In: *Journal of Geophysical Research: Solid Earth* 97.B7, pp. 11149–11162. ISSN: 2156-2202. DOI: 10.1029/92JB00601. URL: http://dx.doi.org/10.1029/92JB00601.

Fujiwara, T, Kodaira, S, No, T, Kaiho, Y, Takahashi, N, and Kaneda, Y (2011). "The 2011 Tohoku-oki earthquake: displacement reaching the trench axis". In: *Science* 334, p. 1240.

Fujiwara, Toshiya, Masaki, Yuka, and Yamamoto, Fujio (2014). "Evaluation of spatial resolution and estimation error of seafloor displacement observation from vessel-based bathymetric survey by use of AUV-based bathymetric data". In: *Marine Geophysical Research* 36.1, pp. 45–60. ISSN: 1573-0581. DOI: 10.1007/s11001-014-9242-8. URL: http://dx.doi.org/10.1007/s11001-014-9242-8.

Gagnon, Katie, Chadwell, C. David, and Norabuena, Edmundo (Mar. 2005). "Measuring the onset of locking in the Peru-Chile trench with GPS and acoustic measure-

ments". In: *Nature* 434.7030, pp. 205–208. URL: http://dx.doi.org/10.1038/nature03412.

Joughin, Ian (2002). "Ice-sheet velocity mapping: a combined interferometric and speckle-tracking approach". In: *Annals of Glaciology* 34.1, pp. 195–201. DOI: doi:10.3189/172756402781817978. URL: http://www.ingentaconnect.com/content/igsoc/agl/2002/00000034/00000001/art00030.

Kido, M., Osada, Y., Fujimoto, H., Hino, R., and Ito, Y. (2011). "Trench-normal variation in observed seafloor displacements associated with the 2011 Tohoku-Oki earthquake". In: *Geophysical Research Letters* 38.24. ISSN: 1944-8007. DOI: 10.1029/2011GL050057.

Pan, Bing, Xie, Huimin, Xu, Boqin, and Dai, Fulong (2006). "Performance of sub-pixel registration algorithms in digital image correlation". In: *Measurement Science and Technology* 17.6, p. 1615. URL: http://stacks.iop.org/0957-0233/17/i=6/a=045.

Pan, Bing, Qian, Kemao, Xie, Huimin, and Asundi, Anand (2009). "Two-dimensional digital image correlation for in-plane displacement and strain measurement: a review". In: *Measurement Science and Technology* 20.6, p. 062001. URL: http://stacks.iop.org/0957-0233/20/i=6/a=062001.

Sato, Mariko, Ishikawa, Tadashi, Ujihara, Naoto, Yoshida, Shigeru, Fujita, Masayuki, Mochizuki, Masashi, and Asada, Akira (2011). "Displacement Above the Hypocenter of the 2011 Tohoku-Oki Earthquake". In: *Science* 332.6036, p. 1395. DOI: 10.1126/science.1207401.

Schreier, Hubert W., Braasch, Joachim R., and Sutton, Michael A. (2000). "Systematic errors in digital image correlation caused by intensity interpolation". In: *Optical Engineering* 39.11, pp. 2915–2921. DOI: 10.1117/1.1314593. URL: http://dx.doi.org/10.1117/1.1314593.

Sjödahl, M. and Benckert, L. R. (1993). "Electronic speckle photography: analysis of an algorithm giving the displacement with subpixel accuracy". In: *Appl. Opt.* 32.13, pp. 2278–2284. DOI: 10.1364/AO.32.002278. URL: http://ao.osa.org/abstract.cfm?URI=ao-32-13-2278.

Smith, W. and Wessel, P. (1990). "Gridding with continuous curvature splines in tension". In: *GEOPHYSICS* 55.3, pp. 293–305. DOI: 10.1190/1.1442837.

Spiess, F N (1985). "Suboceanic geodetic measurements". In: *IEEE Trans. Geosci. Remote Sens.* GE-23, p. 502.

Spiess, F. N., Chadwell, C. D., Hildebrand, J. A., Young, L. E., G. H. Purcell, Jr., and Dragert, H. (1998). "Precise GPS/Acoustic positioning of seafloor reference

points for tectonic studies". In: *Phys. of the Earth and Plan. Int.* 108, pp. 101–112.

Tomita, Fumiaki, Kido, Motoyuki, Osada, Yukihito, Hino, Ryota, Ohta, Yusaku, and Iinuma, Takeshi (2015). "First measurement of the displacement rate of the Pacific Plate near the Japan Trench after the 2011 Tohoku-Oki earthquake using GPS/acoustic technique". In: *Geophysical Research Letters*. ISSN: 1944-8007. DOI: 10.1002/2015GL065746.

Watanabe, Shunichi, Sato, Mariko, Fujita, Masayuki, Ishikawa, Tadashi, Yokota, Yusuke, Ujihara, Naoto, and Asada, Akira (2014). "Evidence of viscoelastic deformation following the 2011 Tohoku-Oki earthquake revealed from seafloor geodetic observation". In: *Geophysical Research Letters* 41.16, pp. 5789–5796. ISSN: 1944-8007. DOI: 10.1002/2014GL061134.

Wdowinski, Shimon, Sudman, Yonadav, and Bock, Yehuda (2001). "Geodetic detection of active faults in S. California". In: *Geophysical Research Letters* 28.12, pp. 2321–2324. ISSN: 1944-8007. DOI: 10.1029/2000GL012637. URL: http://dx.doi.org/10.1029/2000GL012637.

Wilcock, W., Bodin, P., Delaney, J., Vidale, J., and (Conveners) (2012). *Workshop Report on Seafloor Geodesy in Cascadia*. June 11-12, 2012. University of Washington.

Chapter 4

Seafloor Geodesy from Repeated Sidescan Sonar Surveys: Optimal Survey and Processing Parameters

4.1 Introduction

Among the great geodetic challenges in Earth science is the problem of seafloor geodesy. Offshore earthquakes, volcanoes, and landslides can cause displacements on the meter scale or larger but are difficult to measure directly because the microwave signals that enable the collection of GPS and InSAR data cannot penetrate deeper than a few millimeters in seawater. As a result, specialized tools have been developed specifically to measure displacement on the seafloor, the most accurate of which are GPS-Acoustic and Bottom Pressure Recorders [Bürgmann and Chadwell 2014]. While these measurements are accurate to the centimeter scale, they are limited in that they are point measurements. Another instrument that may be used for seafloor geodetic application is the multibeam sonar, which collects bathymetry measurements in a broad swath beneath a research

vessel.

The method for measuring seafloor displacement with a multibeam sonar involves collecting repeated surveys of a patch of seafloor. Displacement between the surveys may be calculated via the normalized cross-correlation between surveys. The offset that yields the peak correlation coefficient is our desired measurement. The precision of a displacement calculated in this way is a sub-pixel fraction of the data resolution; a 12 kHz multibeam sonar has a bathymetry resolution on the order of 100-150 m for seafloor depths of approximately 3000 m, so it is possible to resolve displacements on the order of 10 m. This is less accurate than the displacements measurable using GPS-Acoustic or Bottom Pressure Recorders, but the multibeam bathymetry covers a far greater area of seafloor than these instruments, which yield point measurements.

Previous studies have employed differential multibeam bathymetry to measure the seafloor displacement across the Japan Trench due to 2011 M_ω 9.0 Tohoku-Oki earthquake in the regions offshore Miyagi [Fujiwara et al. 2011] and Sanriku [Fujiwara et al. 2017]. These studies were able to identify the distribution of surface displacement with an accuracy on the order of 3-20 m. A study by DeSanto et al. [2016] proposed using digital image correlation on sidescan sonar rather than multibeam bathymetry. The accuracy of such measurements is a sub-pixel fraction of the data resolution. Thus, the theoretical displacement resolution obtained from image correlation of sidescan data should be superior to that obtained from multibeam bathymetry because the resolution of sidescan is constant in slant range and thus independent of seafloor depth; contrast with multibeam bathymetry resolution which becomes coarser in deeper waters. In addition, the sidescan data are less sensitive to roll biases than multibeam bathymetry. The DeSanto et al. [2016] study estimated a displacement precision of 0.75 m in the range dimension by analyzing legacy multibeam sidescan data from cruises in offshore Cascadia and Southern California. However, that study was unable to quantify the contribution of the

correlation algorithm, navigation, and sound speed profile to the measurement uncertainty or how these uncertainties are impacted by survey design.

There are few requirements to be able to collect a displacement measurement using sonar data. The key experiment design involves returning to a previously surveyed region to collect a second data set of bathymetry and sidescan utilizing the same geometry as the older survey. In order to facilitate a valid cross-correlation between the reference and repeat surveys, we need sufficient information about the ship location and sound velocity profile for both surveys. The ship location is required to properly locate any patch of seafloor in space since the research vessel acts as the reference from which ranges are measured. Ideally the ship navigation has been post-processed using a technique such as Precise Point Positioning (PPP) as shown in DeSanto et al. [2018], but the real-time solution of a dual-frequency navigation system such as the Kongsberg Seapath 330+ is sufficient to eliminate receiver drift on the order of 1 m/hr due to variations of total electron content in the ionosphere. An appropriate sound velocity profile is required to properly perform raytracing when solving for the range of any sonar echo; poor constraints on the sound velocity can result in up to a few meters of range error as well as a poorly constrained look angle.

We seek to clarify the accuracy of displacement measurements from repeated sidescan surveys attainable given a wide variety of acquisition parameters. Some parameters, such as the ship speed and seafloor depth, influence the along-track sounding density on the seafloor with slower speeds and shallower depths allowing for a greater sounding density and thus more precise measurement. Sonar frequency and bandwidth affect sounding density in the across-track direction but also influences the swath width, with higher frequencies reducing the range of look angles from which data may be collected with an acceptable noise level.

The track separation of the repeated tracks may play a significant role as the

different ship locations will modify the range and look angle to reflectors on the seafloor between tracks as explained in Chapter 3 [DeSanto, Sandwell, and Chadwell 2016]. Likewise, the quality of our knowledge of the ship position during acquisition places bounds on how well we may locate a patch of seafloor due to the sonar ranges being relative to the vessel.

In addition to testing these parameters we include general tests of the displacement estimation. The first of these tests is to process a pair of sidescan tracks in which the repeat track of data has the opposite heading as the reference track. The second of these tests is a closure test to determine if the solutions obtained from pairs selected from a trio of repeated tracks are self-consistent.

We also include a discussion of the sensitivity of the data to perturbations of the sound velocity profile, as this informs our processing structure.

In this study we consider data from four cruises: Roger Revelle, 2016, Leg 5 (RR1605), Sally Ride, 2017, Leg 4 (SR1704), Okeanos Explorer, 2010, Leg 6 (EX1006), and Okeanos Explorer, 2015, Leg 5 (EX1505). The RR1605 and SR1704 cruises contain pairs of repeated tracks and act as calibration experiments designed to explore the dependence of the displacement measurement upon various acquisition parameters. The EX1006 and EX1505 cruises share a similar transit and thus serve as an example for how such surveys may be collected in practice. The Okeanos Explorer employs a 30 kHz Kongseberg EM322 multibeam instead of the 12 kHz EM122 used by the other vessels, so these cruise provide an opportunity to test the effects of sonar frequency on positioning accuracy.

4.2 Processing Methods

Our data consists of two multibeam sidescan tracks that have been collected in the same area at different times. These tracks are close repeats with similar heading and location, and are ideally collected at the same speed with similar instruments so that they have comparable data density. For this analysis we consider 4 variables present in the sidescan data. The fundamental data we observe is the amplitude, or backscatter, of the sidescan echoes. Each ping consists of many points of amplitude, each with a unique look angle θ, measured from vertical, and range ρ, the distance between the sonar and the point on the seafloor from which the echo reflected. For 12 kHz multibeam sonars, the range resolution is 11.25 m. Amplitude points in a single ping are arranged roughly across track; we log the position of each ping with a value called the azimuth, the along-track distance from a shared reference point.

Multibeam and sidescan data are collected in "pings", which consist of chirp pulses emitted by the sonar; reflections of a single pulse from the seafloor are logged before another pulse is emitted. Although each ping contains bathymetry and sidescan information, sidescan data have a finer resolution than the bathymetry. This oversampling means we must interpolate bathymetry data for an appropriate model of range and look angle (required to correct the sidescan range for baseline separations between the reference and repeat tracks) for sidescan amplitudes. Thus, the zeroth step for the sidescan processing is to process the bathymetry; we do so using the MB-System software [Caress and Chayes 2015]. At this stage we implement appropriate sound velocity profiles, tidal corrections, and navigation corrections if possible.

Data processing for the sidescan tracks follows the methodology described in DeSanto et al. [2016]. First, we rotate the repeated tracks into a consistent coordinate frame of range and azimuth, correcting for across-track and heading deviations from a

reference ship track. Second, we create grid files of backscatter amplitude as a function of range and azimuth. The sum and difference of an example pair of gridded sidescan data is shown in Figure 4.1. The sum of the sidescan grids shows the detailed backscatter of the seafloor while the difference resembles a random noise distribution, showing that that a cross-correlation between the reference and repeat is well-founded. The range displacement of the port and starboard grids is computed independently by solving for the pixel offset that yields the maximum of a normalized cross correlation function, yielding a single displacement for each side. After estimating the port and starboard range displacements ρ, we may derive an expression for the average displacement u as a function of look angle θ in a geographical coordinate frame by considering the geometry of the swath:

$$\begin{aligned} u_{acrosstrack} &= \frac{1}{2\theta_{max}} \int_{-\theta max}^{\theta max} \rho(\theta) \sin\theta \partial\theta \\ u_{vertical} &= \frac{1}{2\theta_{max}} \int_{-\theta max}^{\theta max} \rho(\theta) \cos\theta \partial\theta \end{aligned} \tag{4.1}$$

The cross correlation analysis yields one range displacement estimate for each of the port and starboard sides of the swath, so $\rho(\theta)$ resembles a step function. Making this assumption, we may evaulate the above integrals as:

$$\begin{aligned} u_{acrosstrack} &= \frac{1 - cos\theta_{max}}{2\theta_{max}} (\rho_{starboard} - \rho_{port}) \\ u_{vertical} &= \frac{\sin\theta_{max}}{2\theta_{max}} (\rho_{starboard} + \rho_{port}) \end{aligned} \tag{4.2}$$

The maximum look angle of a 12 kHz multibeam sonar is 75°, but we only consider data with a look angle less than 65° due to the higher noise at higher look angles.

Assuming $\theta_{max} = 65$, the expressions for u evaluate to:

$$u_{acrosstrack} \approx 0.25(\rho_{starboard} - \rho_{port})$$
$$u_{vertical} \approx 0.4(\rho_{starboard} + \rho_{port}) \tag{4.3}$$

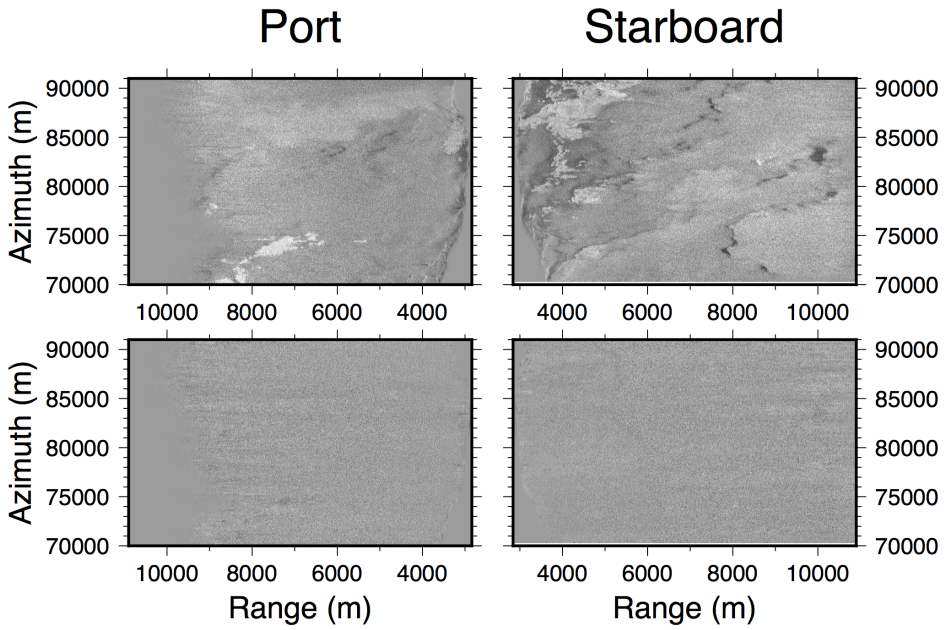

Figure 4.1: **Sum (upper) and difference (lower) of two repeated sidescan sonar tracks collected during the RR1606 cruise. The port and starboard sidescan data are plotted separately.**

4.3 Experiments

4.3.1 RR1605 Cruise at the Ayu Trough

We performed a calibration survey during the RR1605 cruise in 2016 which consisted of five repeating multibeam surveys collected above the Ayu Trough approx-

imately 200 nautical miles southwest of Palau. The Ayu Trough is a slow spreading center denoting the southern plate boundary between the Philippine Sea Plate and the Caroline Sea Plate [Weissel and Anderson 1978]. The plate motion across this boundary is difficult to resolve; marine seismic studies estimate the spreading rate to be 3.5-9.1 mm/yr based upon sediment thicknesses and sedimentation rates [Fujiwara et al. 1995; Hong and Lee 2002]. The seafloor in this region in approximately 3500-4300 meters deep and has a topographic fabric oriented approximately North-South, reflecting the plate boundary between the Philippine and Caroline Sea Plates. The survey area contains both a rough and reflective topographic high as well as a smoother topographic low.

The RR1605 experiment consists of repeated surveys consisting of 4 tracks (Figures 4.2 and 4.3): Track 1 is 12 nautical miles long and oriented due East. Track 2 is 8 nautical miles long and oriented southwest with a bearing of 225°. Track 3 is 12 nautical miles long and oriented due North, forming a cross with Track 1. Track 4 is an 8 nm long diagonal track similar to Track 2, and connects the end of Track 3 with the start of Track 1 to form a closed loop. Tracks 1 & 3 were collected at a speed of 6 knots and have across-track separations varying from 0-300 meters across track. Track 2 was collected at a speed of 4 knots and Track 4 was collected at a speed of 8 knots. Neither diagonal track has a variable track separation between surveys.

Displacements measured between every valid combination of repeated surveys are plotted in Figure 4.4, colored according to ship track. Error bars are calculated according to the reduced χ^2 values computed by the peak-fitting algorithm, and agree with the precision reported in DeSanto et al. [DeSanto, Sandwell, and Chadwell 2016]. The vertical displacement measured in all tracks varies within 2 meters, but the across-track displacement has a variance dependent on track. In the following analysis we shall use these measurements to estimate the influence of track orientation, track separation, and ship speed on displacement uncertainty.

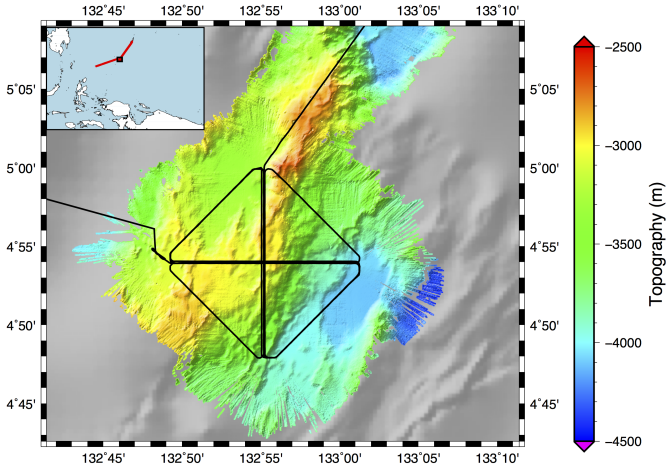

Figure 4.2: **Topography collected during the RR1605 cruise (colored). Regional topography from before the cruise shown in greyscale. Regional context of the cruise shown in inset map.**

A method by which we may assess the accuracy of displacement estimates is by forming closed loops of horizontal and vertical offsets from surveys in subsets of three or more. If no random noise is introduced into the measurements during the data processing, the displacement between any two surveys should be predictable using the sum of displacements obtained using an independent survey as a reference or repeat. We form closed loops using every possible combination of survey triplets for each of the four RR1605 tracks, excluding only the S3T1 survey, which was previously demonstrated to not yield reliable results due to having been collected with opposite heading to the other Track 1 surveys.

Closure test results are plotted in Figure 4.5 separated by track, with the displacement between two surveys plotted on the x-axis and the prediction from the other displacements in the loop plotted on the y-axis. In this configuration, points that plot closer to the line denoted by $y = x$ are considered more accurate. Table 4.1 displays the RMS of closure differences for the across-track and vertical displacement estimates associated with each track. The track with the most consistent measurements is Track 2

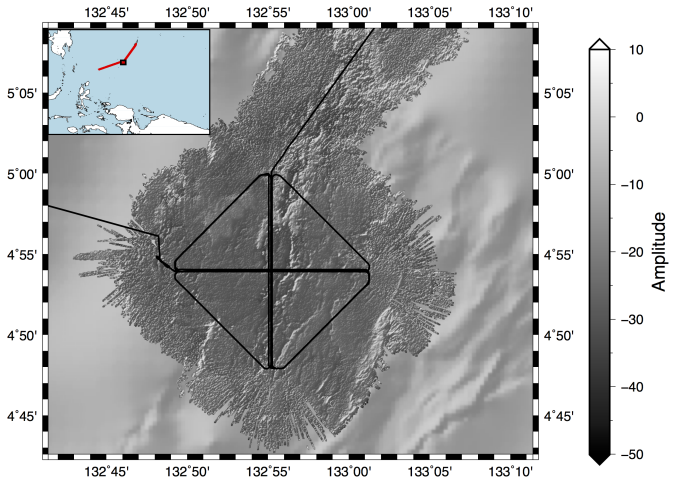

Figure 4.3: **Sidescan backscatter collected during the RR1605 cruise. Regional topography from before the cruise shown in greyscale. Regional context of the cruise shown in inset map.**

Table 4.1: **RMS values of mis-closures of loops of displacement measurements between repeated sidescan sonar surveys collected during the RR1695 cruise.**

Track	Ship Speed (knots)	RMS Across-track Mis-closure (m)	RMS Vertical Mis-closure (m)
1	6	0.65	0.75
2	4	0.25	0.37
3	6	0.33	0.45
4	8	0.67	0.65

while the tracks with the least consistent measurements are Tracks 1 & 4. Tracks 1 & 3 (blue and red, respectively) were collected at a speed of 6 knots and variable baseline, Track 2 (purple) was collected at a speed of 4 knots, and Track 4 (orange) was collected at a speed of 8 knots. Track 1 displacements show the largest range of mis-closure while Track 2 displacements show the smallest range. At first glance, this lends credence to the hypothesis that data collected at a slower ship speed is of higher fidelity in that the slowest track (Track 2) yielded the most consistent results, but there is also rough equivalence in the spread of mis-closure between the Track 3 data collected at 6 knots and the Track 4 data collected at 8 knots.

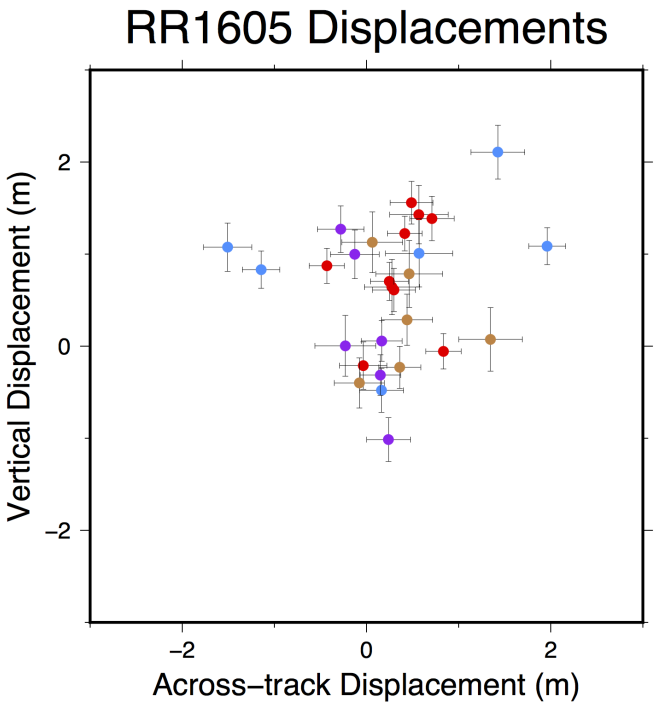

Figure 4.4: **Displacement estimates between repeated sidescan sonar surveys collected during the RR1605 cruise. Colored points denote different tracks in the cruise: blue denotes Track 1, red Track 2, purple Track 3, and orange Track 4.**

We analyze the horizontal and vertical displacements measured between RR1605 surveys as a function of track separation. Figure 4.6 shows no discernible dependence of displacement on track separation, implying that precise displacement measurements may be obtained even from tracks that are separated by as much as 300 meters. We interpret this as evidence that the repeated tracks have been successfully translated to a common reference track, eliminating range errors that would arise due to ship sway from the reference.

Another way to diagnose the quality of these displacement measurements is to plot them as a function of peak correlation, as shown in Figure 4.7. Of particular note are a set of displacement measurements with significantly lower correlation coefficient (approximately 0.13) than the other measurements. These measurements are all associated

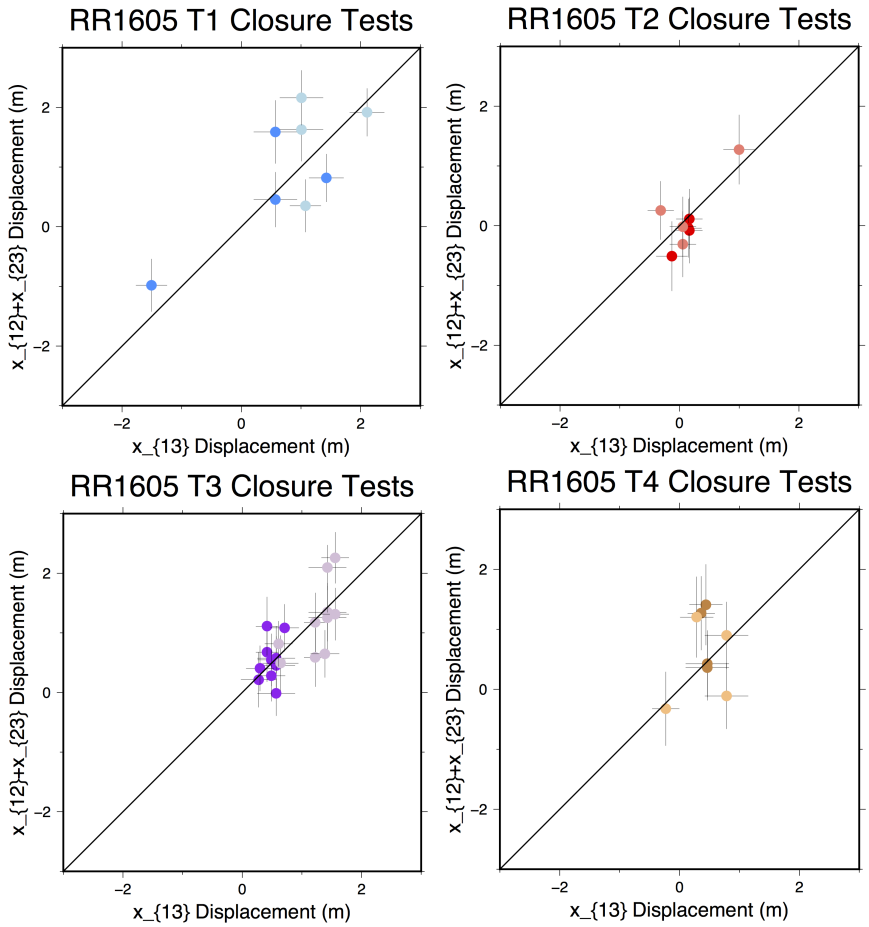

Figure 4.5: **Closure of across-track and vertical displacements between RR1605 tracks. Horizontal axis plots the sum of two displacement measurements while the vertical axis plots the displacement that closes the loop. The line $y = x$ denotes perfect closure.**

with one survey of sidescan data, S3T1, a repeat with heading oriented 180°relative to the reference track as a test of the limits by which we may design a repeated sidescan survey. Data from this track were processed using the same methodology as the other surveys, with the only notable processing difference being the yaw compensation, which rotated the track 180°to align with the reference. The displacement estimates computed with track S3T1 range from 2-10 m in the across-track component and 8-22 m in the vertical component with 2σ uncertainties from 2-10 m, significantly poorer than other

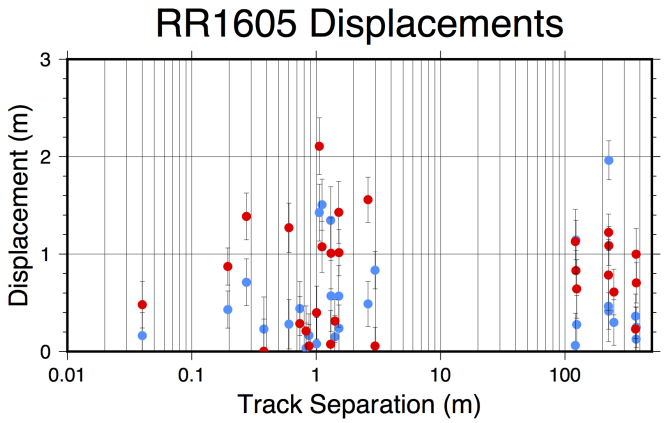

Figure 4.6: **Across-track (blue) and vertical (red) displacement estimates between repeated RR1605 sidescan surveys, plotted according to track separation.**

displacement estimates from the RR1605 cruise. However, the lower correlation values imply little common signal preserved between these track pairs, indicating a failure during processing to properly rotate the signals into a common reference frame. This implies that there may be some critical heading difference in repeated tracks beyond which we may no longer measure a displacement between surveys. However, we do not have a sufficient variation in the survey orientations to identify this critical heading difference.

4.3.2 SR1704 Cruise at the Inner California Borderlands

In contrast to other experiments discussed in this study, the SR1704 cruise was conducted in a region of offshore seismic hazard, the inner California Borderland. The inner California Borderland is the region offshore California and south of Point Conception, characterized by high-relief seafloor topography bounded by primarily right-lateral strike-slip faults oriented NNW. This is a zone of transtension that formed after the subduction of the East Pacific Rise at 27 Ma [Atwater 1970] to accommodate motion between the Pacific and North American Plates. Significant regional consequences of the

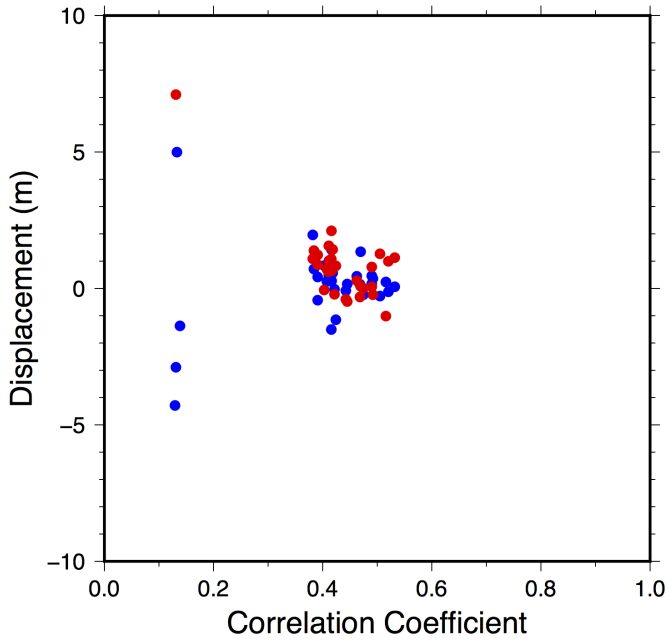

Figure 4.7: **Across-track (blue) and vertical (red) displacement estimates between repeated RR1605 sidescan surveys, plotted according to cross-correlation coefficient averaged between port and starboard data.**

transtensional motion are the rotation of the Western Transverse Range by 90-110°at 16 Ma and the opening of the Gulf of California at 5 Ma. In the present day, approximately 8mm/yr of right-lateral strike-slip motion between the Pacific and North American Plates is accommodated by faults in the inner California Borderland [Platt and Becker 2010]. Significant faults in this region are the Newport-Inglewood-Rose Canyon Fault, which accommodates 1-1.5 mm/yr of plate motion [Lindvall and Rockwell 1995], the Palos Verdes Fault, which accommodates 2.7-3.0 mm/yr of plate motion [McNeilan, Rockwell, and Resnick 1996], and the San Diego Trough Fault, which accommodates 1.5 mm/yr of plate motion [Ryan et al. 2012].

The SR1704 cruise consists of two pairs of surveys above a seamount southeast of Santa Catalina Island in the Southern California Borderlands (Figures 4.8 and 4.9). This seamount is bisected by the San Diego Trough Fault (SDTF), which creates a striking

surface feature that could shift by a measurable amount in the event of an earthquake along the SDTF. During this cruise our ability to collect quality multibeam data was hindered by large swells coming from the West; the surveys were oriented North-South and Northeast-Southwest to minimize noise from the sea state. All surveys were 15 km long and collected at a ship speed of 5 knots with a Kongsberg EM122 multibeam sonar. Ship navigation was collected with a Kongsberg Seapath 330+, but due to instrument failure early in the cruise the raw data from the first surveys was lost. Thus, we do not have a complete set of the raw navigation and a kinematic post-processed GPS solution is unavailable for these surveys.

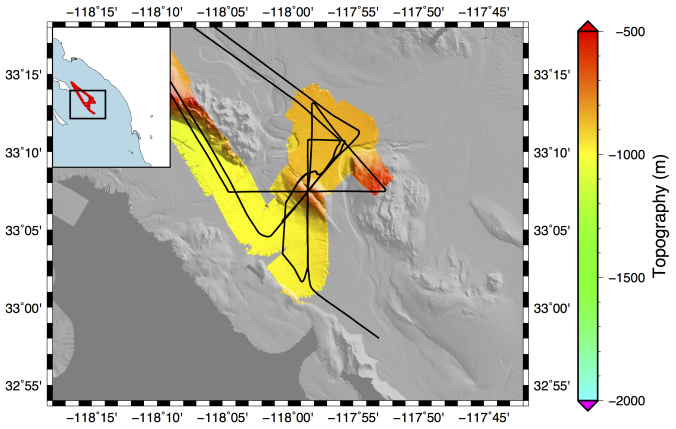

Figure 4.8: **Topography collected during the SR1704 cruise (colored). Regional topography from before the cruise shown in greyscale. Regional context of the cruise shown in inset map.**

The estimates of across-track and vertical displacement measured between the SR1704 surveys were many meters in magnitude and demonstrated similar uncertainties as the RR1605 measurements (Table 4.2). These measurements capture uncertainties due primarily to errors in navigation, as well as unmodeled sound velocity errors. Because of the lost navigation data in the early surveys we must rely on the real-time ship GPS solution for these data. As a result, navigation errors for this survey are on the meter scale rather than the centimeter scale (see Chapter 5 for a more in-depth discussion of

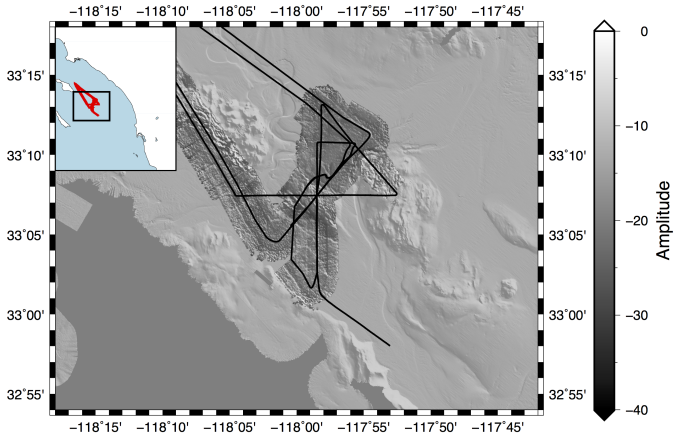

Figure 4.9: **Sidescan backscatter collected during the SR1704 cruise. Regional topography shown in greyscale. Regional context of the cruise shown in inset map.**

Table 4.2: **Displacements and 2σ uncertainties measured between repeated surveys collected during the SR1704 cruise.**

Track	Correlation	Across-track (m)	Vertical (m)	2σ (m)
North-South	0.35	3.34	1.20	0.55
Diagnol	0.49	-1.51	6.09	0.70

the navigation uncertainties of raw vs post-processed ship navigation).

4.3.3 Repeated Okeanos Explorer Transit Cruises

The final data set we considered was a pair of transit cruises by the Okeanos Explorer. The cruises EX1006 from 2010 and EX1505 from 2015 were transits from Hawaii to San Francisco that had three sections above the Pacific Plate interior that repeated with an average track separation of 30-200 m. These repeated sections were 60-150 km in length and were collected at a transit speed of 12 knots. The multibeam sonar used on the Okeanos Explorer cruises was a Kongsberg EM322. This instrument differs from the EM120 and EM122 sonars discussed in the previous sections in that the EM322 transmits acoustic pulses with frequency bands of 30 kHz instead of 12 kHz. Because

Table 4.3: **Displacements and 2σ uncertainties measured between repeated transits of the *R/V Okeanos Explorer*.**

Track	Correlation	Across-track (m)	Vertical (m)	2σ (m)
1	0.01	5.13	-3.02	4.20
2	0.08	25.82	-11.34	3.01
3	-0.00	-6.43	-0.30	0.76

of the higher transmit frequency, the EM322 has a finer slant range resolution with the important caveat that the 30 kHz pulses attenuate faster than the 12 kHz pulses, giving the EM322 sonar a smaller effective range than the EM122. As a result, in deeper waters the EM322 has a narrower swath with a maximum look angle of 10°-20°as opposed to the EM122, which has a maximum look angle of 65°-75°. This is unfortunate because the ground range resolution of sidescan data depends on the cosecant of look angle; the near vertical beams have very poor resolution.

The displacement measurements between these cruises are likely inaccurate because they display near-zero correlation (Table 4.3). Unfortunately, we do not have enough information to determine whether this result is primarily due to the small look angles, fast ship speed, poor navigation, sound velocity, or some combination thereof. In principle, the 30 kHz multibeam should produce data appropriate for displacement measurements, but probably only in waters shallower than 1000 m.

4.4 Effects of Layered Ocean Sound Velocity

Our analysis thus far has assumed a known speed of sound C_d in the water column, from which the beam steering is calculated. In the real world, the sound speed varies as a function of temperature and salinity, both of which change with depth. We demonstrate this for the RR1605 sidescan data by considering the sound speed profiles collected from

a set of seven expendable bathythermograhps (XBTs) collected over the course of the survey. The XBT consists of a disposable sensor deployed over the side of the vessel during a transit that measures temperature as it sinks through the upper 1000 m of the water column. These measurements are used as input alongside a model of conductivity with depth to calculate the sound speed profile using Del Grosso's equations [Del Grosso 1974]. Figure 4.10 shows the XBT profiles collected during the RR1605 cruise as well as the RMS of the XBT profiles. We expect a shallow sound velocity profile derived from an XBT to be most accurate immediately after deployment and deteriorate with time. In this way, we expect the RMS values to provide a estimate of the upper bound of sound speed error as a function of depth, at least for the duration of the cruise.

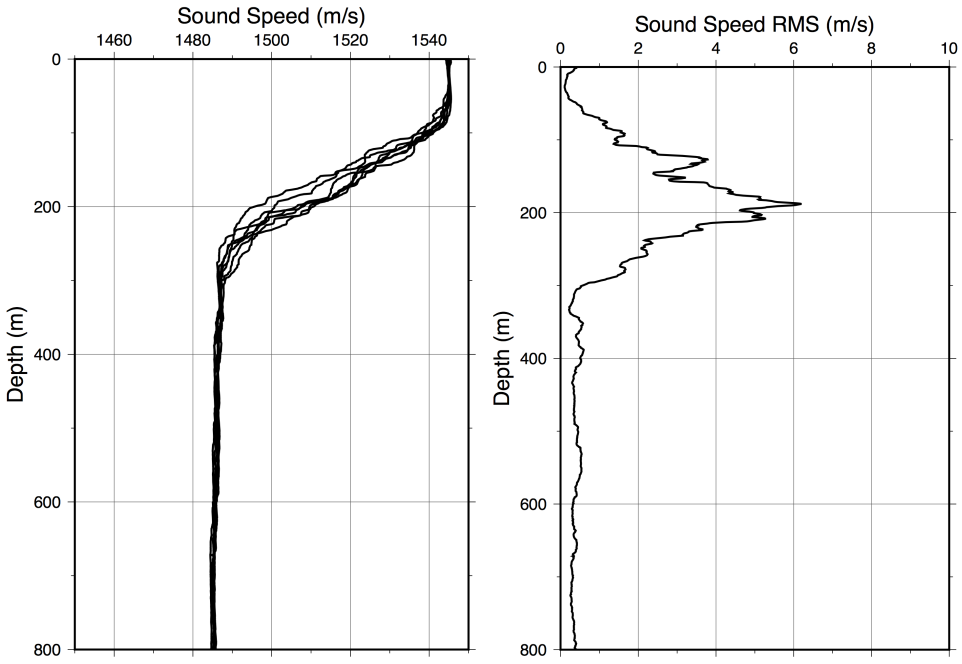

Figure 4.10: **(Left) Sound speed profiles computed from XBTs deployed during the RR1605 cruise. (Right) RMS of sound speed profiles computed from XBTs deployed during the RR1605 cruise.**

Our strategy for using these XBT data to estimate an upper bound for the displacement errors due to sound speed variations is detailed in Chapter 2, derived from de

Moustier [1988], but we shall briefly describe it here. In principle, the depth H of a point on the seafloor may be calculated as $H(\theta) = \rho \cos\theta = \frac{C_d}{2} t \cos\theta$, where C_d is the average sound speed, t is the travel time and ρ is the slant range. This may be separated into perturbations in the surface sound speed and average sound speed profile. To demonstrate the former effect, consider the case in which the sound speed C_d is accurate except for some sound speed perturbation at the sea surface that may be measured during transit. In this case, the slant range is not affected but the apparent look angle will be bent according to Snells Law:

$$\frac{\sin\theta'}{C'} = \frac{\sin\theta_d}{C_d} \tag{4.4}$$

As a result, the apparent range profile is distorted to

$$\rho'(\theta) = \frac{\rho(\theta)}{\cos\theta} \cos\left(\mathrm{Sin}^{-1}\left[\frac{C'}{C_d}\sin\theta\right]\right). \tag{4.5}$$

We estimate the effect of this distortion in Figure 4.11, which shows the percent change in range as a function of look angle calculated assuming $C' = C_{surface} + RMS_{surface}$ using values derived from Figure 4.10. The range difference increases for greater angles, causing greater errors for outer beams. However, this profile is symmetric about nadir, meaning that in the theoretical case of a flat seafloor, the across-track average of range measurements would be unaffected because the range errors would cancel out. In reality the seafloor is not completely flat; we may estimate the across-track uncertainty by multiplying the topographic relief across the swath by the percent change in range at relevant look angles. The maximum topographic relief in the RR1605 survey is approximately 600 m; at a look angle of 50° this corresponds to approximately 0.3 m of across-track uncertainty.

The other source of uncertainty is from errors in sound speed along the ray path

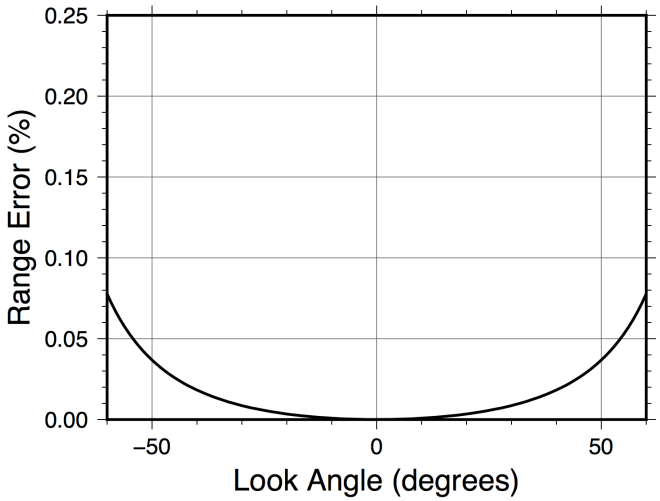

Figure 4.11: **Expected uncertainty in range for the RR1605 cruise due to variations in the surface sound speed, expressed as a percent of range.**

from the ship to the reflector on the seafloor. Assuming sound speed depends only on depth, the strategy to address this is to consider the effect on the average speed of sound by integrating sound speed across the vertical water column, computed using the harmonic mean:

$$C_h = \left[\frac{1}{H_0} \int_0^{H_0} \frac{dz}{C(z)} \right]^{-1}. \tag{4.6}$$

This will shift the range profile by a constant value since range is linear with sound speed. As a result, errors in C_h will cause uncertainty in the vertical displacement measurement. In the RR1605 cruise, we may consider the RMS of sound speed derived from XBT profiles (Figure 4.10) as an upper bound of the sound speed error for the duration of the cruise. Unsurprisingly, we observe the largest variance in sound speed in the region of the thermocline between 100 m and 300 m depth, due to the propagation of density waves. However, the regions shallower and deeper are far better constrained.

We estimate the variation in C_h for the duration of the cruise by computing the harmonic mean of the RMS profile. However, since the actual water depth is

approximately 3000 m instead of the 800 m shown in Figure 4.10, we must make an assumption about the sound speed variation at depth. In this case, we assume the sound velocity conforms to models of mean annual sound velocity described by Levitus [1982] and Dushaw et al. [1993]. Thus, we expect the RMS variation observed beneath the thermocline to hold constant throughout the rest of the profile. Since the region of high RMS due the thermocline is a small portion of the water column, the harmonic mean of the RMS profile is close to 0.4 m/s, being governed primarily by the stable, deep waters. If we multiply this value by the approximate two-way travel time of sound through the water column, 4 seconds, we arrive at an estimate of 1.6 m as the maximum RMS uncertainty in the vertical displacement measurements made during this cruise.

4.5 Discussion & Conclusions

We demonstrate displacement measurements between repeated sidescan sonar tracks collected above the Ayu Trough during the RR1605 cruise with RMS uncertainties of 0.25-0.67 m across track and 0.37-0.75 m in vertical derived from closure tests. This is sufficient to measure the displacement due to large earthquakes with $M_\omega > 8.0$. The uncertainty of these measurements has little correlation with across-track separation, demonstrating that we have successfully rotated the reference and repeat tracks into a consistent reference frame of range and azimuth. There is a weak dependence on the ship speed for speeds $<$8 knots, reflecting denser sampling on the seafloor in the azimuth direction.

For this study we employed a simple processing strategy that fits a Gaussian peak to the correlation coefficient using a least-squares inversion. This method produces fit uncertainties on the order of 0.5 m, but the closure of Track 1 displacements imply an uncertainty closer to 0.65 m. Previous studies of digital image correlation methods

have argued that more robust measurements may be obtained using a spline-fitting or Newton-Rhapson algorithm [Pan et al. 2009]. In addition, our correlation algorithm implicitly assumes that the seafloor is moving as a block unit the size of ensonified area on either the port or starboard of the vessel. Thus, localized deformation occurring in small subsections of the swath may cause the algorithm to arrive at a false solution.

We measured displacements with magnitudes of up to 2 m over a 40 hour time scale during which we expect no seafloor deformation. Thus, these measurements are probably a reflection of uncertainties introduced due to contributions from the ship navigation and sound speed profile. The contribution due to ship navigation is discussed in detail in Chapter 5 [DeSanto, Chadwell, and Sandwell 2018], and contributes 6 cm of uncertainty to the across-track measurements and 14 cm to the vertical measurements. The uncertainty contribution from the sound speed profile may be broken into three components: the contribution to the vertical uncertainty resulting from deviations of the average sound speed, the contribution to the across-track uncertainty from deviations in the surface sound speed, and horizontal variations in sound speed not measured by the XBT. Surprisingly, variation in the thermocline seems to have a limited effect on the average sound speed due to being restrained to a limited section of the water column. However, even with the current accuracy of the sound velocity in more stable portions of the water column, we still estimate a 1.6 m upper bound of uncertainty in the vertical component. This estimate depends on the two-way travel time of sound at nadir and may increase or decrease with depth accordingly. This estimate is derived from XBT measurements made in the upper water column; for deeper sound speeds we rely on the levitus model [Levitus 1982; Dushaw et al. 1993]. However, we are confident this is a reasonable assumption since we expect the sound speed to be more stable beneath the thermocline.

Variation in the surface sound speed is used to derive an estimate of across-track

uncertainty of 0.3 m. This estimate depends on the topographic relief across the swath and will be minimized as the bathymetry approaches the flat seafloor assumption. However, it also is specific to the region in which the RR1605 survey was conducted. Since the Ayu Trough is in an equatorial region, we expect the temperature of the sea surface to be stable as a result of the tropical climate. In regions with a greater seasonal temperature variation, we expect this error to increase accordingly.

We also estimated seafloor displacements between repeated sidescan surveys collected during the SR1704 cruise above the San Diego Trough Fault and *R/V Okeanos Explorer* transits in the central Pacific, but these measurements display greater uncertainties for many reasons. The SR1704 cruise was hindered by a rougher sea state and the loss of a dual-frequency navigation feed partway through the survey, resulting in the loss of early raw data and subsequently much higher navigation uncertainties. Repeat Okeanos Explorer data had very low correlation and thus failed to produce an accurate displacement estimate. This could have been in part to the faster transit speeds decreasing the sounding density, but is likely also the result of the multibeam sonar employed. The *R/V Okeanos Explorer* employs a 30 kHz Kongsberg EM322 rather than a 12 kHz EM122. The higher frequency sonar has a finer resolution but is also limited to shallower ocean depths due to greater attenuation. In deep waters the 30 kHz multibeam can still collect bathymetry data but is limited to a narrower swath, which negatively impacts the ground range resolution of sidescan, which approaches a theoretical singularity at nadir. At present we do not have enough information to discern which of these effects was the dominant source of uncertainty in the 30 kHz data, but we expect this instrument to produce data of sufficient, if not superior, quality at depths shallower than 1500 m.

Acknowledgements

We would like to thank the Scripps Ship Scheduling Office, Shipboard Technical Services, James Holmes, Captain Dave Murline, and the crew of the R/V Roger Revelle, without any of whom the RR1605 cruise would not have been possible. Likewise for Matt Cook, Glenn Sasagawa, and crew of the R/V Sally Ride for making the SR1704 cruise possible. This work was supported by the National Science Foundation, Marine Geology and Geophysics Division, grant 1536386. The RR1605 and SR1704 cruises were supported by the UC Student Ship Funds Program.

Chapter 4, in full, is currently being prepared for publication as DeSanto, J. B., Sandwell, D. T., "Seafloor Geodesy from Repeated Sidescan Sonar Surveys: Optimal Survey and Processing Parameters". The dissertation author was the primary investigator and author of the paper.

References

Atwater, Tanya (1970). "Implications of Plate Tectonics for the Cenozoic Tectonic Evolution of Western North America". In: *GSA Bulletin* 81.12, p. 3513. DOI: 10.1130/0016-7606(1970)81[3513:IOPTFT]2.0.CO;2. eprint: /gsw/content_public/journal/gsabulletin/81/12/10.1130_0016-7606(1970)81[3513_ioptft]2.0.co;2/3/i0016-7606-81-12-3513.pdf. URL: http://dx.doi.org/10.1130/0016-7606(1970)81[3513:IOPTFT]2.0.CO;2.

Bürgmann, Roland and Chadwell, David (2014). "Seafloor Geodesy". In: *Annual Review of Earth and Planetary Sciences* 42.1, pp. 509–534. DOI: 10.1146/annurev-earth-060313-054953.

Caress, David W. and Chayes, Dale N. (2015). *MB-System: Mapping the Seafloor*. DOI: http://www.mbari.org/data/mbsystem, http://www.ldeo.columbia.edu/res/pi/MB-System.

De Moustier, C (Jan. 1988). "State of the Art in Swath Bathymetry Survey Systems". In: *OED (ASME, Ocean Engineering Division)* 13.

Del Grosso, V. A. (1974). “New equation for the speed of sound in natural waters (with comparisons to other equations)”. In: *The Journal of the Acoustical Society of America* 56.4, pp. 1084–1091. DOI: 10.1121/1.1903388.

DeSanto, John B., Chadwell, C. David, and Sandwell, David T. (2018). “Kinematic Post-processing of Ship Navigation Data Using Precise Point Positioning”. In: *journal of Navigation*.

DeSanto, John B., Sandwell, David T., and Chadwell, C. David (2016). “Seafloor geodesy from repeated sidescan sonar surveys”. In: *Journal of Geophysical Research: Solid Earth*. 2016JB013025. ISSN: 2169-9356. DOI: 10.1002/2016JB013025.

Dushaw, Brian D., Worcester, Peter F., Cornuelle, Bruce D., and Howe, Bruce M. (1993). “On equations for the speed of sound in seawater”. In: *The Journal of the Acoustical Society of America* 93.1, pp. 255–275. DOI: 10.1121/1.405660.

Fujiwara, T., Tamaki, K., Fujimoto, H., Ishii, T., Seama, N., Toh, H., Koizumi, K., Igarashi, C., Segawa, J., Kobayashi, K., Kido, M., Seno, T., and Kinoshita, H. (1995). “Morphological Studies of the Ayu Trough, Phillippine Sea - Caroline Plate Boundary”. In: *Geophysical Research Letters* 22, pp. 109–112. DOI: 10.1029/94GL02719.

Fujiwara, T, Kodaira, S, No, T, Kaiho, Y, Takahashi, N, and Kaneda, Y (2011). “The 2011 Tohoku-oki earthquake: displacement reaching the trench axis”. In: *Science* 334, p. 1240.

Fujiwara, Toshiya, Christian, Santos Ferreira, Katharina, Bachmann Anna, Michael, Strasser, Gerold, Wefer, Tianhaozhe, Sun, Toshiya, Kanamatsu, and Shuichi, Kodaira (2017). “Seafloor Displacement After the 2011 Tohoku-oki Earthquake in the Northern Japan Trench Examined by Repeated Bathymetric Surveys”. In: *Geophysical Research Letters* 44.23, pp. 11,833–11,839. DOI: 10.1002/2017GL075839.

Hong, J. K. and Lee, S. M. (2002). “Reflection Seismology in the Southern Ayu Trough, a Slow-spreading Divergent Boundary”. In: *Ocean and Polar Research* 24, pp. 189–196. DOI: 10.4217/OPR.2002.24.3.189.

Levitus, S. (1982). “Climatological Atlas of the World Ocean”. In: *NOAA/ERL GFDL Professional Paper 13, Princeton, N.J., 173 pp. (NTIS PB83-184093)*.

Lindvall, Scott C. and Rockwell, Thomas K. (1995). “Holocene activity of the Rose Canyon fault zone in San Diego, California”. In: *Journal of Geophysical Research: Solid Earth* 100.B12, pp. 24121–24132. DOI: 10.1029/95JB02627. URL: https://agupubs.onlinelibrary.wiley.com/doi/abs/10.1029/95JB02627.

McNeilan, Thomas W., Rockwell, Thomas K., and Resnick, Gregory S. (1996). "Style and rate of Holocene slip, Palos Verdes fault, southern California". In: *Journal of Geophysical Research: Solid Earth* 101.B4, pp. 8317–8334. DOI: 10.1029/95JB02251. URL: https://agupubs.onlinelibrary.wiley.com/doi/abs/10.1029/95JB02251.

Pan, Bing, Qian, Kemao, Xie, Huimin, and Asundi, Anand (2009). "Two-dimensional digital image correlation for in-plane displacement and strain measurement: a review". In: *Measurement Science and Technology* 20.6, p. 062001. URL: http://stacks.iop.org/0957-0233/20/i=6/a=062001.

Platt, John P. and Becker, Thorsten W. (2010). "Where is the real transform boundary in California?" In: *Geochemistry, Geophysics, Geosystems* 11.6. DOI: 10.1029/2010GC003060. URL: https://agupubs.onlinelibrary.wiley.com/doi/abs/10.1029/2010GC003060.

Ryan, H. F., Conrad, J. E., Paull, C. K., and McGann, M. (2012). "Slip Rate on the San Diego Trough Fault Zone, Inner California Borderland, and the 1986 Oceanside Earthquake Swarm RevisitedSlip Rate on the SDTFZ, Inner California Borderland, and the 1986 Oceanside Earthquake Swarm Revisited". In: *Bulletin of the Seismological Society of America* 102.6, p. 2300. DOI: 10.1785/0120110317. eprint: /gsw/content_public/journal/bssa/102/6/10.1785_0120110317/3/2300.pdf. URL: http://dx.doi.org/10.1785/0120110317.

Weissel, Jeffrey K. and Anderson, Roger N. (1978). "Is there a Caroline Plate?" In: *Earth and Planetary Science Letters* 41, pp. 143–158. DOI: 10.1016/0012-821X(78)90004-3.

Chapter 5

Kinematic Post-processing of Ship Navigation Data Using Precise Point Positioning

5.1 Introduction

Measuring small absolute displacements of the seafloor ($<$10 m) in the deep ocean is challenging since doing so requires a combination of acoustic measurements with measurements of a moving platform [Bürgmann and Chadwell 2014]. Advancements have allowed seafloor geodetic surveys to be performed with increasing frequency in recent years [Tadokoro et al. 2012; Yokota et al. 2015; Yokota et al. 2016; Yasuda et al. 2017]. However, geodetic methods such as GPS-Acoustic [Spiess et al. 1998; Fujita et al. 2006] rely on positioning points on the seafloor relative to a research platform and thus could be limited by the quality of GPS navigation used to constrain the platform location.

Most seafloor geodetic studies obtain a real-time kinematic solution of shipboard GPS stations, utilizing land stations as reference. However, in remote regions this may

not be feasible or require creative workarounds, such as the temporary deployment of land stations [Gagnon, Chadwell, and Norabuena 2005]. An alternative is to post-process navigation collected at sea using precise point positioning (PPP). PPP relies on clock and orbit solutions obtained from pre-existing networks to individually process remote stations [Zumberge et al. 1997]. Since PPP does not require proximity to a land reference station to obtain a solution, it is well suited to marine surveys that may be hundreds of kilometers offshore.

Shipboard campaign GPS have been repeatedly shown to have vertical accuracy sufficient to distinguish changes in position from atmospheric signals due to precipitable water vapor, either after processing with respect to nearby land stations [Chadwell and Bock 2001; Kealy, Foster, and Businger 2012] or PPP [Rocken et al. 2005]. These studies show RMS errors on order 10 cm in the vertical GPS component. Likewise, Foster [2014] estimated a horizontal precision of shipboard GPS on order 7 cm derived from baseline measurements between GPS stations. Most recently, Watanabe et al. [2017] estimated horizontal PPP errors to be on the order of 2 cm at sea.

However, these studies do not consider GPS data collected by the standard dual-frequency GPS systems deployed on University-National Oceanographic Laboratory System (UNOLS) vessels. Multiple UNOLS vessels such as the R/V Roger Revelle and the R/V Sally Ride now employ a Kongsberg Seapath330+ for dual frequency ship navigation. These data should yield ship locations of comparable quality to campaign GPS stations.

The focus of this study was to evaluate the absolute accuracy that a ship can be positioned in a remote ocean location using a standard dual-frequency receiver and standard PPP processing. In doing so, we estimated the uncertainties introduced by a number of noise sources, including difficulties in locking onto low elevation satellites due to the roll and pitch of the vessel, and multi-path reflections from large surfaces

on the ship. We also verified any dependence on processing strategy or software. This was accomplished by using three PPP software packages to evaluate GPS data from two experiments: a known fixed position to establish a baseline accuracy of the PPP softwares and a remote moving platform to explore the uncertainties introduced by the noise sources previously declared. The PPP software packages are the Kalman Filter solver in PANDA [Shi et al. 2008] processed using the methodology described by Geng et al. [Geng et al. 2013], GIPSY-OASIS [Zumberge et al. 1997; Bertiger et al. 2010], and the Canadian Spatial Reference System (Natural Resources Canada [2016]).

5.2 Aleutian Island Station AB21

The first experiment was designed to evaluate the absolute accuracy of the three PPP software packages using continuously recorded GPS data from a fixed remote island location. The station we chose was station AB21 on the Aleutian Islands. This station is appropriate to compare to ship navigation because it is not used to generate International GNSS Service (IGS) clocks and orbits, is in a very remote location 1675 km from the nearest IGS network station, has a long (>10 years) time series of daily solutions, and periods of high-rate data collection at a 1 second interval that is comparable to the data collected by ship navigation. We processed data collected from 16 June 2014 to 18 June 2014, a subsection of the most recent month during which high-rate data was collected at this station and during a period in which there were no significant earthquakes or aftershocks in the region. The position accuracies during this time derived from the Scripps Orbit and Permanent Array Center (SOPAC) are 0.3 cm in the horizontal components and 0.8 cm in the vertical component.

We generate kinematic PPP solutions for land station AB21 high-rate data using the PANDA, GIPSY, and CSRS software. Solution accuracy is judged against the SOPAC

daily solution (Figure 5.1, Table 5.1). We find the three kinematic solutions agree with the SOPAC daily solution with 2σ standard deviations of 1.1-1.3 cm in the East and North components and 2.3-3.5 cm in the vertical component.

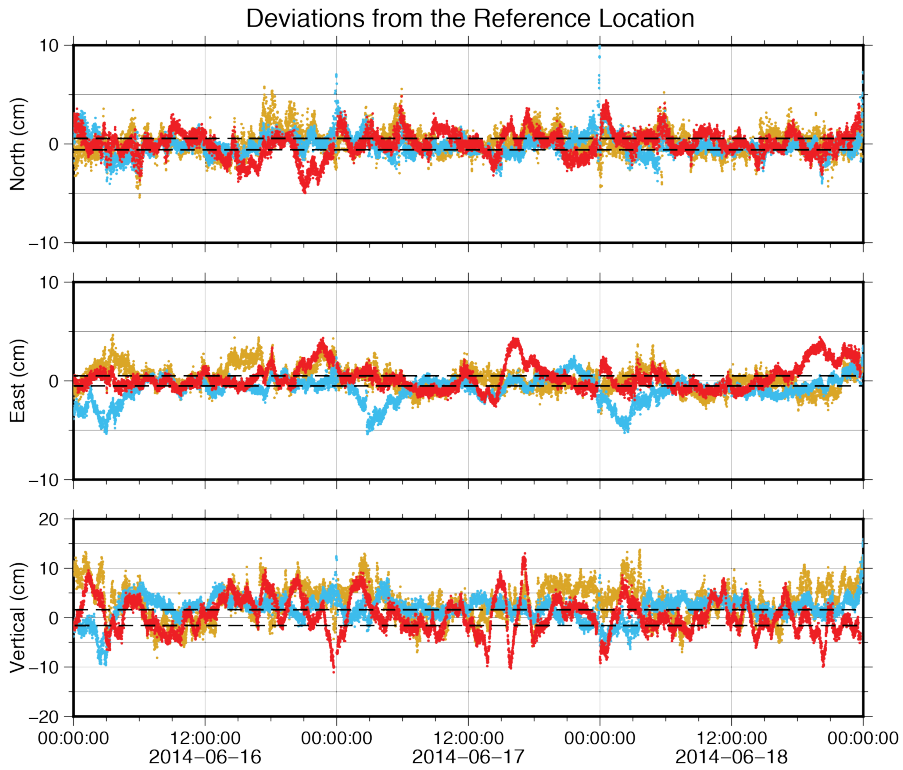

Figure 5.1: **Kinematic solutions for station AB21, plotted as differences relative to the SOPAC daily solution. Red time series is the PANDA solution, blue time series is the CSRS solution, gold time series is the GIPSY solution. Dashed lines show 2σ uncertainties for the SOPAC daily solution.**

5.3 RR1605 Station Analysis

We assessed the accuracy of PPP positions at sea using data collected on board the R/V Roger Revelle during the RR1605 cruise in May, 2016. The cruise objective was to determine how accurately a patch of seafloor could be positioned using repeated sonar data [DeSanto, Sandwell, and Chadwell 2016], and contains multiple repeated tracks

Table 5.1: **Locations of station AB21 obtained by averaging kinematic time series. SOPAC daily solution is the reference point.** 2σ **standard deviations are reported as errors.**

Software	North (cm)	East (cm)	Vertical (cm)
CSRS	-0.1 ± 1.1	-0.8 ± 1.3	1.9 ± 2.3
PANDA	0.4 ± 1.3	0.3 ± 1.3	0.4 ± 3.5
GIPSY	0.2 ± 1.2	0.2 ± 1.2	3.2 ± 3.5

arranged in a 12 nautical mile by 12 nautical mile cross pattern. The survey area was a patch of seafloor above the Ayu Trough approximately 330 km southwest of the island nation of Palau, 870 km East of the Philippines, and 550 km north of Papua New Guinea (Figure 5.2). We chose this region because the Ayu Trough is a very slow spreading center between the Caroline Sea Plate and the Philippine Plate, convenient for the sidescan calibration survey described in Chapter 4. Current estimates of the half-spreading rate along the Ayu Trough are 3.5-9.1 mm/yr [Fujiwara et al. 1995; Hong and Lee 2002]. Our analysis will primarily focus on the entire 40 hour survey, but individual tracks are straight segments ranging in duration from 1-2 hours. Thus, we shall also explore the expected navigation accuracy on the shorter time scale of a single track.

GPS data were collected at 2 stations during this cruise: the Seapath330+ navigation system employed on the vessel (henceforth referred to as station RRNV) and a campaign-style Trimble NetR9 receiver (henceforth referred to as station RR01). The antenna for these stations were both installed in elevated positions on board the vessel; ship navigation RRNV was (and remains) located on the aft mast and campaign GPS RR01 was installed on the deck above the bridge. We process data collected from 13 May 2016 to 15 May 2016 using the PANDA, CSRS, and GIPSY software as before. The closest IGS stations were in Manila, Philippines at a distance of 1700 km from the survey area and Guam at a distance of 1600 km, so a real-time kinematic solution and differential GPS solutions are unavailable; we must make inferences by comparing the

kinematic PPP solutions obtained from different software.

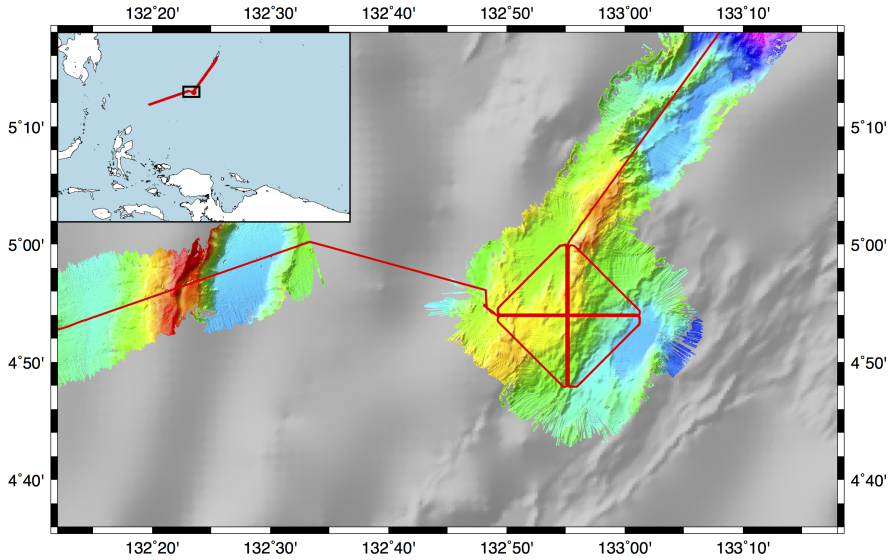

Figure 5.2: **Map of the RR1605 cruise. Track lines denoted in red and collected bathymetry denoted by colored relief. Greyscale bathymetry taken from the SRTM15 model derived from satellite altimetry [Smith and Sandwell 1997]. Inset diagram shows regional context of the cruise.**

The first comparison we considered was of the RRNV solutions shown in Figure 5.3, taking the GIPSY-OASIS solution as a baseline (reported uncertainties have been divided by a factor of $\sqrt{2}$ to account for the difference). The kinematic solutions agreed with 2σ standard deviations of 2.4-2.8 cm in the North component, 5.7-5.9 cm in the East component and 11.4-12.4 cm in the vertical component (Table 5.2). Assuming that the inherent uncertainties of the PPP solutions are the values inferred from the land station AB21 case in Table 5.1, the marine GPS solutions introduced 2.0-2.6 cm of noise in the North component, 5.6-5.8 cm of noise in the East component, and 11-11.9 cm of noise in the vertical component compared to the land station. This likely resulted from inherent differences between terrestrial and marine environments. The constant swell of the ocean meant that satellites near the horizon continually swayed in and out of visibility. Consequently, quality control of the raw data confirmed an increase of ionospheric slips particularly when satellites came into view.

We also inferred the uncertainty in the GPS time series for time scales on the order of a single ship track. Each straight survey required 1-2 hours depending on ship speed. Upon inspection of Figure 5.3, we confirmed that despite being more precise over these shorter time scales, the mean difference between PPP solutions varied within the standard deviations reported for the whole survey in Table 5.2. During the shorter time interval, the GPS satellites completed only a fraction of their orbit, which may explain these systematic deviations from the long-term mean.

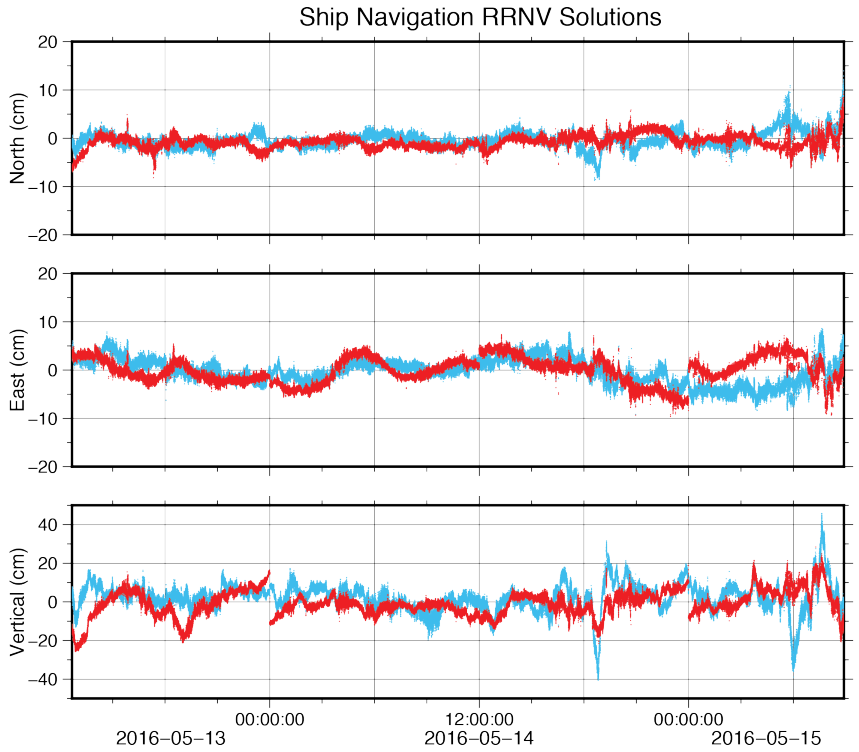

Figure 5.3: **RRNV solutions, taking the GIPSY-OASIS solution as a reference. Red is the PANDA solution. Blue is the CSRS solution.**

The comparison between kinematic solutions for station RR01 (Figure 5.4, Table 5.2) was significantly worse. The GIPSY-OASIS and PANDA solutions for the campaign GPS agreed with uncertainties at least twice as large as the ship navigation case, implying an additional source of noise adding 4.4 cm to the North component, 7.3 cm to the East component, and 5.0 cm to the vertical component of the previous estimates. The CSRS

Table 5.2: **Differences between solutions generated by reported software for stations RRNV and RR01.** 2σ **standard deviations are reported as errors.**

Station	Software	North (cm)	East (cm)	Vertical (cm)
RRNV	PANDA-GIPSY	-0.7 ± 2.4	0.1 ± 5.9	-1.1 ± 12.4
RRNV	CSRS-GIPSY	-0.6 ± 2.8	-0.1 ± 5.7	2.5 ± 11.4
RR01	PANDA-GIPSY	-0.1 ± 5.4	-0.9 ± 11.0	-1.2 ± 17.9
RR01	CSRS-GIPSY	1.0 ± 10.2	3.5 ± 28.3	21.3 ± 39.4

solution was an even greater outlier. This lack of repeatability implies a shortcoming of the station since the ship navigation solutions obtained were more stable despite being collected on the same moving platform at the same time and processed with the same software. A probable cause for the poorer accuracy of campaign GPS RR01 solutions was the location of the antenna. Although situated at a higher elevation, the campaign GPS was also directly in the shadow of the ship's radar equipment and therefore susceptible to lesser sky visibility and greater multipath effects. Quality control of the raw data verified the campaign GPS had many more multipath slips than the ship navigation. The multipath RMS values varied from 1.06-2.05 m for the campaign GPS as opposed to 0.27-0.43 m for the ship navigation. These campaign GPS solutions thus provide a clear example of the variance that may be introduced as a result of antenna placement on the vessel.

5.4 Comparison to Real-time Ship Navigation

We evaluated the utility of the standard scientific instrumentation deployed on UNOLS vessels by comparing post-processed PPP and real-time ship navigation solutions. Since both the PPP and real-time solutions were derived from the Seapath330+ instrument, significant deviations from a common solution result from error of the real-time solution, assuming the accuracy of RRNV solutions were the same as for the land station AB21

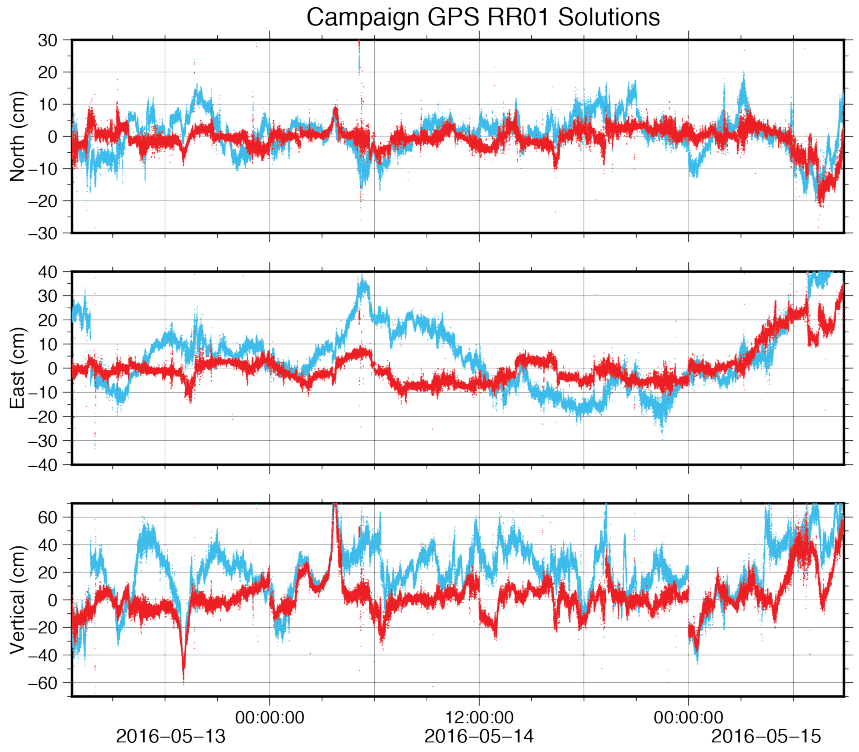

Figure 5.4: **RR01 solutions, taking the GIPSY-OASIS solution as a reference. Red is the PANDA solution. Blue is the CSRS solution.**

solutions.

Although conceptually simple, there are two complications introduced by this calculation. The first complication is that an offset was introduced to the real-time solution during the processing step so that it tracks the motion reference unit of the vessel rather than the antenna. This offset is known from independent surveys of the instrumentation on board the Roger Revelle, and reported as "Truth" in Table 5.3. The second complication is that the horizontal components of the difference between post-processed and real-time solutions were not independent due to the continuously changing heading of the vessel during the survey. We avoided this issue by considering the magnitude of horizontal displacement between solutions rather than individual components. The vertical component was considered separately because it is independent of heading and (as previously demonstrated) has worse accuracy compared to the horizontal components.

Figure 5.5 and Table 5.3 show histograms of the distances between the PANDA and real-time solutions of the ship navigation, corresponding to the vertical and horizontal components. Accounting for the width of the histograms, the solutions were 20.296 ± 1.423 m apart in the horizontal components and 11.061 ± 3.630 m apart in the vertical component. Comparing this measurement to the expected distances, we found the horizontal and vertical distances to be within error. Assuming RRNV solutions with accuracy comparable to the AB21 solutions and pitch and roll errors on the order of 60 cm (obtained for the known instrument geometry by estimating variations of $\pm 3°$), this implies the horizontal ship navigation components may be accurate to 0.8 m and the vertical component may be accurate to 2.8 m. This analysis was repeated using other PPP solutions for ship navigation RRNV, yielding similar results for the other processing techniques. In light of our expected noise levels for the PPP solutions, nearly all of this uncertainty must be indicative of the noise level in the real-time ship navigation solution. It is important to note that the real-time solution is not a Real Time Kinematic (RTK) solution because these data were collected too far from a stable land station. We expect the real-time ship navigation solution to be more accurate closer to shore when an RTK solution is available.

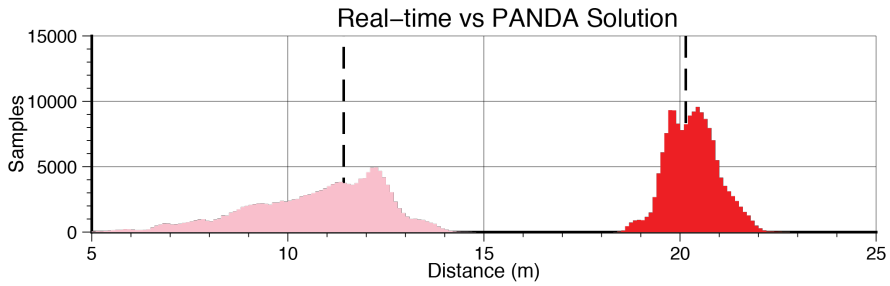

Figure 5.5: **Histograms of the horizontal (red) and vertical (pink) components of distance between the PPP solution (computed using PANDA) and real-time ship navigation solutions. Bold dashed lines indicate the true distances between the Seapath 330+ antenna and the motion reference unit.**

Table 5.3: **Horizontal and vertical components of distance between RRNV real-time and PPP solutions. The known value between the antenna and motion reference unit is reported as Truth. 2σ standard deviations are reported as errors.**

RRNV Solution	Horizontal Distance (m)	Vertical Distance (m)
Truth	20.141	11.427
PANDA	20.296 ± 1.423	11.061 ± 3.630
CSRS	20.286 ± 1.397	11.107 ± 3.603
GIPSY	20.288 ± 1.405	11.076 ± 3.598

5.5 Conclusions

We have performed PPP post-processing on the following 3 stations: continuous land-based station AB21, ship navigation RRNV, and campaign GPS station RR01 deployed on a research vessel at sea. We generated solutions using CSRS, PANDA, and GIPSY-OASIS software, all of which agreed with the SOPAC daily solution for station AB21 with uncertainties of 1.1-1.3 cm in the horizontal components and 2.3-3.5 cm in the vertical component, verifying that PPP is an accurate method for land-based stations even in remote areas far from the network used to determine clocks and orbits.

The PPP solutions also agreed for ship navigation RRNV, although frequent ionospheric slips of low elevation satellites due to the rocking of the research vessel with the ocean swell introduced 2.0-5.8 cm of horizontal uncertainty and 11.0-11.9 cm of vertical uncertainty to the solutions. The solutions were somewhat larger over the shorter time increments that will be used for the repeated sonar surveys. We may not draw a quantitative conclusion about the absolute accuracy of these solutions since we do not have the equivalent of a SOPAC daily solution at sea for a moving platform, but the high degree of repeatability demonstrated implies that PPP-processed ship navigation may be accurate enough for GPS-Acoustic surveys as long as enough data is collected to cover multiple orbital cycles of the constellation. Shorter collection periods yielded less stable results, but the sub-meter accuracies obtained are still sufficient for repeated sidescan

sonar surveys.

The solutions were poorer for station RR01, which had at least an additional 4.4 cm of uncertainty in the North component, 7.3 cm of uncertainty in the East component, and 5.0 cm of uncertainty in the vertical component. The CSRS solution was particularly unstable for this station, having additional uncertainties at least twice as large. We attribute this apparent degradation in quality compared to the ship navigation RRNV solutions to differences in receiver location. The campaign GPS being installed above the bridge (and subsequently below the ship's radar equipment) likely led to it having poorer sky visibility and greater multipath susceptibility compared to the ship navigation, which is installed on the aft mast.

We used the RRNV solutions to evaluate the accuracy of the real-time ship navigation feed by comparing the measured distance between the PPP and real-time solutions to the known distance between the ship antenna and the motion reference unit. We found the horizontal component to be accurate to within 1.4 m and the vertical component to within 3.6 m of known values. Factoring the expected noise introduced by the roll and pitch of the vessel, we expect the uncertainties of the real-time ship navigation solution to be 0.8 m in the horizontal components and 2.8 m in the vertical component. These estimates may overestimate the measurement error given our lax treatment of ship orientation. Nevertheless, the difference between standard and post-processed ship navigation still implies an improvement of many decimeters in the horizontal components and a few meters in the vertical component in computing the platform location.

PPP is a viable method for calculating ship position that may be used to provide kinematic solutions repeatable on scales of a few centimeters, even in very remote locations where differential GPS may not be feasible. Despite being a post-processing technique, it may be used to obtain near real-time solutions with a delay of a few hours using the IGS "ultra" solutions for satellite clocks and orbits. The station geometry is

critical for this method, which requires good visibility and little multipath. An additional point of interest is that these results may not be fully indicative of the accuracy obtainable by the ship navigation. The ship navigation logged data from Galileo and Beidou satellites throughout the survey that were not utilized during this study because these networks have not yet been integrated into the PPP software considered. Thus, we expect these results to improve in the future as PPP solutions using these satellites become more common.

Acknowledgements

We would like to acknowledge Peng Fang and Yehuda Bock for their assistance in setting up the PANDA software, as well as three anonymous reviewers for their feedback on the initial manuscript. We would also like to thank the Scripps Ship Scheduling Office, Shipboard Technical Services, James Holmes, Captain Dave Murline, and the crew of the R/V Roger Revelle. This work was supported by the National Science Foundation, Marine Geology and Geophysics Division, grant 1536386. The RR1605 cruise was supported by the UC Student Ship Funds Program.

Chapter 5, in full, is a reprint of the material as it will appear in the Journal of Navigation: DeSanto, J. B., C. D. Chadwell, D. T. Sandwell, "Kinematic Post-processing of Ship Navigation Data Using Precise Point Positioning", *Journal of Navigation*, accepted. The dissertation author was the primary investigator and author of the paper.

References

Bertiger, Willy, Desai, Shailen D., Haines, Bruce, Harvey, Nate, Moore, Angelyn W., Owen, Susan, and Weiss, Jan P. (2010). "Single receiver phase ambiguity resolu-

tion with GPS data". In: *Journal of Geodesy* 84.5, pp. 327–337. ISSN: 1432-1394. DOI: 10.1007/s00190-010-0371-9.

Bürgmann, Roland and Chadwell, David (2014). "Seafloor Geodesy". In: *Annual Review of Earth and Planetary Sciences* 42.1, pp. 509–534. DOI: 10.1146/annurev-earth-060313-054953.

Canada, Natural Resources (2016). *Canadian Spatial Reference System (CSRS) Precise Point Positioning (PPP) tool*. https://webapp.geod.nrcan.gc.ca/geod/tools-outils/ppp.php?locale=en.

Chadwell, C. David and Bock, Yehuda (2001). "Direct estimation of absolute precipitable water in oceanic regions by GPS tracking of a coastal buoy". In: *Geophysical Research Letters* 28.19, pp. 3701–3704. DOI: 10.1029/2001GL013280.

DeSanto, John B., Sandwell, David T., and Chadwell, C. David (2016). "Seafloor geodesy from repeated sidescan sonar surveys". In: *Journal of Geophysical Research: Solid Earth*. 2016JB013025. ISSN: 2169-9356. DOI: 10.1002/2016JB013025.

Foster, James, Li, Ning, and Cheung, Kwok Fai (2014). "Sea State Determination from Ship-Based Geodetic GPS". In: *Journal of Atmospheric and Oceanic Technology* 31.11, pp. 2556–2564. DOI: 10.1175/JTECH-D-13-00211.1.

Fujita, Masayuki, Ishikawa, Tadashi, Mochizuki, Masashi, Sato, Mariko, Toyama, Shinichi, Katayama, Masato, Kawai, Koji, Matsumoto, Yoshihiro, Yabuki, Tetsuichiro, Asada, Akira, and Colombo, Oscar L. (2006). "GPS/Acoustic seafloor geodetic observation: method of data analysis and its application". In: *Earth, Planets and Space* 58.3, pp. 265–275. ISSN: 1880-5981. DOI: 10.1186/BF03351923. URL: https://doi.org/10.1186/BF03351923.

Fujiwara, T., Tamaki, K., Fujimoto, H., Ishii, T., Seama, N., Toh, H., Koizumi, K., Igarashi, C., Segawa, J., Kobayashi, K., Kido, M., Seno, T., and Kinoshita, H. (1995). "Morphological Studies of the Ayu Trough, Phillippine Sea - Caroline Plate Boundary". In: *Geophysical Research Letters* 22, pp. 109–112. DOI: 10.1029/94GL02719.

Gagnon, Katie, Chadwell, C. David, and Norabuena, Edmundo (Mar. 2005). "Measuring the onset of locking in the Peru-Chile trench with GPS and acoustic measurements". In: *Nature* 434.7030, pp. 205–208. URL: http://dx.doi.org/10.1038/nature03412.

Geng, Jianghui, Bock, Yehuda, Melgar, Diego, Crowell, Brendan W., and Haase, Jennifer S. (2013). "A new seismogeodetic approach applied to GPS and accelerometer observations of the 2012 Brawley seismic swarm: Implications for earthquake early warning". In: *Geochemistry, Geophysics, Geosystems* 14.7, pp. 2124–2142. DOI: 10.1002/ggge.20144.

Hong, J. K. and Lee, S. M. (2002). "Reflection Seismology in the Southern Ayu Trough, a Slow-spreading Divergent Boundary". In: *Ocean and Polar Research* 24, pp. 189–196. DOI: 10.4217/OPR.2002.24.3.189.

Kealy, John, Foster, James, and Businger, Steven (2012). "GPS meteorology: An investigation of ocean-based precipitable water estimates". In: *Journal of Geophysical Research: Atmospheres* 117.D17. DOI: 10.1029/2011JD017422.

Rocken, Christian, Johnson, James, Van Hove, Teresa, and Iwabuchi, Tetsuya (2005). "Atmospheric water vapor and geoid measurements in the open ocean with GPS". In: *Geophysical Research Letters* 32.12. DOI: 10.1029/2005GL022573.

Shi, Chuang, Zhao, Qile, Geng, Jianghui, Lou, Yidong, Ge, Maorong, and Liu, Jingnan (2008). "Recent development of PANDA software in GNSS data processing". In: *Proc.SPIE* 7285, pp. 7285 –7285 –9. DOI: 10.1117/12.816261.

Smith, Walter H. F. and Sandwell, David T. (1997). "Global Sea Floor Topography from Satellite Altimetry and Ship Depth Soundings". In: *Science* 277.5334, pp. 1956–1962. DOI: 10.1126/science.277.5334.1956.

Spiess, F. N., Chadwell, C. D., Hildebrand, J. A., Young, L. E., G. H. Purcell, Jr., and Dragert, H. (1998). "Precise GPS/Acoustic positioning of seafloor reference points for tectonic studies". In: *Phys. of the Earth and Plan. Int.* 108, pp. 101–112.

Tadokoro, Keiichi, Ikuta, Ryoya, Watanabe, Tsuyoshi, Ando, Masataka, Okuda, Takashi, Nagai, Satoru, Yasuda, Kenji, and Sakata, Tsuyoshi (2012). "Interseismic seafloor crustal deformation immediately above the source region of anticipated megathrust earthquake along the Nankai Trough, Japan". In: *Geophysical Research Letters* 39.10. DOI: 10.1029/2012GL051696.

Watanabe, Shunichi, Bock, Yehuda, David Chadwell, C, Fang, Peng, and Geng, J (Mar. 2017). "Long-term stability of the kinematic Precise Point Positioning for the sea surface observation unit compared with the baseline analysis". In: *Report of Hydrographic and Oceanographic Researches* 54.

Yasuda, Kenji, Tadokoro, Keiichi, Taniguchi, Sota, Kimura, Hiroshi, and Matsuhiro, Kenjiro (2017). "Interplate locking condition derived from seafloor geodetic observation in the shallowest subduction segment at the Central Nankai Trough, Japan". In: *Geophysical Research Letters* 44.8, pp. 3572–3579. DOI: 10.1002/2017GL072918.

Yokota, Yusuke, Ishikawa, Tadashi, Sato, Mariko, Watanabe, Shun-ichi, Saito, Hiroaki, Ujihara, Naoto, Matsumoto, Yoshihiro, Toyama, Shin-ichi, Fujita, Masayuki, Yabuki, Tetsuichiro, Mochizuki, Masashi, and Asada, Akira (2015). "Heterogeneous interplate coupling along the Nankai Trough, Japan, detected by GPS-

acoustic seafloor geodetic observation". In: *Progress in Earth and Planetary Science* 2.1, p. 10. ISSN: 2197-4284. DOI: 10.1186/s40645-015-0040-y. URL: https://doi.org/10.1186/s40645-015-0040-y.

Yokota, Yusuke, Ishikawa, Tadashi, Watanabe, Shun-ichi, Tashiro, Toshiharu, and Asada, Akira (June 2016). "Seafloor geodetic constraints on interplate coupling of the Nankai Trough megathrust zone". In: *Nature* 534.7607, pp. 374–377. URL: http://dx.doi.org/10.1038/nature17632.

Zumberge, J. F., Heflin, M. B., Jefferson, D. C., Watkins, M. M., and Webb, F. H. (1997). "Precise point positioning for the efficient and robust analysis of GPS data from large networks". In: *Journal of Geophysical Research: Solid Earth* 102.B3, pp. 5005–5017. DOI: 10.1029/96JB03860.

Chapter 6

Conclusions & Future Work

6.1 Chapter Summaries

The goal of this thesis was to describe and test an improved method for measuring seafloor displacements with multibeam sonar, utilizing the sidescan backscatter amplitude data collected simultaneously with multibeam bathymetry rather than the bathymetry itself. The specific conclusions of each chapter are presented as follows:

Chapter 2 was a brief overview of the multibeam sonar that discussed the design of the instrument as well as the physics that govern the resolution of bathymetry and sidescan. I presented the derivations of bathymetry and sidescan resolution, demonstrating that sidescan has superior range resolution compared with the across-track bathymetry resolution. I also discussed important concepts such as beam steering, which inform the types of data processing that must be performed in order to rotate data from separate cruises into a consistent reference frame. This chapter also included a brief discussion of how uncertainties in the sound velocity profile of the ocean affect the multibeam and sidescan measurements. The two sources of sound velocity error are errors in the surface sound velocity and along the acoustic ray path. Quantifying these errors requires

independent measurements of the sound velocity profile such as from an XBT. This also neglects other potential sound speed errors such as horizontal variations in the upper water column.

Chapter 3 presented the data processing method employed to measure displacement using repeated sidescan sonar surveys. The method entails performing digital image correlation on repeated sidescan sonar surveys and solving for the track displacement that yields the maximum correlation. This processing was tested using legacy data available from previous cruises conducted offshore Cascadia and offshore Southern California. These surveys were suitable for calibrating the data processing because they should realistically have had no measurable displacement as a result of being collected over a time span of a few days. Because these surveys only had single pairs of repeat tracks, I probed the precision of the measurements by introducing a synthetic displacement into one of the repeat tracks but not the other; we verified the efficacy of our technique by measuring this synthetic displacement. I demonstrated that meter-level precision is obtainable in the range dimension but not the along-track dimension.

Chapter 4 was a presentation of data collected during the 2016 RR1605 research cruise, specifically designed as a calibration survey for assessing the displacement accuracy obtainable using the method proposed in Chapter 3. This was done by measuring the displacement between four sets of five repeating sidescan sonar surveys collected within a 40-hour period. These repeated surveys were collected with varying ship speed and track separation, allowing me to infer the optimal survey design for collecting sidescan sonar data for geodetic application. I measured displacements with magnitudes of up to 2 m over a 40 hour time scale during which we expect no seafloor deformation. Thus, these measurements are probably a reflection of uncertainties introduced due to contributions from the ship navigation and sound speed profile. I estimated the sound speed errors to have an across-track RMS uncertainty of 0.3 m and a 1.6 m upper

bound of RMS uncertainty in the vertical component. I observed a weak dependence of displacement uncertainty on ship speed, with optimal results collected at speeds of 4-6 knots, and no dependence on track separation. I also estimated seafloor displacements between repeated sidescan surveys collected during the SR1704 cruise above the San Diego Trough Fault and *R/V Okeanos Explorer* transits in the central Pacific, but these measurements displayed greater uncertainties.

Chapter 5 analyzed the ship navigation data collected during the RR1605 cruise, which are critical to properly locating points on the seafloor. I employed Precise Point Positioning (PPP) to obtain a post-processed kinematic GPS solution of the ship navigation since seafloor geodetic surveys are not always close enough to a land GPS station to obtain a differential GPS solution. I assessed the accuracy of the PPP method by calculating the location of a continuous land station (AB21) on the Aleutian islands using three independent processing methods: GIPSY-OASIS, PANDA, and CSRS. We then compared the PPP solutions of the RR1605 cruise to assess the noise added by the moving platform. This was done for both the ship navigation and a campaign-style GPS receiver deployed on the deck during the cruise. I compared these solutions to the real-time ship navigation solution to quantify the improvement in location accuracy obtained by the kinematic post-processing. Overall, the kinematic post-processing improved the ship navigation uncertainty from 0.8 m in the horizontal components and 2.8 m in the vertical component to 7 cm in the horizontal components and 15 cm in the vertical components.

6.2 Future Work

We have demonstrated that repeated sidescan sonar surveys may be used to measure seafloor displacement with uncertainties on the scale of a few meters, which is sufficient to measure displacement due to offshore earthquakes of $M_\omega > 8.0$. Sufficient

data may be collected by surveying a region of interest with a straight track line of 2-3 hours of duration, assuming a ship speed of 4-6 knots. The ideal cruise design would probably be to collect sidescan data alongside a seismic survey, as seismic surveys also require straight tracks collected at a slow speed. However, these types of sidescan surveys may be reasonably integrated into most geophysical cruises; as long as the ship is in an area of interest only a few extra hours during transit are required to create a reference sidescan survey. Regions where these types of reference surveys would be particularly useful are offshore subduction zones including but not limited to the Cascadia, Alaska, Japan, Central and South America, and Hikurangi subduction zones.

Currently, the most critical infrastructure holding back these types of sidescan surveys is the lack of raw ship navigation. To clarify, US research vessels currently only automatically log a real-time solution of the ship navigation insufficient for geodetic purposes. It is possible to access the raw navigation data collected during a cruise as was done during the RR1605 cruise presented in Chapters 4 & 5, but these data are not automatically logged, meaning that most cruises will not have ideal ship navigation data unless the chief scientist specifically asks for it. We have contacted the Ship board Technical Services about setting up a system where raw navigation may be automatically logged in the Rolling Deck to Repository database, which would significantly lower the barrier to performing geodetic studies with legacy multibeam sidescan data.

A difficult issue for seafloor geodesy in general is the treatment of errors in the sound velocity profile. We were able to estimate the error contribution from some sound velocity uncertainties during the RR1605 cruise, but this was due to collecting XBT data at more frequent intervals than is normal for a research cruise. This quantity of sound velocity profiles may not always be available. However, there is a thermosalinograph in the bow thruster that collects a measurement of the sound velocity at the sea surface at 15 second intervals. Currently, these data are only used for diagnostic purposes to

estimate the validity of the current sound velocity used in multibeam data collection, but they could potentially be integrated into a partial sound speed correction for across-track displacement measurements, given the importance of the surface sound speed for estimating the look angle of a ray path.